

Dissertation
submitted to the
Combined Faculty of Natural Sciences and Mathematics
of the Ruperto Carola University Heidelberg, Germany
for the degree of
Doctor of Natural Sciences

presented by

M.Sc. Marvin Albert

born in Heidelberg, Germany

Oral examination: 12.11.2019

**A spatial normalization framework to
quantify signaling receptor activity and
function during embryonic development**

Referees

Prof. Dr. Detlev Arendt

Prof. Dr. Thomas Höfer

Abstract

During the development of an organism, chemokine signaling provides long range guidance for migrating cells and tissues. Using an intricate system of promiscuous receptor-ligand interactions, the embryo coordinates the robust positioning of its future organs in space and time. Cells both sense and actively shape a highly dynamical and diverse signaling environment, thus making it challenging to systematically study cell signaling regulation and function *in vivo*.

To approach this problem, I combined novel methods from the fields of microscopy, cell biology and image analysis. Specifically, this includes multiple-view light sheet microscopy for imaging developmental processes simultaneously at the cell and organism scales and tandem fluorescent lifetime reporters as an emerging tool to visualize signaling receptor turnover *in vivo*. To quantitatively compare three dimensional embryo acquisitions across genetic conditions and multiplex fluorescent readouts, I used nonlinear image registration to perform spatial normalization. Further, the so obtained sample deformation maps were exploited to perform morphometric phenotype analysis. Together, these tools led to the development of a computational analysis framework enabling quantification of chemokine signaling activity and function during embryonic development.

This framework was then applied to search for novel interactions between the chemokine scavenger CXCR7 (or ACKR3) and the signaling receptor CXCR4 in the early zebrafish embryo. In recent years, the competition of these receptors for their shared ligands has been shown to be implicated in several developmental processes

as well as tumor progression. In my analysis, loss of the scavenger was revealed to exert a strong activating effect on CXCR4 expressing tissues across the entire embryo. The remarkable up-regulation of signaling activity in the absence of the scavenger was however found to be aphenotypic in many target tissues. Therefore, I proceeded to investigate at which level the phenotypic impact of this genetic perturbation is compensated for and found receptor desensitization to likely be dispensable in this context.

In conclusion, this work provides an example of how spatial normalization and multiplexing of *in toto* light sheet images can be used to investigate the general logic and functional output of chemokine-scavenger interactions during embryonic development.

Zusammenfassung

Während der Entwicklung eines Organismus dienen Chemokine als weitreichende Signale für die Migration von Zellen und Zellverbänden. Unter Verwendung eines komplexen Systems verworrener Rezeptor-Liganden Interaktionen koordiniert der Embryo die Bildung seiner Organe in Raum und Zeit. Dass Zellen ihre dynamische und vielfältige Signalumgebung nicht nur wahrnehmen sondern gleichzeitig aktiv mitgestalten macht die systematische Untersuchung von Regulation und Funktion interzellulärer Signaltransduktion *in vivo* zu einem schwierigen Unterfangen.

Der in dieser Arbeit verfolgte Ansatz vereint neuartige Methoden der Mikroskopie, Zellbiologie und Bildanalyse um dieses Problem anzugehen. Dies beinhaltet die *in toto* Lichtblattmikroskopie um entwicklungsbiologische Prozesse gleichzeitig auf zellulären und embryonalen Skalen zu untersuchen, sowie den Einsatz von Tandem Fluorescent Lifetime Reporters zur *in vivo* Visualisierung von Signalrezeptordynamik. Um dreidimensionale Embryoaufnahmen quantitativ über verschiedene genetische Hintergründe hinweg zu vergleichen und multiplexen setze ich nichtlineare Bildregistrierung zur räumlichen Normalisierung ein. Die dadurch erhaltenen Verformungsfelder werden zudem zur morphometrischen Phänotypanalyse verwendet. Zusammen führten diese Methoden zur Entwicklung eines computergestützten Verfahrens zur Quantifizierung von Chemokinaktivität und -funktion während der Embryonalentwicklung.

Dieses Verfahren wurde dann für die Suche neuer Interaktionen zwischen dem als Signalsenke fungierenden Chemokinrezeptor CXCR7 (neuerdings ACKR3) und dem

Signalrezeptor CXCR4 im frühen Zebrafischembryo eingesetzt. Zuletzt wurde dem Ringen beider Rezeptoren um gemeinsame Liganden eine wichtige Rolle in diversen entwicklungsbiologischen Prozessen und der Tumorprogression zugeschrieben. In meiner Untersuchung führte das Fehlen der Signalsenke zu einer starken Aktivierung CXCR4 exprimierender Gewebe über den gesamten Embryo hinweg. Diese bemerkenswerte Heraufregulierung der Signalaktivität in Abwesenheit von CXCR7 führte jedoch in den meisten Geweben zu keiner phänotypischen Auswirkung. Daher untersuchte ich auf welcher Ebene der Effekt dieses genetischen Eingriffs kompensiert wird und kam zu dem Schluss, dass Rezeptordesensibilisierung in diesem Zusammenhang wahrscheinlich keine Rolle spielt.

Schlussendlich stellt diese Arbeit ein Beispiel dafür dar, wie die räumliche Normalisierung von *in toto* Lichtblattmikroskopiebildern zur Untersuchung der allgemeinen Logik und Funktionsweise als Signalsenken agierender Chemokinrezeptoren verwendet werden kann.

Contents

Abstract	V
Zusammenfassung	VII
1 Introduction	1
1.1 Tissue migration and chemokine signaling during development	2
1.1.1 Collective cell migration	2
1.1.2 Chemotaxis in response to extracellular gradients	3
1.1.3 Chemokine signaling during development	5
1.1.4 Studying chemokine signaling in the zebrafish embryo	8
1.2 Visualizing cell signaling in vivo	10
1.2.1 Fluorescent readouts of signaling activity	10
1.2.2 Tandem fluorescent protein timers to study receptor dynamics	13
1.2.3 Spatial and temporal multiplexing of fluorescent readouts . . .	17
1.3 In toto multi-view light sheet microscopy	21
1.3.1 Principles of light sheet microscopy	21
1.3.2 Multi-view reconstruction	23
1.4 Aim	27
2 Method development for in toto image quantification	29
2.1 Multi-view image reconstruction	29
2.1.1 Robust content based multi-view image registration	29
2.1.2 Image quality weighted multi-view image reconstruction . . .	34

2.1.3	Evaluation of improved multi-view fusion results	39
2.1.4	A tool for multi-view deconvolution of very large datasets . . .	44
2.2	Atlas framework	49
2.2.1	Spatial normalization of embryo stacks	49
2.2.1.1	Pairwise nonlinear image registration	49
2.2.1.2	Establishing a common reference coordinate system .	55
2.2.2	Definition of tissue patches using segmentation and clustering	60
2.2.3	Experimental setup and statistical analysis	64
2.2.4	Morphometric quantification of tissue phenotypes	65
3	Studying chemokine signaling interactions	71
3.1	In toto measurement of fluorescent lifetime ratios	74
3.2	Cxcr4b receptor signaling dynamics	78
3.2.1	Cxcr4b receptor activity is regulated globally by the endoge- nous Cxcl12 chemokine ligand distribution	78
3.2.2	Widespread chemokine receptor hyperactivation in absence of scavenger Cxcr7	82
3.2.3	In toto comparison of the effect of ligands and scavenger on Cxcr4b in vivo	86
3.3	Correlating scavenger expression pattern to its signaling impact . . .	87
3.3.1	Chemokine receptor turnover increase does not tightly corre- late with Cxcr7b expression profile	87
3.3.2	Modelling a potential long range Cxcr7b-Cxcr4b interaction .	89
3.4	Addressing impact of chemokine receptor hyperactivation on tissue positioning and morphology	90
3.5	Testing the role of desensitization in providing phenotypic robustness	96
3.5.1	Preventing Cxcr4b desensitization enhances the pLLP migra- tion phenotype in the absence of Cxcr7	97

3.5.2	Preventing Cxcr4b desensitisation does not lead to additional phenotypes in <i>cxcr7b</i> ^{-/-}	98
3.6	Materials and Methods	102
3.6.1	Zebrafish stocks	102
3.6.2	pLLP migration phenotype scoring	103
3.6.3	Light sheet microscopy	103
4	Discussion	105
4.1	Establishing a multi-view light sheet reconstruction pipeline for increased multi-view throughput and reconstruction quality	106
4.2	Building an in toto atlas to integrate expression, signaling and phenotype information	110
4.3	Loss of scavenger leads to embryo-wide hyper activation of chemokine signaling	115
4.4	Desensitization alone cannot explain morphological robustness to increased signaling in <i>cxcr7b</i> ^{-/-}	117
4.5	An opportunity to model receptor interactions	120
4.6	Future perspective	122
4.7	Concluding remarks	123
	Acknowledgments	125
	Bibliography	127

1 Introduction

The driving processes of embryonic development - such as cell proliferation, differentiation and migration - are tightly coupled to each other to orchestrate the transformation of the zygote into a multicellular organism. The developmental path of every cell is determined through interactions with other cells and the extracellular environment. Many of these interactions can extend from the cell to the tissue and organismal scale, mediated via long range signaling, tissue mechanics and cell movements. A process that integrates all of these aspects is collective cell migration (CCM), where cohesive groups of cells migrate to form organs of complex morphological shapes.

The study of complex cellular processes in vivo demands the development of new technologies. In recent years the advent of new imaging techniques, such as light sheet microscopy, also known as Single-Plane Illumination Microscopy (SPIM) has increased the capability to study developmental processes within their physiological spatial contexts. Multi-view light sheet microscopy enables embryo imaging at the cellular and organism scales simultaneously at isotropic resolution. While this has generally been used for high-data capture of small numbers of specimens, nonlinear image registration methods open up the possibility to 'multiplex' light-sheet microscopy and allow the integration of different types of data (e.g. gene and protein expression, activity reporters) across embryos and genetic conditions. Combining this emerging imaging modality with new fluorescent reporters will potentially allow the unprecedented mapping of processes such as cell signaling across whole embryos.

The focus of this thesis lies on combining and further developing aspects of these state-of-the-art methodologies to study how chemokine signaling, a key driver of cell migration, functions to guide CCM during embryonic development. This chapter introduces the concepts and methods required to then formulate this aim more precisely.

1.1 Tissue migration and chemokine signaling during development

1.1.1 Collective cell migration

Cell migration plays an important role in many processes such as the formation of complex organs during development, the defense against pathogens or cancer invasion. In multicellular organisms cells can migrate individually, e.g. in the case of leukocytes [120] or primordial germ cells [147], or collectively. Collective cell migration (CCM) refers to the ability of groups of cells to move together and simultaneously affect the behavior of each other [133] (for example over cell-cell junctions [108, 150]), which can orchestrate complex morphogenetic events. Some examples of CCM are depicted in fig. 1.1 and can exhibit different modes of migration including migration as epithelial sheets, in a stream, via sprouting and branching and more [87]. Importantly, CCM can be distinguished from other types of multicellular translocations such as invagination, intercalation or expansive growth among others, which do not rely on active migration [45].

Whether as individual cells or in the group, cell migration relies on the exertion of force onto the cellular substrate typically mediated by coordinated rearrangements of the cytoskeleton [86, 129]. Predominantly, dynamical cell shape changes are regulated by actin dynamics and involve the formation of cell protrusions or thin

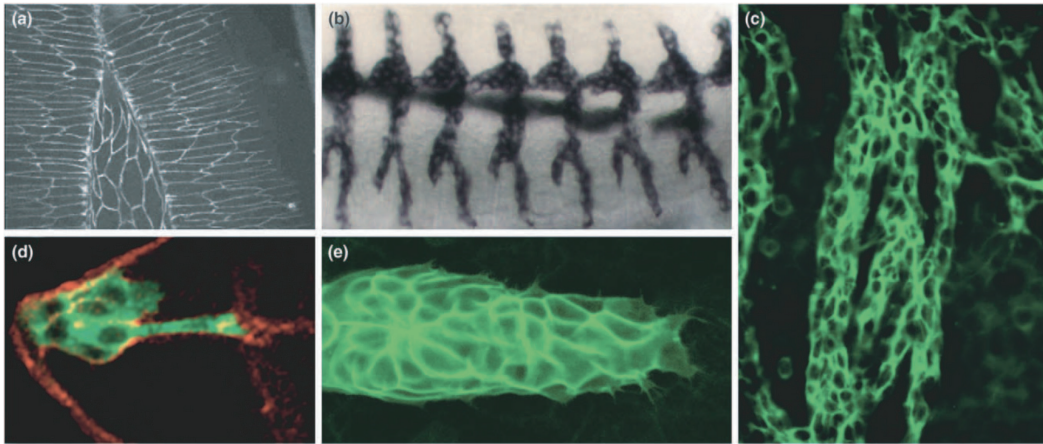


Figure 1.1 – Examples of collective cell migration during development: a) Epithelial sheet migration during dorsal closure in the drosophila embryo, b) sprouting and branching in the tracheal system, c) neural precursor migration in the rodent brain, d) drosophila border cells and e) the zebrafish lateral line primordium. Illustration taken from [88].

filopodia. While single cell migration is relatively well understood in many specific contexts, CCM is a much more complex process integrating interactions at the cell and tissue scale. One general principle underlying CCM is the subdivision of the collective into leader and follower cells, that can be distinguished by different molecular and morphological features [104]. While leader cells are generally responsible for responding to guidance cues and organizing the directed migration of followers via intercellular contacts, the concerted action of the entire collective is known to contribute to the migration process.

1.1.2 Chemotaxis in response to extracellular gradients

While in some cases cell migration is random or guided by intrinsic directionality [118], both individual and collective cell migration is typically directed by an extracellular guidance cue. These cues can take the form of light (phototaxis), electrical fields (galvanotaxis), in terms of substrate stiffness (durotaxis) [44, 110, 72] or, most relevant to this thesis, extracellular diffusible chemicals (chemotaxis) [172].

Chemotaxis is defined as the process by which a cell's directional movement is determined by gradients of chemoattractants. In order for cells or tissues to successfully perform chemotaxis, they must sense and react to an extracellular signal which are sensed by membrane proteins such as G-protein-coupled receptors or receptor tyrosine kinases [62, 2].

The presence of an extracellular gradient can induce the polarized activation of downstream signaling pathways that results in differential responses at leading and trailing edges of the cell that are required for directed migration. Interestingly, such polarized responses to chemoattractant can be strongly influenced by intrinsic polarities of the migrating cell or tissue itself, a prominent example for a collective being the lateral line primordium in the zebrafish embryo, which is further described in section 1.1.4 [167, 118, 40]. Therefore, the interaction between migrating cells and extracellular gradients is highly complex. Typically, chemotaxis is thought to occur along prepatterned extracellular gradients, however evidence is increasing that especially the intrinsic properties of migrating collectives play an important role in directing migration [132, 40].

The establishment of chemotactic gradients has been proposed to function by local production and subsequent diffusion in the extracellular space, such as in the case of morphogens in pattern formation [37, 30]. However, many geometrical and functional effects including hindered diffusion, binding, and many other regulatory interactions can influence the diffusion of molecules within the embryo, determining how gradients are established [30, 71]. In particular, concentration dependent degradation and sinks have been found to play an important role in establishing stable gradients [114, 6], presumably by ensuring that molecules diffusing in restricted spaces do not reach saturation. In addition, chemoattractants can be dynamically produced by tissues that are moving or changing in size, which adds another layer of complexity to understanding gradient formation. Unfortunately, low concentrations of diffusible molecules are difficult to visualize directly using microscopy, therefore

examining the role of gradients in vivo requires different approaches (see section 1.2.2).

1.1.3 Chemokine signaling during development

Chemokine signaling overview

A well-studied class of chemoattractants are chemokines. They form a family of structurally related, small cytokines or signaling proteins (8-10 kDa in size), which had been originally discovered for their role in the immune system where they induce chemotaxis in leukocytes [116]. However, in recent years chemokine signaling has also been shown to play an important role during embryonic development, where chemokines guide neuronal, neural crest and germ cell migration, regulate the patterning and remodeling of the vascular system and are involved in muscle formation, amongst other processes [16, 23, 21, 128, 105, 90, 28]. Chemokines are secreted by producing cells and exert their function by binding to their counterpart chemokine receptors, seven-transmembrane domain G-protein coupled receptors which by conformational change upon binding activate downstream signaling effectors [79]. Interestingly, chemokine receptors are often able to bind to more than one chemokine ligand and vice versa. Also, prolonged exposure to ligand typically leads to a decrease of receptor responsiveness, which is a feedback mechanism termed desensitization [67].

CXCR4 / CXCL12 signaling

The most evolutionarily conserved chemokine is CXCL12 (also known as stromal derived factor 1 or SDF1), which binds to the well studied and medically relevant CXCR4 [43]. A mutated form of CXCR4 leads to WHIM syndrome, a disease characterised by the effects of impaired leukocyte migration [9]. Also, increased levels of CXCR4 are associated to increased cancer progression [109]. During development,

CXCR4/CXCL12 signaling is involved in most of the above mentioned processes including guiding the migration of the posterior lateral line primordium in the zebrafish embryo [52].

Importantly, upon binding of its ligand, CXCR4 is rapidly phosphorylated and undergoes internalization mediated by endocytosis [143, 54], a process termed desensitization. The interaction activates both G-protein-dependent and independent (Jak/STAT and β -arrestin) downstream signaling pathways [19]. After internalization, the receptor is either degraded [99, 14] or recycled back to the membrane [83], and the route of intracellular trafficking can be regulated by post-translational modifications of amino acids in the receptor's C-terminal tail. Indeed, mutations in the C-terminal domain of the receptor can lead to defects in receptor desensitization which results in defects in the migration of neutrophils in WHIM-syndrome patients [9].

Interactions with the atypical chemokine receptor CXCR7

In addition to canonical chemokine receptors, there is an additional structurally related class - termed atypical chemokine receptors - that can bind to chemokines but are however unable to activate G-protein mediated downstream signaling [48].

CXCR7/ACKR3 is an atypical receptor that binds CXCL12 ligand with high affinity [8]. CXCR7 exerts its function in several ways, including both CXCR4 dependent and independent mechanisms (see fig. 1.2 for a schematic) [124, 8]. CXCR7 can heterodimerize with CXCR4, modulating its signaling activity and chemotactic function in a seemingly chemokine level dependent manner [89, 35, 141].

More prevalently, CXCR7 can also modulate CXCR4 signaling activity and function in cell non-autonomous fashion by sequestration of the CXCL12 ligand. CXCR7 can successfully compete with CXCR4 for CXCL12 because of its higher affinity and recycling rate [18]. This sinking activity has an important function in vivo, namely the establishment of chemokine gradients due to CXCR7 sinking activity. For example,

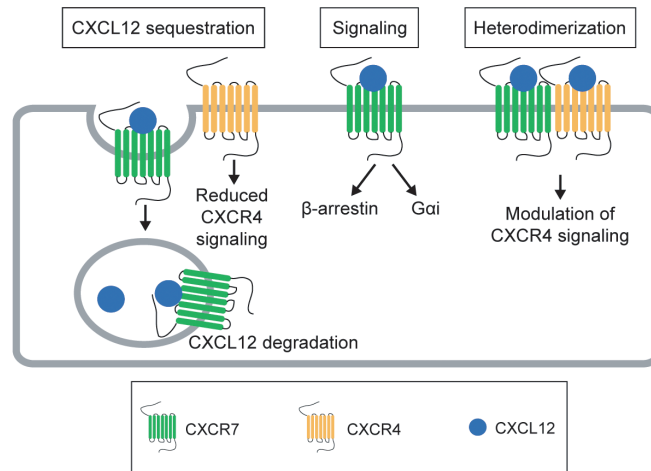


Figure 1.2 – The function of CXCR7 relative to CXCR4: Internalization of CXCL12 leads to reduced ligand levels and CXCR4 signaling. Alternatively, CXCR7 can signal G-protein independently or receptors can heterodimerize, leading to a modulation of CXCR4 signaling. Illustration taken from [39].

PGC migration during zebrafish development requires CXCR7 mediated receptor internalization by somatic cells [17] to stabilize its chemokine gradient. Another very clear unraveling of the scavenging function of CXCR7 in modulating CXCR4 activity by shaping the extracellular ligand distribution has been shown for the pLLP migration in zebrafish, which will be discussed in the next section. Other examples of functional CXCR7 sinking activity include neuronal migration in vivo in zebrafish [91, 31] and mouse [138, 106].

However, it has not been demonstrated that CXCR7's scavenger activity alone is sufficient to fulfill its function in every context where this receptor is known to be required. Since the three mentioned interaction mechanisms are not mutually exclusive, their relative contribution remains open in many contexts. Also, the function of CXCR7 mediated modulation of CXCR4 signaling might vary, since a clearance of the ligand has been proposed to, rather than decreasing CXCR4 signaling, ensure continued signaling by preventing excessive CXCR4 internalization [1].

1.1.4 Studying chemokine signaling in the zebrafish embryo

The zebrafish embryo represents a popular model system for studying cell migration and chemokine signaling *in vivo*. This is due to the fact that cell migration studies are typically advanced by the ability to perform live microscopy, for which the transparent and easy to handle zebrafish embryo is optimally suited. The zebrafish also represents a genetically readily accessible vertebrate model system. Interestingly, due to gene duplication events (most probably during teleost evolution), many chemokine ligands and receptors are represented by more than one gene in zebrafish. So is the case for all of CXCL12, CXCR4 and CXCR7, which can be found in duplicates (nomenclature: CXCL12a and CXCL12b). CXCR4a is reported to bind to CXCL12b [15] while CXCR4b and CXCR7b can bind to both ligands, potentially creating a highly promiscuous interplay of this signaling axis in zebrafish. Interestingly though, CXCL12a and CXCL12b show different binding affinities to receptors [15] and CXCR4a and CXCR4b differ largely in their expression domains during development [27]. However despite their split nature both CXCR4 receptors are highly expressed in the zebrafish embryo.

Self-generated chemokine gradients

An intriguing and well studied example of a collectively migrating tissue in which all three CXCR4 / CXCL12 / CXCR7 receptors play an important role for collective cell migration is the posterior lateral line primordium (pLLP) in the zebrafish embryo. The pLLP is a group of approx. 100 that migrates along the lateral line of the embryo, depositing neuromasts on its way.

This migration is guided by a narrow ‘stripe’ of CXCL12 expressing cells, which the primordium detects via the expression of the receptor CXCR4b [53]. However, in the absence of the primordium the chemokine is present in constant concentrations along the lateral line. Donà et al. and Venkiteswaran et al. have shown that

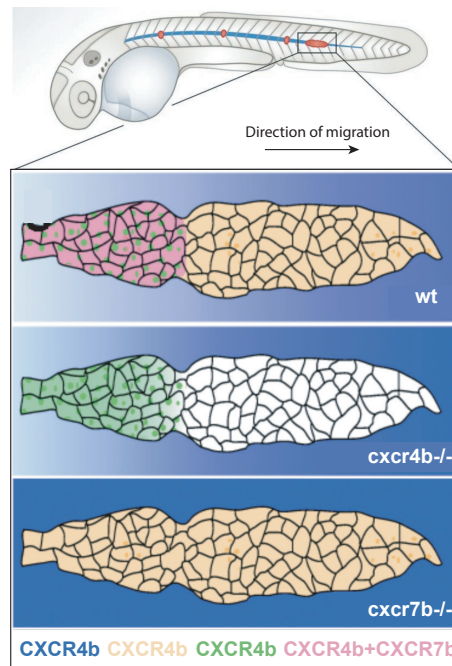


Figure 1.3 – By selectively expressing the scavenging CXCR7b in its rear, the migrating pLLP self-generates its CXCL12a gradient which is interpreted by CXCR4b (adapted from [20] and [39]).

nevertheless CXCR4b responds to a chemokine gradient during migration. This gradient is established by a polarized expression of CXCR7b located in the rear part of the migrating tissue, which selectively internalizes the chemokine [40][160].

While CXCR7 has been involved in the formation and stabilization of chemotactic gradients in other contexts, this is the first demonstration that this mechanism can enable a migrating tissue to form its own chemotactic gradient and therefore determine its own directionality. This mechanism has been predicted to play a role in more developmental contexts, which so far however remain open. Also, self-generated gradients could potentially be employed by migrating tumors, a context in which CXCR7 has been heavily involved.

Importantly, the findings of Donà et al. has been made possible by establishing tandem fluorescent timers as a novel fluorescent readout for the visualization of chemokine receptor signaling activity, which will be introduced in section 1.2.2.

1.2 Visualizing cell signaling in vivo

Organisms employ highly dynamical intercellular signaling to orchestrate interactions between cells and tissues, which need to effectively respond to an ever changing environment in a tightly regulated manner. Although information about signaling networks is increasingly abundant, an understanding of the spatial and temporal regulation of these interactions has lagged behind [70]. In other words, biological function is only determined from precisely how organisms employ the diverse signaling pathways at their disposal. Therefore, these can only be studied in the native context of living cells, where signaling networks together with their regulatory mechanisms are retained in their spatiotemporal organization.

1.2.1 Fluorescent readouts of signaling activity

Advances in both microscopy technology and the design of novel fluorescent probes has in recent years led to the development of many diverse signaling biosensors. These can report on the activity of a variety of signaling molecules including kinases, phosphatases, GTPases and many more (for reviews see [11, 113] or [136]). While the targeted observation of molecules of interest started with immunofluorescence in the early twentieth century [29] and the first important calcium signaling activity readout Fura-2 [50] was achieved using chemical dyes, genetically encoded fluorescent reporters now enable the minimally invasive observation of signaling events in living organisms.

Central to the functioning of a biosensor is its targeted member of the signaling pathway it reports on, which is fused to a fluorescent reporter consisting of one or more fluorophores. In its simplest form, a normal fluorophore such as GFP fused to a protein with a functional binding domain can serve as a biosensor (for a schematic see fig. 1.4). In this case, the relocation of the protein over time, for example from the cytoplasm into the nucleus or to the membrane can function as

an activity readout. Using this general principle, the formation of protein clusters during phase separation has recently been exploited to reveal signaling oscillations in the activity of G-protein coupled receptors [171]. Another category of biosensors is characterised by the exploitation of the photo-physical properties of a chromophore, in which a target induced switch can lead to a change in its fluorescent intensity. A very prominent example for such a sensor is the calcium sensor GCaMP [112], which in recent years has been used to record the brain-wide neural activity of living animals [125]. Also, new biosensors of small GTPases could be used to characterize cell dynamics in vivo [73]. The most prominent and diverse category of biosensors relies on Förster Resonance Energy Transfer (FRET), which refers to the transfer of energy between two fluorophores, a donor and an acceptor, depending on their relative distance or orientation. To create a biosensor, a target protein is fused to a donor and an acceptor. When the relevant signaling event occurs, the target undergoes a switch which leads to a change in the FRET efficiency between the two fluorophores [85]. The advantage of these biosensors lies in their modular design which can be adapted to many contexts, which has led e.g. to the ability to measure membrane tension in living cells [49]. However, a disadvantage of FRET sensors is their relatively low signal to noise ratio.

In many signaling pathways, such as in the case of G-protein mediated signaling [79] or Epidermal Growth Factor (EGF) [142], protein stability and intracellular trafficking is tightly linked to signaling events and can act as a proxy thereof. When proteins are trafficked or degraded in response to signaling, a fluorescent reporter which changes its fluorescent output either after an intervention or over time can be used to gain insights into these dynamics. Thus, photo-switchable fluorophores can be used to perform pulse-chase experiments: After permanently changing the fluorescence attached to a target protein, its behavior or that of the pool of labelled proteins can be monitored and contrasted with a model of the underlying process. Using this principle, protein dynamics could be visualized with subdiffraction resolution in living cells [46]. A disadvantage of this approach consists in the necessity to

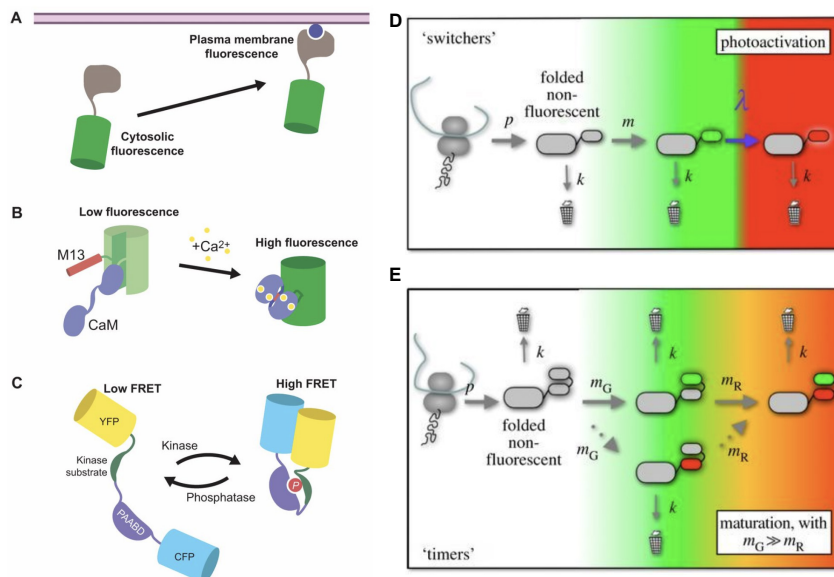


Figure 1.4 – Different strategies to visualize signaling in vivo. a) Over monitoring the relocation of the fluorescent labeling of a binding domain, b) modulation of fluorescence by induced conformational changes c) FRET sensitivity to changes in the spatial proximity of nearby components, d) modeling the outcome of microscopy-based pulse-chase experiments or e) inferring protein age using (tandem) fluorescent timers. Illustrations adapted from [136] and [78].

perform measurements over time. This can be avoided using fluorescent reporters which change their color over time. These so called fluorescent timers have first been used to study promotor transcriptional activity [149, 107]. The suitability of a given timer for studying protein dynamics in a certain context is strongly influenced by the timescales involved in its fluorescent change. Therefore, the development of different variants with different kinetics has enabled the study of a broader range of processes [146]. More recently, fluorescent timers composing of two proteins have emerged [69], which bring many advantages to fluorescent lifetime imaging and will be discussed in the next section.

Finally, it is important to note that the choice of a biosensor to study a given signaling pathway is constrained, since its applicability depends on many factors. Ultimately, a fluorescent contrast needs to reflect a change in the signaling state,

which strongly depends on the dynamic properties of the fluorescent reporter in interplay with its targeted process. The dynamic range of a FRET sensor is strongly determined by the proximity change between acceptor and donor induced by the signaling event, and the FRET efficiency of the chromophores. Similarly, in the case of a fluorescent timer the involved timescale determines its applicability to studying a given process.

1.2.2 Tandem fluorescent protein timers to study receptor dynamics

In recent years, a new category of fluorescent timers, the tandem fluorescent protein timer (tFT), has emerged in which the fluorescent reporter is composed of two fluorescent proteins fused to the target, instead of a single one [69]. The change of fluorescence over time is achieved by the fact that fluorescent proteins in different colors fold with different maturation rates after translation. Therefore, only after a characteristic time will the fluorophore contribute to the fluorescence captured by the microscope. When observing this stochastic process in a population of receptors in a living cell, the ratio between the intensities of the slow and fast maturing fluorophores will be indicative of the time that has passed since protein translation, i.e. protein age (see fig. 1.5 for a schematic). While in a previous approach two separate fluorophores were produced using bicistronic expression [25], if both proteins are fused to the target even subcellular distributions of protein ages can be measured [69]. This approach has several advantages over monomeric fluorescent timers, including that standard fluorophores that are optimized regarding brightness, phototoxicity and photobleaching can be used, such as GFP, mCherry, tagRFP, etc. In addition to better imaging properties, the possibility to modularly exchange the fluorophores allows custom engineering of the timescales at which the resulting fluorescent timer operates.

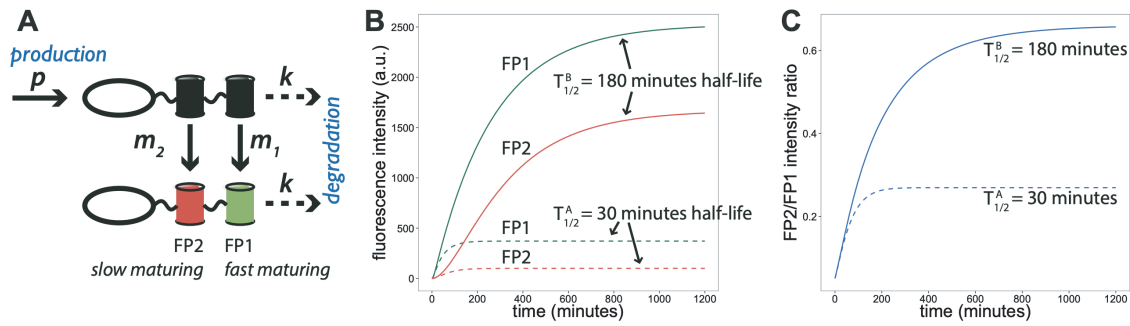


Figure 1.5 – Tandem fluorescent protein timers. A) The target protein is fused to two fluorophores folding at different maturation rates ($m_2 \gg m_1$). These kinetics can be modeled to measure protein degradation rate (see text). B) Modeled intensities over time from a protein population. Different combinations of fluorophores with different maturation rates lead to different curves. C) The resulting fluorescent ratios are indicative of protein half life (or the degradation rate). Illustrations taken from [13].

The fluorophore kinetics of tFTs can be mathematically modeled as depicted in fig. 1.5 assuming a one step maturation process. For each of the fluorophores, this leads to the set of equations:

$$\begin{aligned}\dot{N}_i^0 &= p - (k + m_i)N_i^0(t) \\ \dot{N}_i &= m_i N_i^0(t) - k N_i(t)\end{aligned}$$

where N_i^0 and N_i are the molecular populations of the immature and mature fluorescent protein with maturation rate m_i and p and k are the production and degradation rates of the fusion protein ($i \in \{0, 1\}$ for FP1 and FP2). While these equations have a time dependent solution, very interesting is the steady state solution for the visible population N_i :

$$\lim_{t \rightarrow \infty} N_i(t) = \frac{pm_i}{k(k + m_i)}$$

As the production rate appears as a simple factor, the ratio between the two populations does not depend on it and, assuming known maturation rates, can therefore be used to infer the degradation rate of the fusion protein. This is very useful

for in vivo studies, as production rates are typically unknown. However, it has to be noted that, just as timer sensitivity in general, the time reaching steady state strongly depends on the slow maturation rate and can exceed its maturation time [13]. Alternatively, timer readout can be measured over time, which allows the estimation of full protein dynamics over time, which however has to be performed before significant photobleaching.

Thanks to their versatility and properties, tFTs have been successfully used to study protein dynamics in vivo. Examples include a proteomic screen for studying protein glycosylation in yeast [22] and its use for discriminating between different models of bicoid gradient formation during early drosophila development [22].

Most importantly for this work and as mentioned before, tFT have recently been established as a tool to study chemokine signaling in the developing zebrafish embryo [40]. Specifically, tFTs have been used to show that the pLLP can self-generate a chemokine gradient as it migrates along the lateral line (refer to section 1.1.4 for details). To do so, Dona et al. targeted the signaling receptor of the primordium, CXCR4b, and attached to it a tFT consisting of sfGFP and tagRFP fluorescent proteins. As CXCR4 is internalized and degraded upon ligand binding, degradation was indicative of receptor-ligand binding and signaling rates (see fig. 1.6a). And as previously described, degradation could be measured using the steady state tFT readout. Therefore, the tFT could be used to compare chemokine availability and receptor signaling along the direction of migration of the primordium, revealing a gradient from the trailing to the leading edge (see 1.6c). Importantly, despite the attachment of two fluorescent proteins, the CXCR4b receptor which was expressed using a bacterial artificial chromosome (BAC) could guide primordium migration in the absence of endogenous CXCR4b, indicating a fully functional receptor. Further, as the primordium represents a tissue with a clear polarity and elongated shape, measurements could be normalised and compared between wild type and different mutant backgrounds: this showed that the clear gradient exhibited in the wild type vanished in *cxc7b*^{-/-} mutants (fig. 1.6b). This provided important evidence that

the expression of CXCR7 can shape extracellular chemokine cues in vivo and for the first time showed the ability of a collectively migrating tissue to perform this autonomously.

In summary, tandem fluorescent lifetime reporters have emerged as a powerful tool to study protein dynamics in vivo and can visualize and quantify chemokine receptor activity in the zebrafish embryo. The thus revealed mechanisms have been proposed to potentially be employed by other developmental processes as well [40, 159, 155].

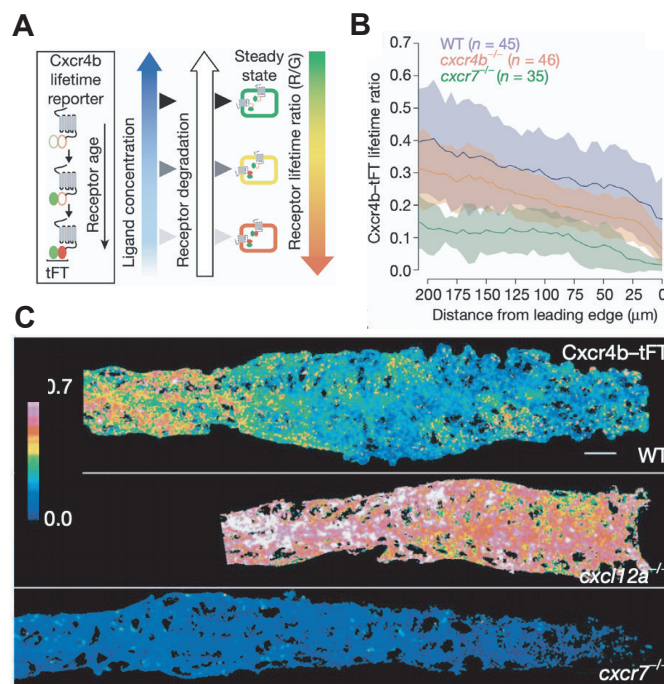


Figure 1.6 – Tandem fluorescent protein timers to study CXCR4 receptor turnover in the pLLP.

A) tFT ratios as a readout for CXCR4 degradation and ligand binding.

B,C) This allows studying signaling gradients along the primordium (see text).

Illustrations adapted from [40].

1.2.3 Spatial and temporal multiplexing of fluorescent readouts

The previously described fluorescent readouts allow studying signaling events and dynamics in relevant in vivo systems. However, signaling networks often comprise the interactions between many signaling components which cannot be studied simultaneously using microscopy approaches. Typically, not more than three or four fluorophores can be spectrally resolved without risking significant overlap of the involved excitation and emission ranges. This is especially critical when using fluorescent readouts comprised of more than one color such as FRET sensors or tandem fluorescent timers, which require precise quantifications occupying a large part of the available spectrum.

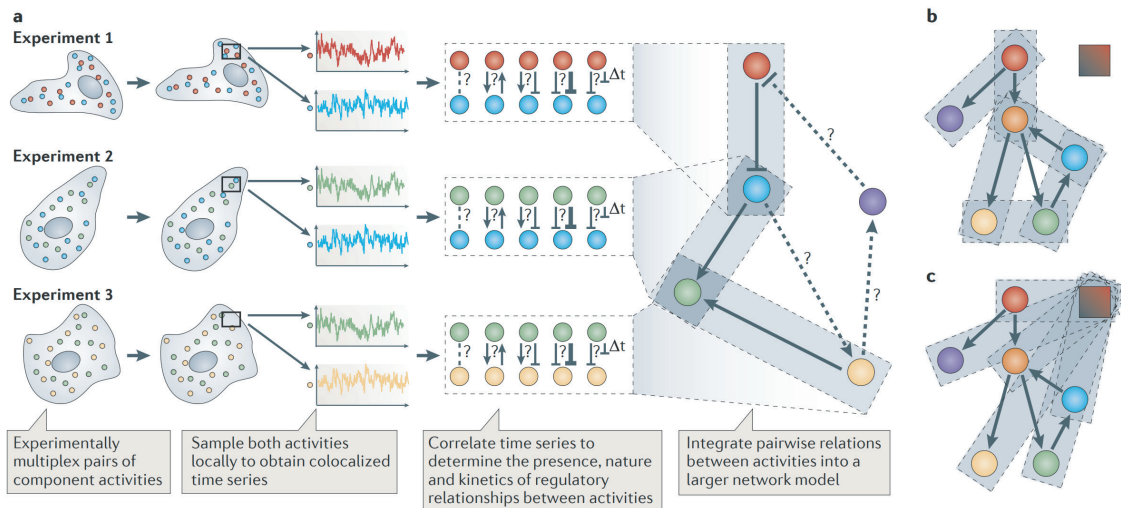


Figure 1.7 – Spatiotemporal multiplexing to study signaling networks in vivo. Illustration taken from [165]

A possible solution to this problem consists in the so-called 'multiplexing', which here refers to the spatial and/or temporal normalization of microscopy data. An area of research where this approach has been popular is the study of components near the cell membrane such as GTPases, their function and interactions during cell migration, polarity establishment and protrusive behavior [96, 165]. Here, the general principle consists in imaging two readouts in different colors at the same time,

to then extract temporal correlations between the two measured signals (see fig. 1.7 for a schematic). From these correlations conclusions about the regulatory relationships between the two components are drawn and then integrated into a larger signal network model in a pairwise manner. Using this method data from completely orthogonal experiments can be integrated, including the comparison between different genetic backgrounds and optogenetic perturbation scenarios [139].

Atlas frameworks

While in the above described approach signaling relationships between dynamic intracellular components are inferred, relationships between components on the organism scale have been addressed using spatial normalization. As an example, in the embryonic nervous system, the previously mentioned GCaMP biosensor can be used to perform calcium imaging to record neuronal activity at cellular resolution across the entire brain. However, this is difficult when interested in the neuronal activity of freely behaving embryos, in which case reporters exist to visualize on past neuronal activity within a given time window [166, 12]. To make sense of the activation of these reporters, their signals need to be correlated between separate experiments and ideally neuronal activity can be mapped onto an anatomical reference. This can be achieved using nonlinear image registration of brain recordings [125], which maps samples acquired in different experiments into the same spatial coordinate system (see fig. 1.8). Sometimes this approach to integrate information from separate samples into a spatially normalized mapping is referred to as an 'atlas'.

Computational algorithms for the spatial normalization of 3D images originate from the neuroimaging and medical fields, being optimized for PET or MRI images (for an extensive overview see [115]). The core challenge in placing samples into a common coordinate system lies in the pairwise mapping of samples onto each other or between a sample and a template image. Whether this is successful or not depends on both the transformations searched for and the variability exhibited by the samples

to be registered. Some of the earliest adaptations of nonlinear image registration to fluorescence images in developmental biology have been applied to organisms and tissues exhibiting relatively stereotypic development such as the drosophila brain and annelid worms [26, 117, 152], for which linear transformations or parameterizations with few degrees of freedom could be assumed as transformation models. More sophisticated transformation models were then applied to register the morphologically more variable vertebrate zebrafish brain [131, 125, 100]. Recently, the adoption of state-of-the-art image registration methods performing diffeomorphic symmetric normalization [5] has enabled another jump in the registration quality of live zebrafish brain recordings [101, 51, 84]. Nevertheless, it is important to note that nonlinear image registration of biological samples remains a difficult and rather poorly defined task [98], as often it is difficult to properly assess the quality of its outcome due to the lack of ground truth. However, the currently achieved registration quality provided by freely available tools on some fluorescent datasets [5] has been shown to be sufficient to perform automated and statistically significant phenotyping (for further details refer to section 2.2.4) on some fluorescence zebrafish brain datasets [51] and interestingly also in toto X-ray recordings in the embryo [38] and even adult zebrafish [164].

Finally, spatial normalization for creating atlas frameworks can be a useful tool in developmental biology to integrate and visualize spatial information about targets of interest obtained from separate experiments. So far, an interesting use case of atlases in the zebrafish embryo has been the development of publicly available databases for comparing and mapping the expression of a plethora of markers in the embryo [131, 125, 101, 84]. Mining data integrated by these tools might lead to new discoveries based on already existing data.

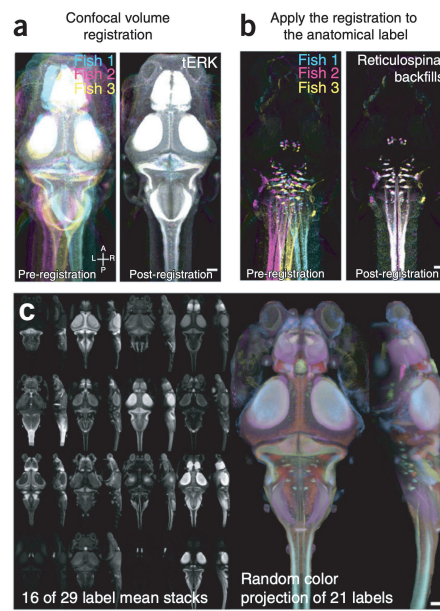


Figure 1.8 – Spatial normalization and multiplexing of fluorescent labels in the zebrafish brain (or: the creation of a brain 'atlas'). a) Nonlinear image registration of a reference label is used to map samples onto each other. b) The obtained sample transformations are applied to other channels recorded in parallel. c) Many expression profiles can be mapped onto the atlas. Illustration adapted from [127].

1.3 In toto multi-view light sheet microscopy

As perhaps the most widespread tool in biology, the light microscope provides a magnified view on the processes of life. In modern molecular biology, fluorescence microscopy in combination with genetically encoded reporters, GFP and its spectral variants, enables the observation of protein localization patterns in living organisms [24]. Optical sectioning allows attributing a fluorescent signal to precise locations within the sample and is typically obtained by using laser scanning microscopy (LSM) with confocal detection through a pinhole [61] or by exploiting nonlinear optical properties of the fluorophores using multi-photon [36]. Although LSM achieves high spatial resolutions, its limitations are given by a limited penetration depth into scattering samples and an axial resolution being 3-4 times lower than the lateral resolution. These effects together limit the usability of LSM when intending to study large specimens such as developing embryos in detail. A solution to both of these problems consists in acquiring images from multiple imaging angles and positions, thereby optically penetrating the sample from different views and varying the lateral and axial directions relative to the sample [81]. A microscopy technique especially suitable for use in a multiple view setting is light sheet microscopy, which enables special sample mounting and fast image acquisition speeds [60]. In recent years, the ability of multi-view light sheet microscopy to reconstruct embryonic development in high spatial and temporal resolution *in toto* has had a big impact on developmental biology.

1.3.1 Principles of light sheet microscopy

While in point scanning LSM both the illumination and detection of the fluorophores to be visualized occurs using the same optical axis, the defining property of light sheet microscopy consists in orienting illumination and detection at a right angle. In this configuration, a given plane orthogonal to the detection axis is illuminated by a

thin sheet of light, which coincides with the focal plane of the detection objective (see fig. 1.9). Alternatively, light sheet microscopy is termed Selective Plane Illumination Microscopy (SPIM), illustrating the plane-wise excitation of fluorophores which is then coupled to an epifluorescent detection using a digital camera. For obtaining three dimensional images, the sample is translated in the axial direction to relocate under the focal plane in several positions.

Because SPIM acquires three dimensional images by tiling 2D planes acquired on a pixel-array detector, imaging speeds are strongly increased compared to standard point scanning confocal microscopy or even spinning disk approaches [97]. Another benefit of optical sectioning using light sheets is the more efficient light deposition on the sample, which is illustrated in fig. 1.9. While in point scanners out-of-focus light is constantly illuminating the sample, a light sheet setup ideally only illuminates those regions of the sample containing the fluorophores which are currently read out. This leads to strongly reduced phototoxicity and fluorophore bleaching, which enables the highly resolved long term imaging of light sensitive developing embryos.

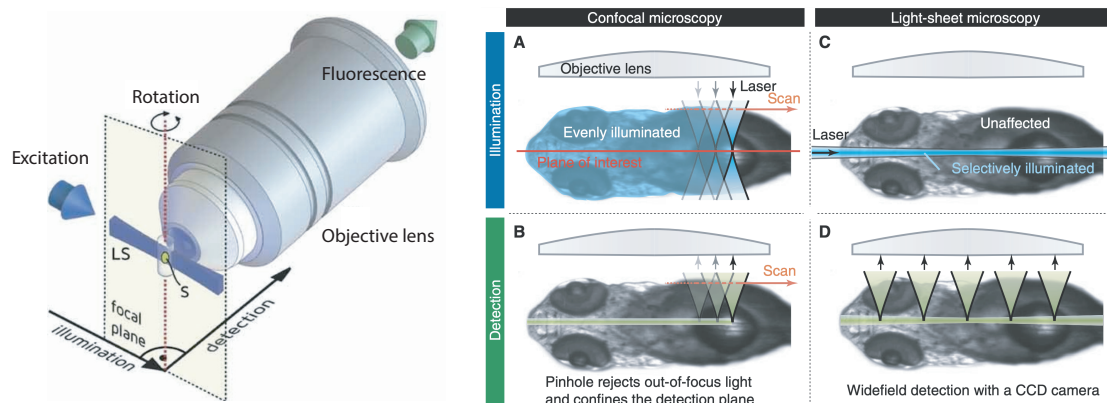


Figure 1.9 – Schematic illustrating the principle of light sheet microscopy: By optimising optical sectioning, phototoxicity and bleaching are reduced and image acquisition speed is increased compared to confocal microscopy. Illustrations adapted from [161] and [59].

Also, optical sectioning using thin light sheets can yield superior axial resolution compared to confocal microscopy. This is because the effective point spread function (PSF) of the microscope can be regarded as the multiplication of an illumination and detection PSF, with the former having lower extensions in the axial detection direction. However, optically the length and thickness of gaussian beams are coupled, leading to a limit of the available extent of thin light sheet, effectively forcing a compromise between the field of view and spatial resolution. Also, for this reason the optical resolution in SPIM can vary significantly within a given imaging plane. In the direction orthogonal to both illumination and detection in contrast, light sheets can extend indefinitely by digitally scanning the gaussian beam in this direction [66].

To enlarge the field of view and increase the spatial resolution achieved with light sheet microscopy, many variants of light sheet microscopes exist and both the illumination and detections paths are optimized in ongoing research [65]. In light sheet engineering, the limits of optical penetration imposed by light scattering and aberrations due to refractive index heterogeneities are addressed by employing multi-photon light sheets [154] or alternative, self reconstructing beam modes [41]. Alternatively, the detection path can be synchronized with modulations of the illumination for discarding out-of-focus light with confocal principles [144, 34] or by application of structured illumination patterns [65].

1.3.2 Multi-view reconstruction

For imaging large embryos such as the zebrafish or drosophila embryo, the arguably most important variant of light sheet microscopy is its extension to multi-view imaging [60]. Thanks to the narrowing of the PSF due to the uncoupled illumination and detection arms, SPIM works well with low numerical aperture objectives, which can have large working distances and therefore leave sufficient space for sample manipulation. Thus, large samples can be rotated in order to be imaged from different

angles (typically around a vertical rotation axis to minimize distortion effects). Another reason for the suitability of light sheet microscopy for multi-view imaging is the fast imaging speed, which is critical when imaging a living sample several times. Typical multi-view setups allow long range translations of the sample to acquire image stacks at multiple positions, which can be important for *in toto* imaging of elongated examples such as the zebrafish embryo. However, for two important reasons imaging embryonic development inherently benefits from sample rotation (illustrated in fig. 1.10):

1. Superior sample coverage: By sequentially imaging large samples from different angles, full surface coverage and optimized sample penetration can be achieved.
2. Improved axial resolution: The inferior axial resolution can be compensated for by sampling at different angles, thus acquiring complementary images regarding their resolutions in the different directions.

Both of these points depend on the computational reconstruction of a single, high quality image stack from several multi-view acquisitions. As a first step this involves multi-view registration, referring to the establishment of correspondences between image locations in the different views. This is typically achieved using fiducial markers [80, 123, 82] in the form of fluorescent beads to guide the alignment process. These are either embedded into the sample or acquired independently of the original sample in a second acquisition using identical microscope settings. Optionally, a subsequent content based image registration step is performed. To account for most distortions between different acquisitions, a linear affine transformation is typically used [80]. For more details on multi-view registration see section 2.1.1, where an optimization of the multi-view registration workflow is presented.

While the registered views could simply be averaged to create a final output stack, more sophisticated methods are required to exploit the advantages of multi-view imaging and create an ideally isotropic high quality output stack. To account for different sample coverage in different views, stitching [82] or content based weighting

[123] can be used. Here, the idea is to fill each region of the output stack with averaged information from the view or views exhibiting highest image quality. These approaches however do not significantly improve axial resolution. A powerful approach for improving axial resolution is multi-view deconvolution [80, 121], which in an iterative process attempts to recover the fluorophore distributions present in the sample before being distorted by the microscope's PSF. The latter is assumed to be known, which represents the main difficulty of this approach as the PSF can significantly vary across the field of view and within the sample. In practice, the PSFs are either determined theoretically or measured using fluorescent beads [148]. However, the PSF degrades within the sample and is difficult to estimate, which is why multi-view deconvolution is limited for large scattering samples. To address this issue, in section 2.1.2 we propose to combine content based weighting with multi-view deconvolution to only let regions of least PSF degradation contribute to the final multi-view reconstruction.

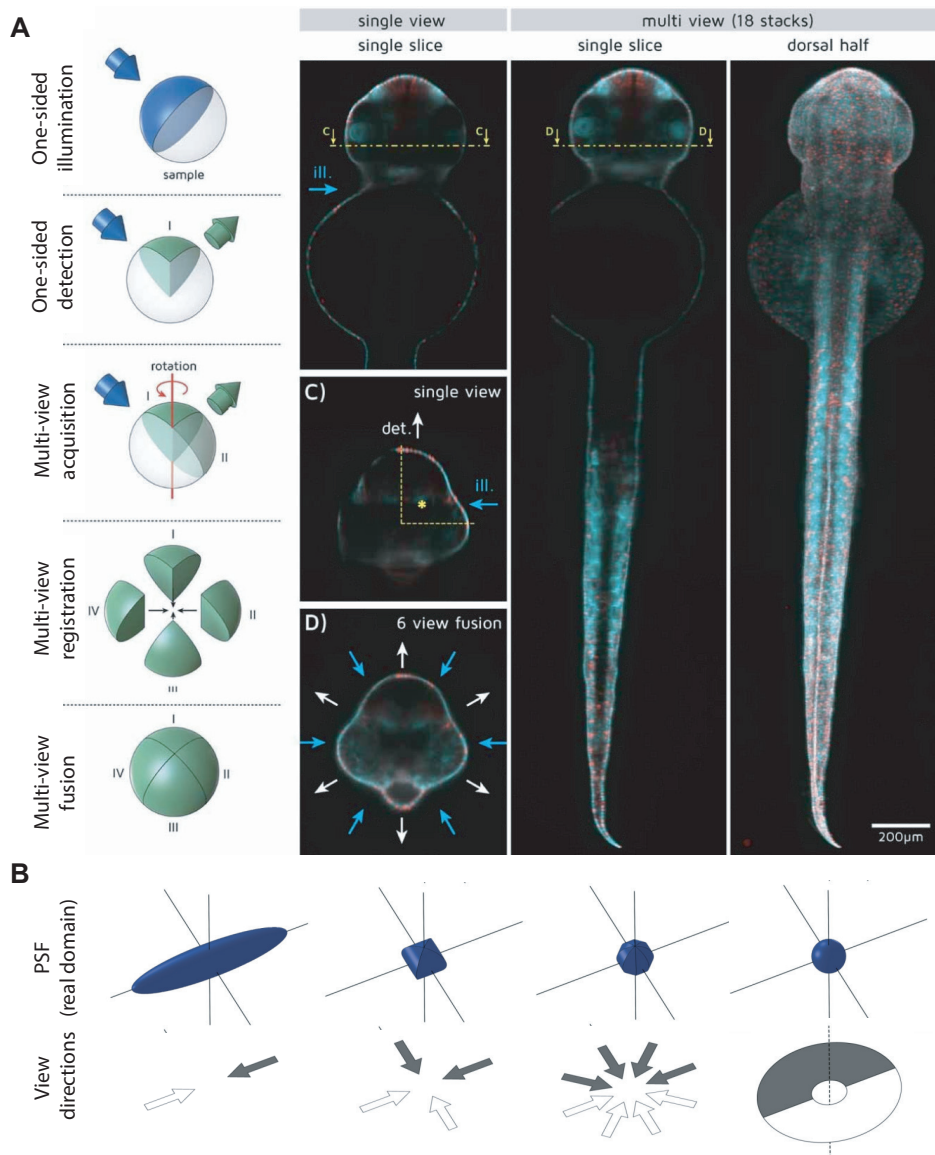


Figure 1.10 – Benefits of sample rotation for multi-view reconstruction. A) A given region of the embryo needs to be accessible by both illumination (blue) and detection (green) to be acquired with good image quality, typically yielding a configuration of sample quadrants. Due to the limited sample penetration of both optical arms, rotation optimizes sample coverage. Multiple view acquisitions are subsequently registered and fused, yielding a high quality output stack. The images on the right exemplify the *in toto* multi-view reconstruction of a zebrafish embryo. B) Axial resolution also benefits from sample rotation: by sampling from different directions, the large axial extent of the single-view PSF is improved upon after multi-view reconstruction by incorporating complementary lateral information. Illustrations adapted from [58] and [81].

1.4 Aim

The overall aim of this thesis is to gain a systems level understanding of chemokine signaling activity and function during development. This broad aim can be subdivided into a biological and a methodological aim. The concrete biological question underlying this work addresses the interactions between chemokine receptors and the impact these interactions have at the tissue and organismal scale. Recently, tissues have been identified in which the expression of the scavenger CXCR7 is critical to ensuring CXCR4 driven functions during collective cell migration by shaping the extracellular ligand distribution. This defies the view that chemokine activity and function is governed by prepatterned extracellular gradients. Instead, the dynamic remodeling of the signaling environment might play an important role in many processes. How prevalent is this role and in which ways do receptor interactions guide cell and tissue behavior during embryonic development?

Addressing this explorative question is supported by a methodological objective: The construction of an analysis framework to study chemokine signaling interactions in a systematic way (see fig. 1.11 for a schematic representation). On one hand advances in optical microscopy allow the visualisation of embryonic development bridging cellular and organismal scales, while on the other cell biological studies use novel fluorescent readouts to perform detailed studies of protein dynamics in cells and tissues of interest. My methodological aim is to combine multi-view light sheet microscopy, tandem fluorescent lifetime reporters and nonlinear image registration to create a computational framework that integrates and maps information about the expression and signaling activity of chemokine signaling components in different genetic backgrounds. Using automated morphometry, these maps can further be complemented by an analysis of morphological phenotypes providing insight into cellular function. This framework will be applied to study the impact of chemokine scavenging on the zebrafish embryo and could perspectivevely serve as a basis for

addressing other questions benefitting from integrated maps of cellular activity and function.

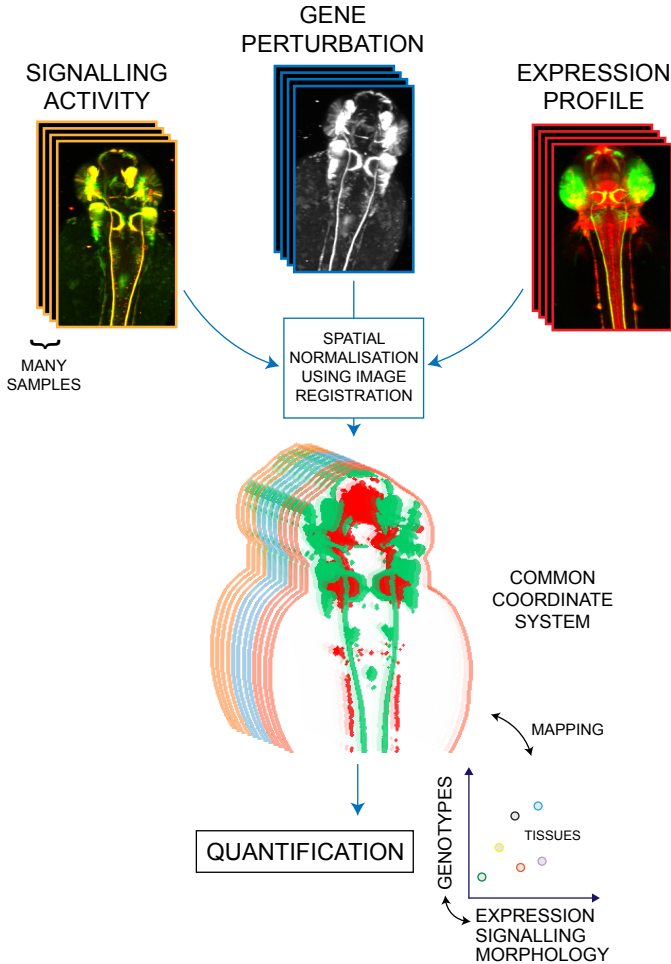


Figure 1.11 – Schematic of the methodological aim: A spatial normalization framework to quantify chemokine activity and function

2 Method development for in toto image quantification

In order to probe chemokine signaling in an in toto context, multi-view panoramic fluorescent data from zebrafish embryos was acquired and analyzed. This section describes the development of image processing and analysis methods enabling the high throughput analysis of many large specimens. Sections 2.1.1 and 2.1.2 describe preprocessing pipelines for the efficient use of image data obtained from multi-view SPIM microscopes. Building up on this, sections 2.2.1 to 2.2.4 describe the development of an atlas framework which allows for the combined analysis of many in toto samples, representing different biological replicates and genetic perturbations, by placing these into a common reference space.

2.1 Multi-view image reconstruction

2.1.1 Robust content based multi-view image registration

The reconstruction of a high quality image stack after acquiring data from a multi-view light sheet microscope starts with the registration of the different imaging views onto each other. This means to find the affine transform that establishes the correspondence between the physical coordinates in different views. Generally, this is achieved with the help of fiducial markers [123, 148, 82], that are embedded into

the imaging medium and acquired together with the sample. The markers are then segmented and the affine parameters are obtained as the solution of a point set registration problem.

This approach has several disadvantages. Special sample preparation is required and the fields of view comprise of at least a four times increase in sample volume to be imaged (see Fig. 2.1). This increases acquisition times and data storage demands considerably. To speed up and optimize this process, here a robust image processing pipeline was developed to perform multi-view registration independently of fiducial markers, while at the same time achieving high quality registrations.

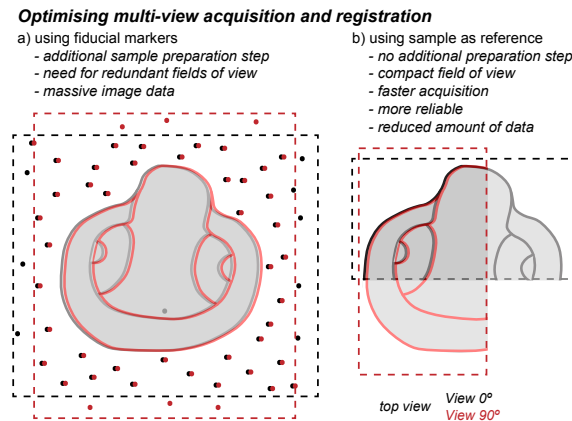


Figure 2.1 – Multi-view registration and fusion of light sheet microscopy data.

Multi-view light sheet microscopy is used to obtain a panoramic recording of the full zebrafish embryo. The sample is imaged at four orthogonal views, which are then registered to be combined (fused) into a single isotropic output stack. Typically, fiducial markers need to be acquired for guiding the image registration process which creates the need for acquiring large fields of view for ensuring sufficient fiducial overlap and correspondences. The presented method eliminates the need for fiducial markers by performing a robust registration directly on the sample data. This allows a tight adjustment of the fields of view to the sample, significantly reducing imaging time and data sizes (both by a factor of approx. 4).

To bring all views associated to a dataset into a common physical space, first a pairwise view registration is performed. Adapting to the chosen multi-view configurations, a set of registration pairs is manually defined to optimize the overlap between the stacks to be registered. The final transformation parameters are calcu-

2.1 Multi-view image reconstruction

lated by concatenating pairwise transformation parameters along the shortest paths between a given view and a global reference view. The transformation of a given pair of views is then modeled as an affine transformation:

$$x_b = Mx_a + \vec{c} \quad (2.1)$$

where x_a and x_b are corresponding physical coordinates of images A and B, $M \in \mathbb{R}^{3 \times 3}$ and $\vec{c} \in \mathbb{R}^3$. For obtaining M and \vec{c} , two consecutive registration steps (see Fig. 2.2) are performed. First, M is approximated by a rotation matrix given by the difference angle between the views as reported by the microscope metadata. Then, the translational shift \vec{c} is obtained as the maximal peak of the cross correlation calculated as:

$$\begin{pmatrix} c_x \\ c_y \\ c_z \end{pmatrix} = \underset{\vec{c}}{\operatorname{argmax}} \left\| \operatorname{FFT}^{-1} \left(\frac{\operatorname{FFT}(A) * \operatorname{FFT}(B)^*}{\|\operatorname{FFT}(A) * \operatorname{FFT}(B)^*\|} \right) \right\| \quad (2.2)$$

where FFT and FFT^{-1} denote the Discrete Fourier Transform and its inverse.

As a second step, the obtained parameters are used as initial values for a set of pairwise iterative content based image registrations. These optimizations use the normalized cross correlation as an image similarity metric (or objective function), and are performed with increasing degrees of freedom (using translation, rigid and affine transforms), working on successive pyramidal downsamplings of the image with the factors 8, 4, 2, 1, to typically arrive at a final spacing of 1 μm .

To place all views into the same reference coordinate system based on the pairwise registrations, the successions of transformations connecting one reference view with all others are concatenated. Finally, a last groupwise image registration step is

performed. This time, an objective function comparing all views simultaneously is minimized, given as the pixel variance along the first dimension of an $N + 1$ dimensional image stack composed by all N dimensional view images transformed into the reference view. The groupwise registration optimizes a transformation composed of one linear subtransformation for each view. Again, the optimization process is performed with increasing degrees of freedom: The linear subtransformations are first parametrized as a rigid, then as an affine transform and pyramidal downsamplings are used. Both optimization based registration steps were implemented using the open-source software toolkits , elastix [77], SimpleElastix [102] and SimpleITK [93]. Importantly, obtaining an initial translation from the cross correlation makes the content based registration significantly more robust compared to the case when another initialization method such as using the center of gravity is used (data not shown). This is most likely due to the strong effects of view dependent image deterioration on the iterative optimization schemes. Finally, the last group-wise registration step achieves a registration quality suitable for performing multi-view image deconvolution as described in the next section.

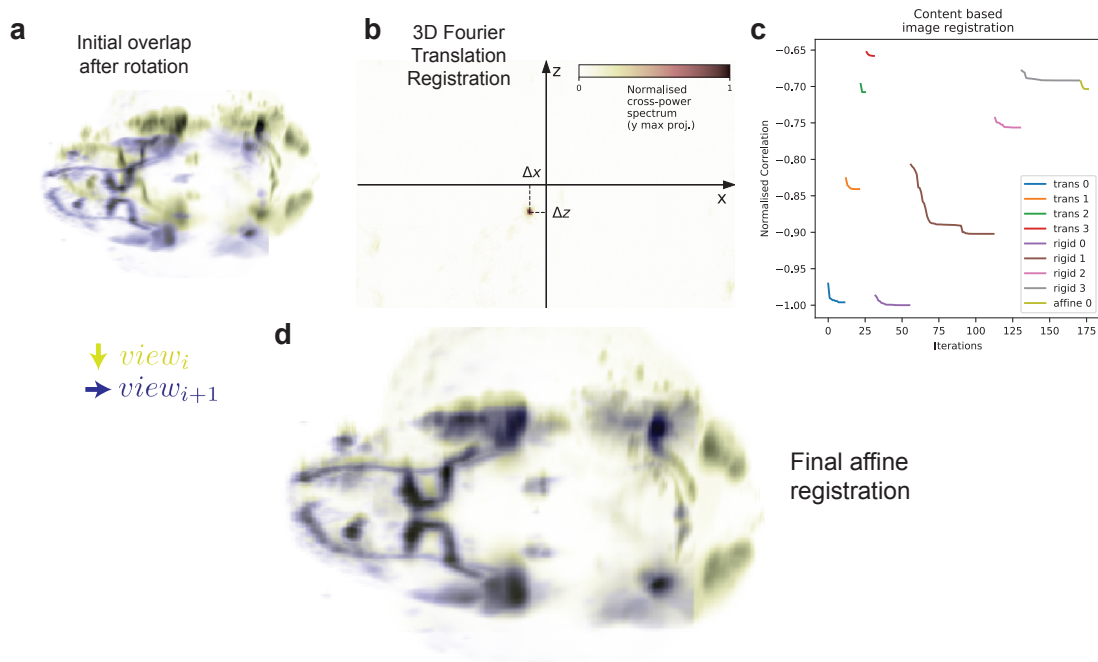


Figure 2.2 – Registration of a pair of views. a) Shows the initial overlap after a rotation transform based on the microscope metadata. b) The translational shift between the views is obtained as the maximal peak of the cross correlation between the images. c) As a second step, an iterative content based image registration is performed to obtain a final affine transformation.

2.1.2 Image quality weighted multi-view image reconstruction

Once the different views are registered they can be fused into a single high quality image stack. Ideally, the anisotropy of single views due to the typical z-extended point spread function can be compensated for by complementary views using multi-view deconvolution[80, 121]. However, in the case of the large zebrafish embryo, despite its optical transparency in the visible spectrum, image quality is deteriorated relatively quickly when moving away from the surface of the embryo. Fig. 2.3 and Fig. 2.4 illustrate this showing four orthogonal views of raw multi-view light sheet data. In principle, multi-view deconvolution could deal with PSFs that vary throughout the sample [148]. However, the variation of the PSF within the zebrafish embryo is very difficult to measure or model, and performing deconvolution with strongly errant PSFs increases the risks of introducing artifacts.

Addressing this problem, here a multi-view deconvolution approach dealing with sample scattering is presented. The approach consists of combining the Richardson-Lucy multi-view deconvolution (as put forward by [80]) with the use of image weighing based on local image quality. Specifically, the updating scheme of the iterative calculation of the final fused image was modified, which is typically given by:

$$U_v = \frac{I_v}{R_i \otimes P} \otimes P^* \quad (2.3)$$

$$R_{i+1} = R_i \cdot \sum_v \frac{1}{N_v} U_v \quad (2.4)$$

Here, P represents the psf, I_v the noisy image of a given view transformed into the target coordinate system and R_i the result image at iteration i . Notably, eq. 2.4 considers the update factors U_v of all views in equal parts, including those image

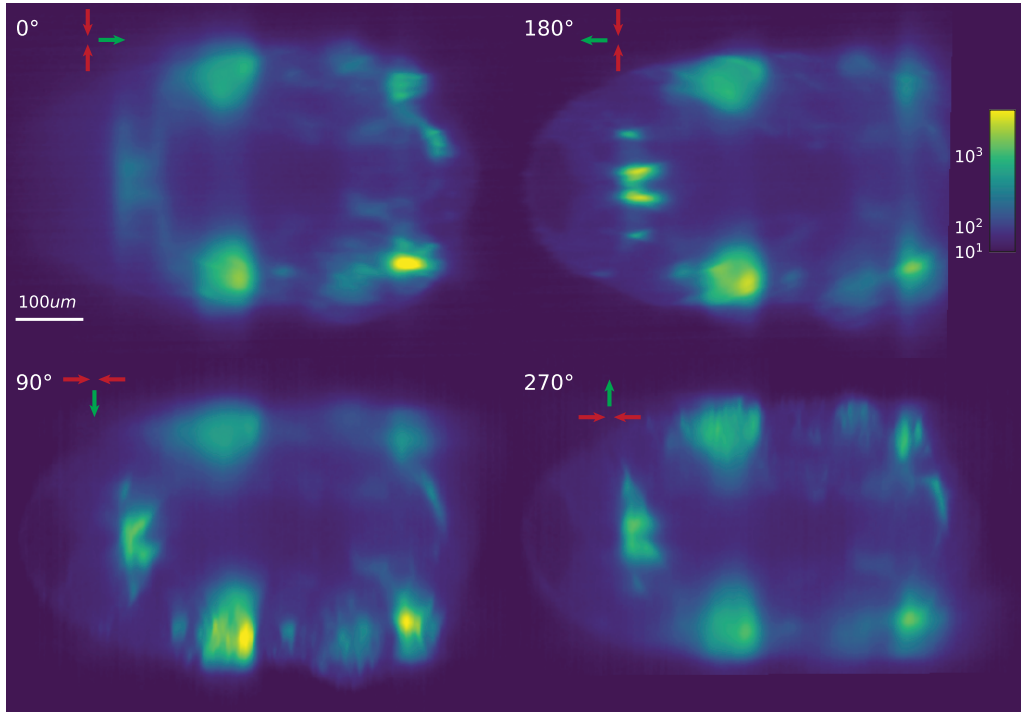


Figure 2.3 – Multi-view raw data from four orthogonal angles in a y-slice through the head of the zebrafish embryo. Image quality clearly deteriorates when moving deeper into the sample and the different views contain complementary information. Marker is the tandem fluorescent reporter displayed with a perceptually uniform LUT. Red and green arrows indicate illumination and detection directions respectively. Raw data was recorded with a spacing of $(\Delta x, \Delta y, \Delta z) = (0.65\mu m, 0.65\mu m, 3\mu m)$.

regions with very extended and unknown PSFs. To increase the contributions of high quality image regions and to reduce those of their low quality counterparts, a multiplication of the update fields U_v with local image quality based weights was introduced in this step. This leads to the following modification of eq. 2.4:

$$R_{i+1} = R_i \cdot \sum_v w_v \cdot U_v \quad (2.5)$$

where the weights are normalized ($\sum_v w_v = 1$). Accordingly, as an initial image the weighted average fusion of the input views $\sum_v w_v I_v$ was chosen. Multiple approaches

can be followed to derive suitable weights w_v , including geometrical considerations and content based image quality metrics. The Normalized Shannon Entropy [135] proved to represent a robust choice for multi-view light sheet acquisitions of the zebrafish embryo. It is calculated as:

$$DCT_{norm_{x,y,z}} = \left| \frac{DCT(I_{X,Y,Z})_{x,y,z}}{L_2(DCT(I_{X,Y,Z}))} \right| \quad (2.6)$$

$$m_{v,X,Y,Z} = - \sum_{\substack{x,y,z \\ DCT_{norm_{x,y,z}} > 0}} DCT_{norm_{x,y,z}} \log_2(DCT_{norm_{x,y,z}}) \quad (2.7)$$

Here, DCT represents the Discrete Cosine Transform and L_2 the euclidean norm. $w_{v,XYZ}$ indicates the calculation of the image quality metric on image blocks centered around the coordinates (X, Y, Z) . To determine a weight value for each pixel within the fused stack, the values obtained for each block are interpolated to the entire stack using nearest neighbor interpolation. To smoothen the transitions between pixels associated to different blocks, gaussian smoothing is applied to the image metric before normalisation:

$$m_v = m_{v,xyz} = SMOOTH(INTERP_{XYZ}(m_{v,XYZ})_{xyz}) \quad (2.8)$$

$$w_v = \frac{m_v}{\|\sum_v m_v\|} \quad (2.9)$$

As the calculation of the weights does not rely on any sample specific assumption, this approach should generalize well to other samples. Fig.2.5 illustrates the weight values as resulting for four orthogonal views of the zebrafish embryo. As expected and intended, the values approx. decrease with the sample depth and increase

2.1 Multi-view image reconstruction

towards regions associated to shorter optical paths of the illumination and detection through the sample. Also, the obtained values correlate with the visually perceived distribution of focus around the axis due to scattering.

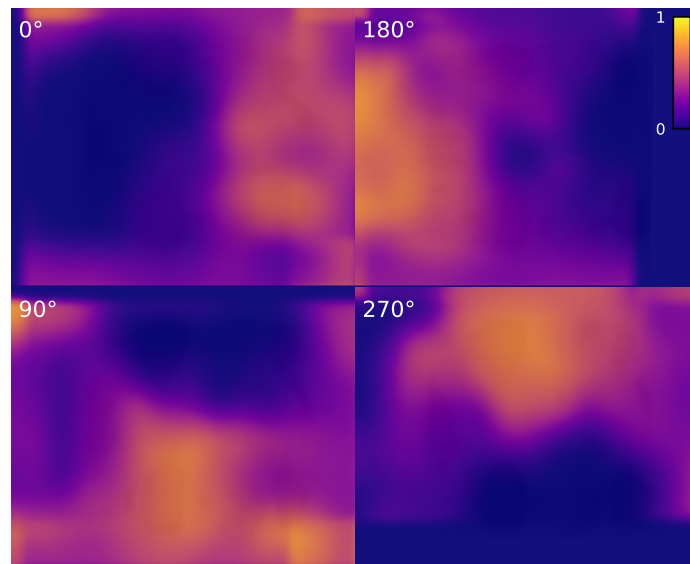


Figure 2.5 – Image quality weights obtained for the different views using the Normalized DCT Shannon Entropy: For a given view, high values (yellow) transitioning to low values (blue) reflect the visibly deteriorating image quality deep in the embryo.

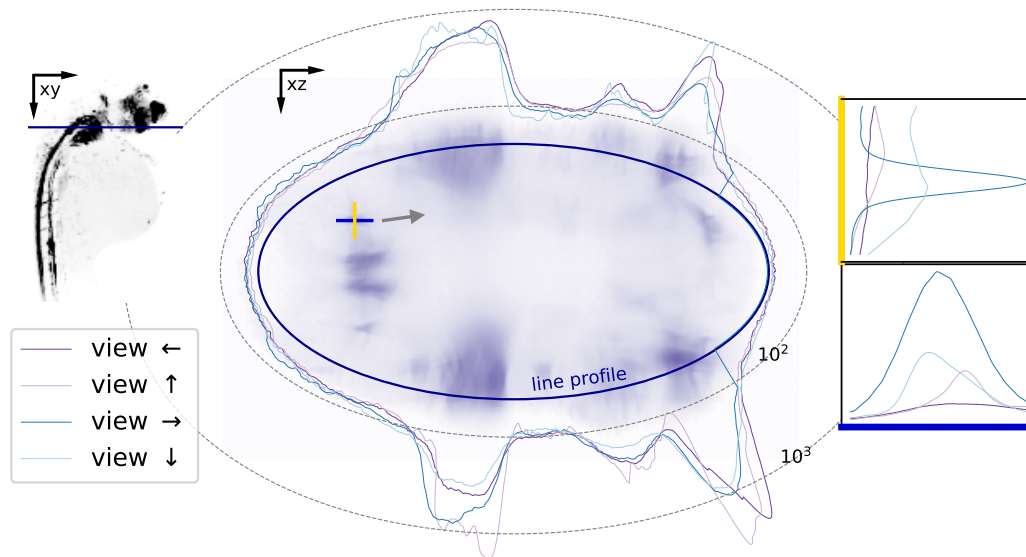


Figure 2.4 – Multi-view raw data from four orthogonal angles in a log intensity profile plot. Taking a xz cross section of the zebrafish embryo, the intensity profile along an (elliptic) line surrounding the embryo quantifies and illustrates the effect of light scattering on the images as recorded by the different views: When following the periphery of the sample, high intensities and high frequencies are shown by the corresponding views of most adequate detection direction. At the right, the signal along the blue and yellow crosshair is extracted (placed on top of the cross section of a nerve), illustrating complementary views in a scattering sample: Overall, the left view shows the highest intensities, followed by the top view as expected based on the location within the embryo. In the vertical plot, the left view shows the best signal to noise ratio (sharp peak), followed by the top view. In comparison, the horizontal plot shows a narrower peak of the left view, while along this direction the top and bottom views exhibit slightly sharper peaks.

2.1.3 Evaluation of improved multi-view fusion results

For a comparison and to get an overview over the achieved image quality in the multi-view fusion process, the presented modified multi-view deconvolution and other common fusion methods were applied to the zebrafish embryo data forming part of this study. Fig. 2.6 shows a xz cross section through the embryo and Fig. 2.7 a xy projection, both comparing the following fusion approaches:

- min and max intensity view fusions
- simple and DCT-weighted averaging of the raw views
- best view fusion (for every region, take the best view as determined by the DCT measure)
- DCT-weighted averaging of single-view deconvolutions
- multi-view deconvolution
- multi-view deconvolution with DCT weighted updating

From the figures it becomes clear that for our sample, the incorporation of the DCT-based image metric into the fusion process improves fusion quality. Additionally, the multi-view deconvolution approaches improve on the signal to noise exhibited by the averages and best view fusion, in particular yielding better results than the averaging of single-view deconvolutions. For further details see the figure captions.

To quantify the signal from the different fusion methods, Fig. 2.8 plots intensity values along a line surrounding the embryo and a crosshair on a sharply defined nerve structure. In the periphery of the embryo, the considered DCT-based methods succeed in resembling the signal provided by the local best view, which overall should exhibit the least pronounced scattering effects. When observing the nerve located slightly deeper within the embryo, it can be appreciated that the signal in axial direction is significantly improved by the weighted multi-view deconvolution compared to averaging or simple multi-view deconvolution (see figure caption).

This illustrates that in a highly scattering context, multi-view deconvolution in practice benefits from prior knowledge about the relative quality of the considered image views. Importantly, the resulting image intensity levels closely resemble those of the view with least PSF degradation, which is especially important when aiming for signal quantifications.

Within the scope of this study, typically four orthogonal views were imaged with a spacing of $(\Delta x, \Delta y, \Delta z) = (0.65\mu m, 0.65\mu m, 3\mu m)$ and data was fused into isotropic output stacks of spacing $\Delta xyz = 1\mu m$. For the DCT-based multi-view deconvolution the effect of the PSF was approximated by a gaussian filter with sigmas $(\Delta s_x, \Delta s_y, \Delta s_z) = (0.5\mu m, 0.5\mu m, 4\mu m)$ and the iterations were stopped either when the relative intensity change between consecutive images resulted below $1e^{-5}$ or the maximum of $N_{max} = 20$ iterations was reached. In terms of computational efficiency, the computation of each output stack required approx. 15 min on a machine with 24 cores.

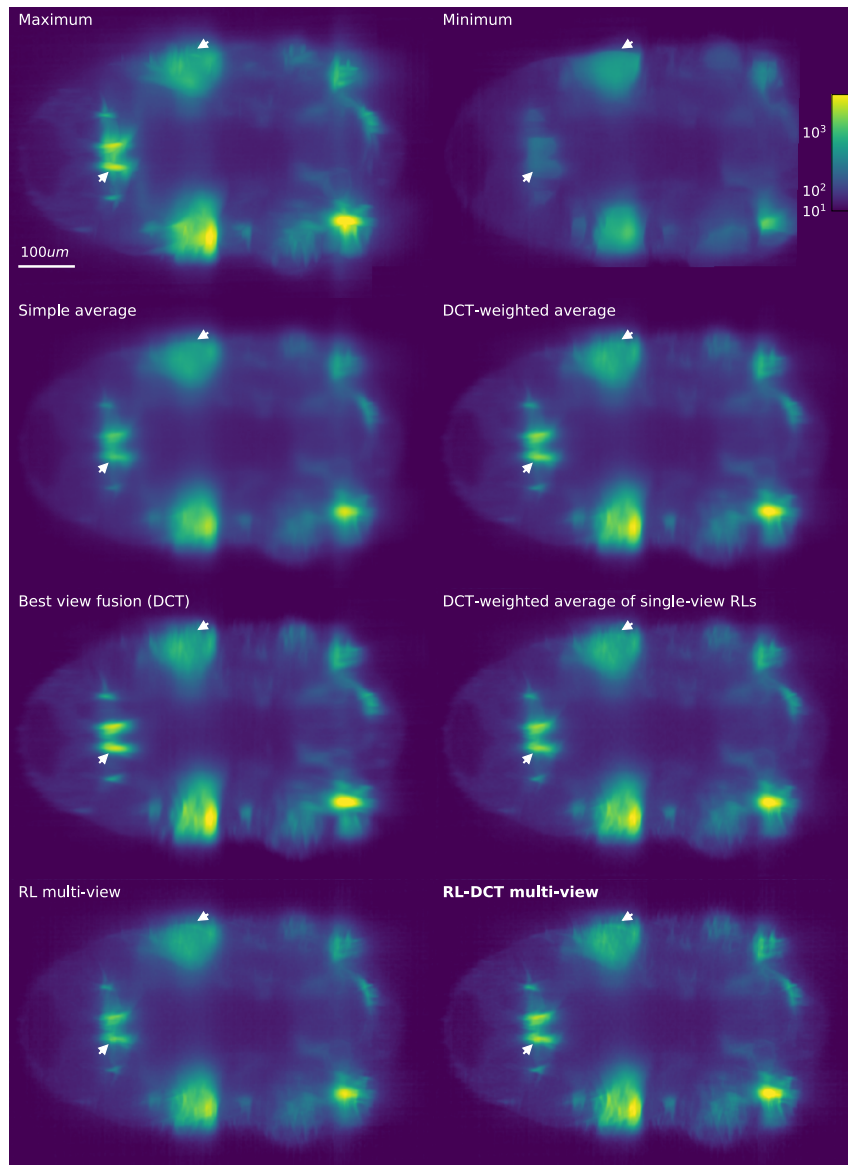


Figure 2.6 – Comparison of multi-view fusion methods (XZ section)

After registration, the multiple views can be fused using different methods. Here a range of such methods is compared, including pixel-wise maximum and minimum, simple and weighted averaging, single view RL deconvolution before averaging and multi-view deconvolution. Finally, these established approaches are compared to the presented method extending the update step of RL multi-view deconvolution: By introducing a view and sample location specific image quality dependent weighting factor, the effective deconvolution concentrates on information from high quality views exhibiting little psf degradation. Visually, this content aware deconvolution improves the image quality of the fusion output in case of the highly scattering early zebrafish embryo (see the resolution of the two nerve structures or the boundary definition of the branchial arches as indicated by the white arrows). More specifically, structures are less stretched in radial direction (into the sample) while at the same time preserving the contrast of the corresponding best view. ⁴¹

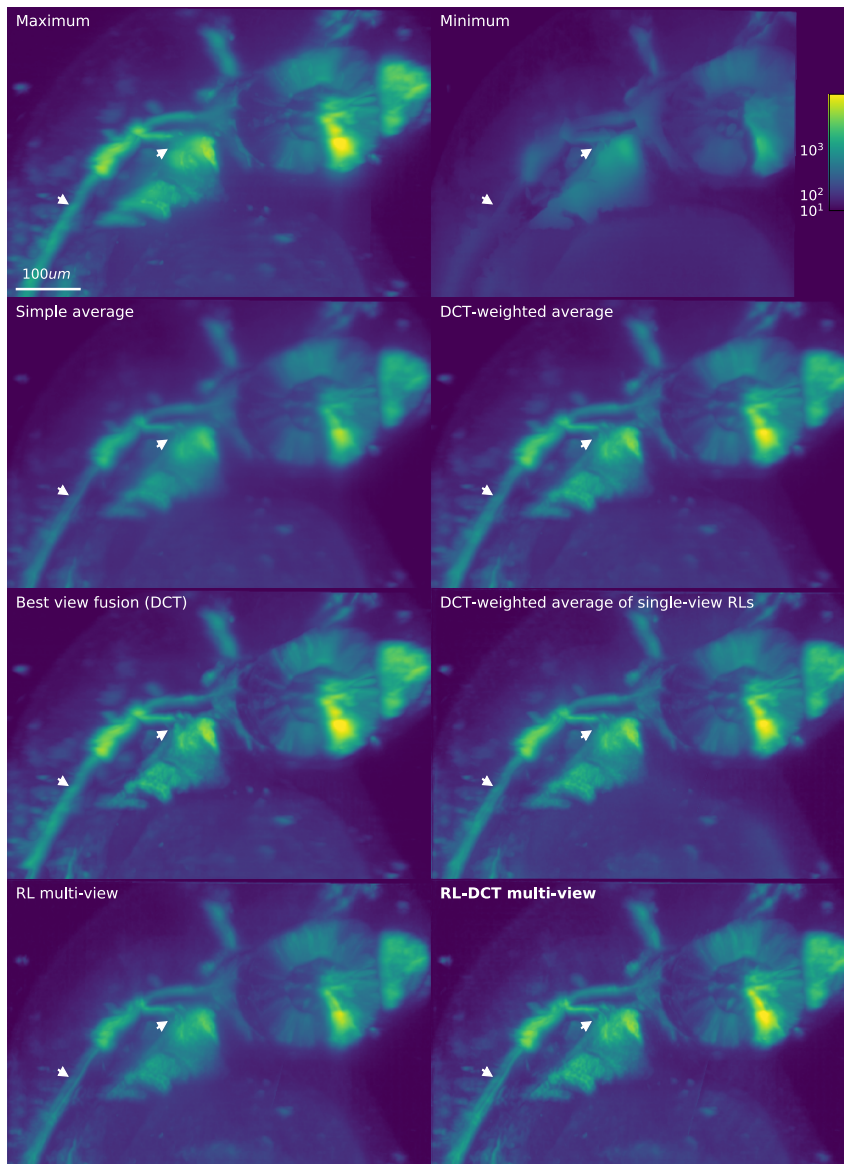


Figure 2.7 – Comparison of multi-view fusion methods (z - max. projection)

To observe the effect of the different fusion methods on the lateral resolution of the embryo, this figure shows a z projection of half of the bilateral embryo. Much of the blur present in the max, min and averages is improved upon in the (locally) best view and deconvolution fusions. The visually best contrast is achieved by the presented RL-DCT multi-view deconvolution, which additionally shows signal intensities very close to the best view fusion (see for example the diagonally running dorsal nerves or the branchial arches as indicated by the white arrows).

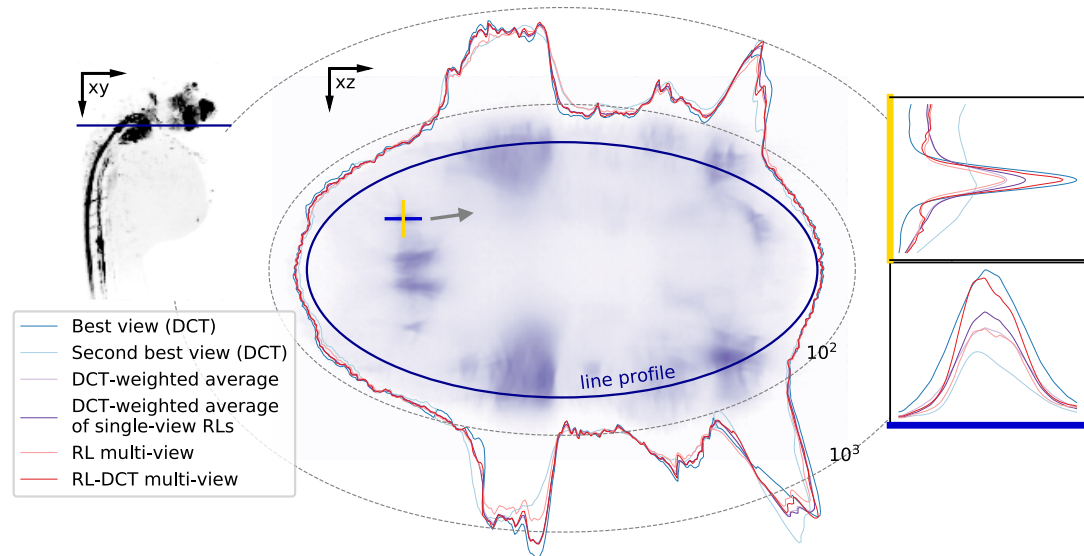


Figure 2.8 – Comparison of multi-view fusion methods (log intensity profile plot)
 On the same line profile as in Fig. 2.4 the intensities obtained from a subset of the most important fusion methods are compared. Around the embryo, the signal intensity of all methods is enclosed between the best and second best view intensities (as determined by the DCT quality measure). Along the embryo periphery, due to little scattering effects the image quality of the raw views is high. Therefore, in contrast to simple multi-view deconvolution, all DCT based methods perform well in capturing high and low signals. The blue and yellow crosshair measures intensities deeper within the embryo. Here, RL-DCT exhibits the best signal to noise ratio in the lateral and axial directions.

2.1.4 A tool for multi-view deconvolution of very large datasets

While being fundamental for producing the atlas framework (sec. 2.2) and to study chemokine signaling in toto (sec. 3), the above described framework for multi-view deconvolution is of general applicability to multi-view light sheet microscopy datasets. Especially its

- robust automated view registration independent of fiducial markers and
- image quality weighted multi-view deconvolution scheme

improve on features of existing frameworks, making it a potentially valuable resource for use in combination with a variety of multi-view imaging purposes and configurations.

In order to support the processing

- of very large datasets
- on both laptops and computational cluster environments
- on any operating system

we implemented the multi-view fusion framework using platform independent open source software building upon and contributing to the growing scientific python community [157][64][158], including *elastix* for content-based image registration [77][103] and *(Simple-)ITK* for efficient image manipulations [168][93]. For working on almost arbitrarily sized images, we implemented the multi-view fusion to produce the final reconstructed image in a block-wise manner with the purpose of both parallelizing processing and reducing the memory requirements. This functionality has been implemented using *dask* [130][33], which additionally allows the entire workflow to be executed on either laptops or large HPC clusters with minimal configuration. The resulting software package is available [here](#)¹. Finally, fig. 2.10 and 2.9 illustrate the results of applying the image quality weighted multi-view reconstruction to two further datasets acquired with a Z1 microscope.

¹For print: <https://github.com/m-albert/MVRegFus>

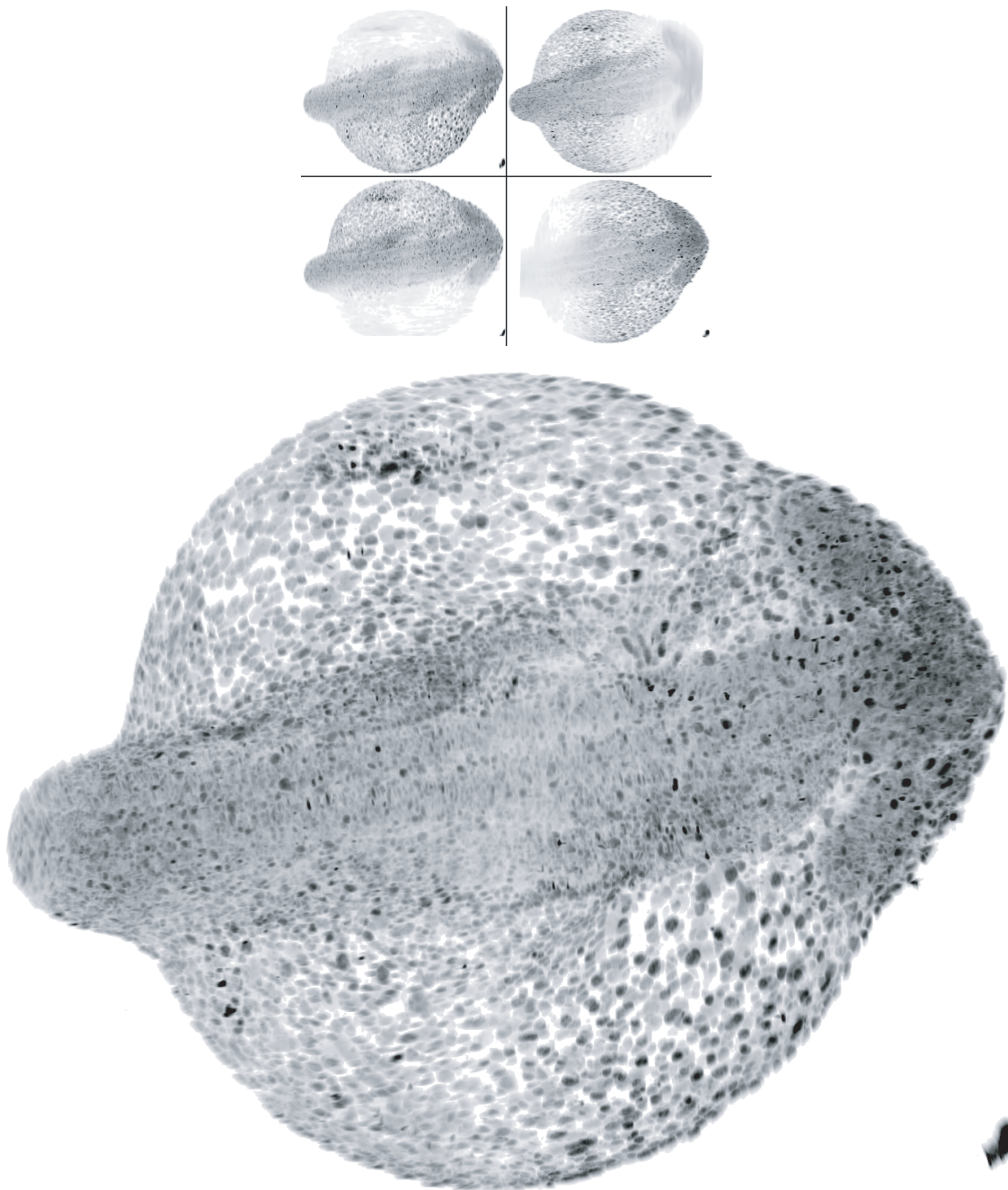


Figure 2.9 – An example of a strongly scattering dataset: *in toto* zebrafish embryo at 15hpf expressing a nuclear marker.

A total of 8 views (shown are stacks with left and right illuminations fused) acquired at 90° , were reconstructed into an output of isotropic spacing $\Delta = 0.5\mu m$. The fusion is shown as a projection along the rotation axis to illustrate the benefit of multi-view reconstruction. Raw data was acquired and kindly provided by Max Brambach.

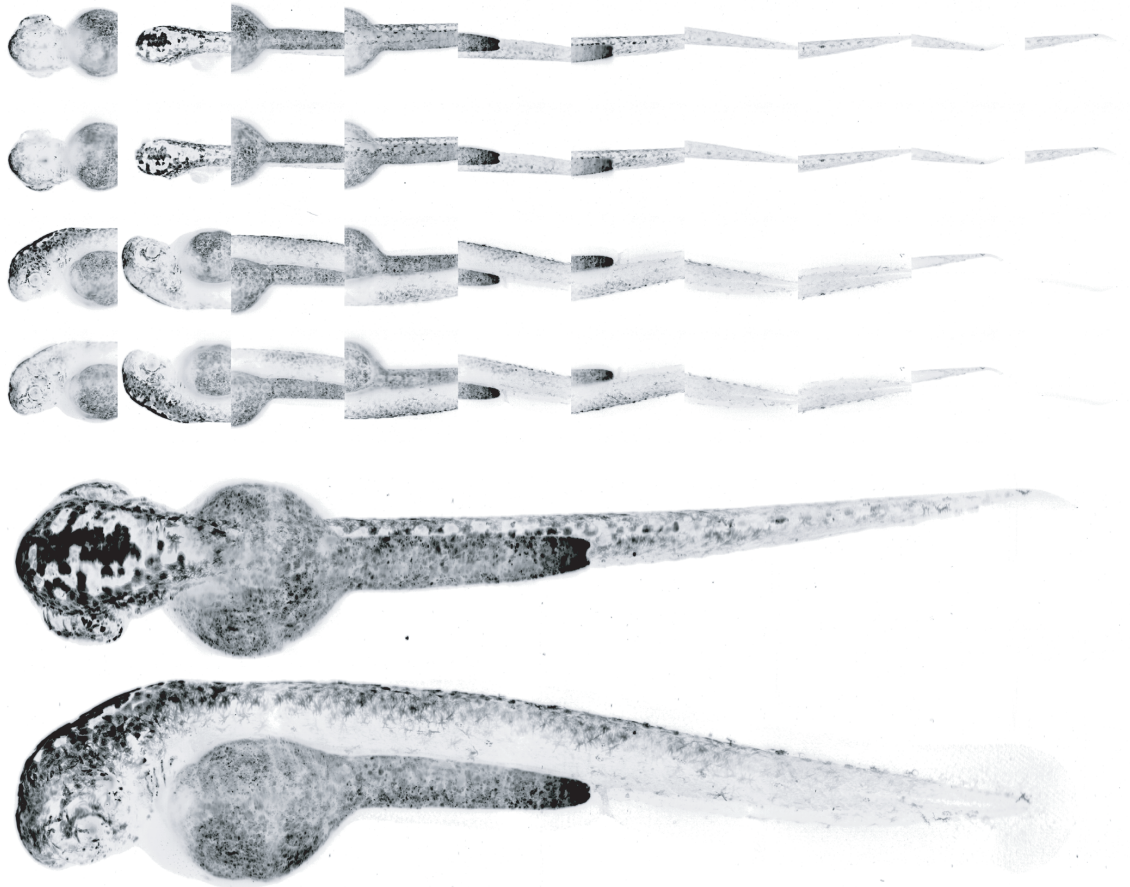


Figure 2.10 – An example of a large dataset: *in toto* zebrafish embryo at 5dpf.

A total of 40 views (top) including left and right illuminations of different positions at 90° angular steps along the AP axis (individual stack size $300 - 600 \times 1912 \times 1912$) were reconstructed into an output of isotropic spacing $\Delta = 0.5\mu m$ and size $1500 \times 7500 \times 1300$ (bottom, x and z projections). Raw data was acquired and kindly provided by Max Brambach.

2.2 Atlas framework

2.2.1 Spatial normalization of embryo stacks

2.2.1.1 Pairwise nonlinear image registration

At the basis of establishing a common coordinate system for comparing different embryos lies the image registration of a given sample onto another. This inter-sample registration, as opposed to the previously described registrations, needs to account for additional sources of variability. While for multi-view registration a linear transformation of the coordinates would map one view onto another, nonlinear transformations are required for normalising different samples and account for inherent biological variability, labelling differences and the phenotypic effect of genetic perturbations.

To this aim a two step process was applied consisting of an initial affine transformation and a subsequent diffeomorphic mapping. In order to specifically account for image intensity biases due to differences in labelling, prior to registration the images were normalized using Contrast Limited Adaptive Histogram Equalization (CLAHE)[158]. An example of applying this normalisation to a *Cxcr4b::GFP* image is shown in Fig. 2.11a. Existing 2D implementations of CLAHE were adapted to 3D², which significantly improved the robustness of the initial affine registration, for which the same procedure as in the case of the multiple view registration was used (see section 2.1.1). Fig. 2.11b shows the registration outcome for the first step, which roughly aligns the embryos. One source of large-scale variability that the linear transformation cannot account for is given by the varying degrees of “head straightening” embryos exhibit during this phase of development despite careful staging.

²An existing 2D implementation of CLAHE was extended to arbitrary dimensions and made available to the research community via the python image processing module *scikit-image* (<https://github.com/scikit-image/scikit-image/pull/2761>)

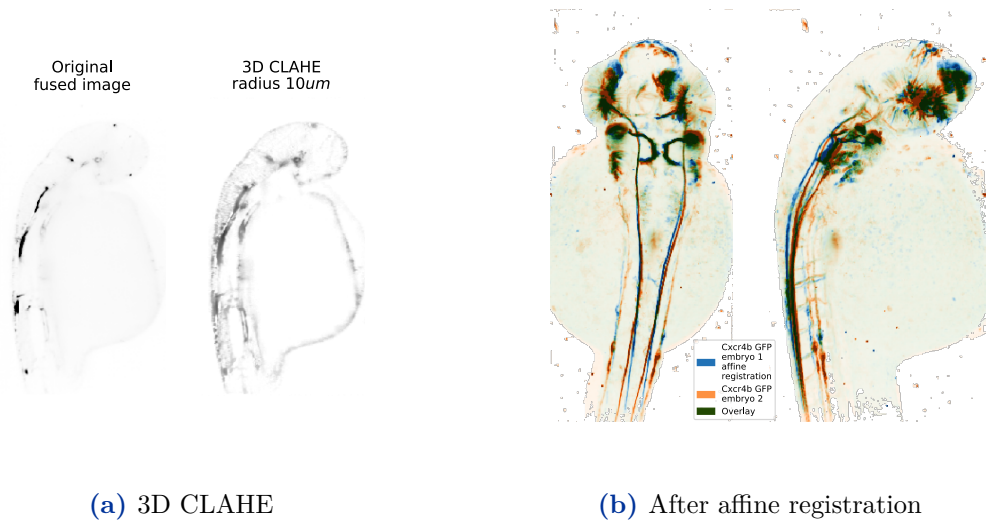


Figure 2.11 – Image normalisation using CLAHE significantly improves the robustness of linear registration, which roughly aligns the tissues and serves as the starting point for nonlinear registration

For the second nonlinear registration step the symmetric diffeomorphic normalisation toolbox *SyN* [4] was used, a framework that is widely utilized for image alignment in the context of MRI studies [76]. Its implicit regularization strategy of obtaining deformation fields composed by the integration of smooth velocity fields leads to both accurate and biologically plausible transformations. Another important criteria for choosing this method was the fact that its resulting deformations are guaranteed to be invertible, which is important for establishing bijective transformations between samples for its use within the groupwise registration approach described below (section 2.2.1.2). The performance of the registration method was optimized for our samples by adapting it in two ways. First, the dependence of the regularizing smoothing kernel on the resolution level to high initial and low final values was optimized, being applied on many resolution levels. Secondly, for the initial coarse resolution levels, 3D CLAHE processed images of varying radii were

used instead of the raw fused images, while the latter was used for the subsequent fine registration.

Due to the fact that nonlinear registration is computationally expensive, stacks downsampled to an isotropic voxel spacing of $s_{x,y,z} = 3\mu m$, were used, retaining approx. cellular resolution. For all registrations the expression of Cxcr4b in the GFP and optionally the RFP channel was used as a common reference label. In addition to Cxcr4b expression, autofluorescence present in regions such as the yolk provided additional references to guide the registration process. Favourably, the use of panoramic multi-view images constrains the registration process in regions of degrading image quality deep inside the sample, as these regions are fully surrounded by high image quality regions closer to the embryo surface.

Finally, a given pair of images was registered using four registration runs with the optimized parameters summarized in Table 2.1. The output of a given run consists of a deformation field which maps the so-called 'moving' image stack onto the 'fixed' image stack. Specifically, it consists of a vector field, or deformation field, $D_{fm} : \mathbb{R}^3 \rightarrow \mathbb{R}^3$, which relates the coordinates in the fixed image $x_f \in \mathbb{R}^3$ to those in the moving image $x_m \in \mathbb{R}^3$:

$$x_m = x_f + D_{fm}(x_f) \tag{2.10}$$

The affine registration is considered as an initial coordinate transformation for the first diffeomorphic registration run and its parameters $M_0 \in \mathbb{R}^{3 \times 3}$, $c_0 \in \mathbb{R}^3$ are subsequently composed with the obtained deformation field D_{fm}^0 , yielding a D_{fm} containing both the linear and non-linear transformations:

$$D_{fm}(x_f) = D_{fm}^0(M_0 x_f + c_0) \tag{2.11}$$

Similarly, after a given run the obtained deformation field is composed with the field from the previous run, transforming the moving image as the input for the subsequent run if applicable. The reason for dividing the registration into several runs was that available frameworks allowed only one setting for the update field smoothing kernel for a given registration process (this also applies to github.com/nipy/dipy used here and the original SyN software registration collection under github.com/ANTsX/ANTs). In principle, a single registration would be better as it avoids the interpolations during the intermediate transformations.

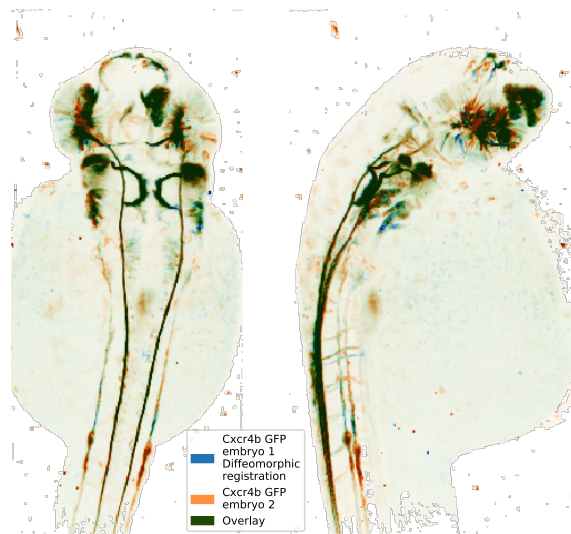
Run	1	2	3	4
Scaling factor s	1.2^i	1.5^i	1	1
Image smoothing kernel σ_i (um)	$1.5 * (s_{1_i} - 1)$			
Update field smoothing kernel σ_D (um)	$12 * s$	$6 * s$	3	1.5
CLAHE kernel size c_i (um)	$\begin{cases} 20 & i \geq 9 \\ 10 & i < 9 \end{cases}$	0	0	0
Iterations i	$\{0, \dots, 17\}$	$\{0, 1, 2, 3\}$	$\{0\}$	$\{0\}$

Table 2.1 – SyN diffeomorphic image registration parameters. Cross correlation was used as the image similarity metric. For all runs the convergence criteria consisted of the tolerance $c = 10^{-7}$ and a maximum iteration number of $N_{max} = 1000$. The registration was performed using the SyN implementation of the *dipy* framework. The careful adaptation of parameters to the Cxcr4b labelled zebrafish embryo were crucial for obtaining high quality registration results.

Fig. 2.12a shows the results of diffeomorphic registration for two wild type embryos. The superposition of structures is significantly improved compared to the result after linear registration. Qualitatively, tissues overlap well and most sample variation is eliminated. This also holds true for the registration between a wild type embryo and a Cxcr7b^{-/-} mutant shown in Fig. 2.12b. In this case, the above introduced modifications and adaptations of the SyN registration method proved especially useful. The local contrast enhancement preprocessing step significantly improved registrations in which the image contrast strongly differed between samples. This was the case for the cxcr4b:GFP labelled arrested primordium in cxcr7b^{-/-} mutants, which

gives rise to an extended intensity gradient due to scattering effects, misleading the unmodified registration process in the neighborhood of the organ. Local contrast enhancement could also improve registration performance near fluorescent beads and imaging artefacts close to the sample surface, and non ubiquitous fluorescent labelling in general.

One clear limitation of the above described registration approach is reached when samples are tried to be normalized which exhibit too strongly differing tissues. This can be the case when a sample region does not contain the same tissues or, generally speaking, when the tissue contexts to be compared arose from developmental trajectories which cannot be approximated by a static deformation field. An example for this is the region where the arrested and elongated lateral line primordium in the mutant occupies the space held by the chain cells and deposited sensory organs in the wild type. This represents a large morphological variation which cannot be accounted for by the registration. Still, due to local contrast filtering, the close neighbourhood of this unilaterally appearing tissue appear faithfully overlapped, while at the same time the resulting transformations contain clear evidence for a phenotypic variation that can be quantitatively captured using the method described in section 2.2.4.



(a) Two wild type embryos

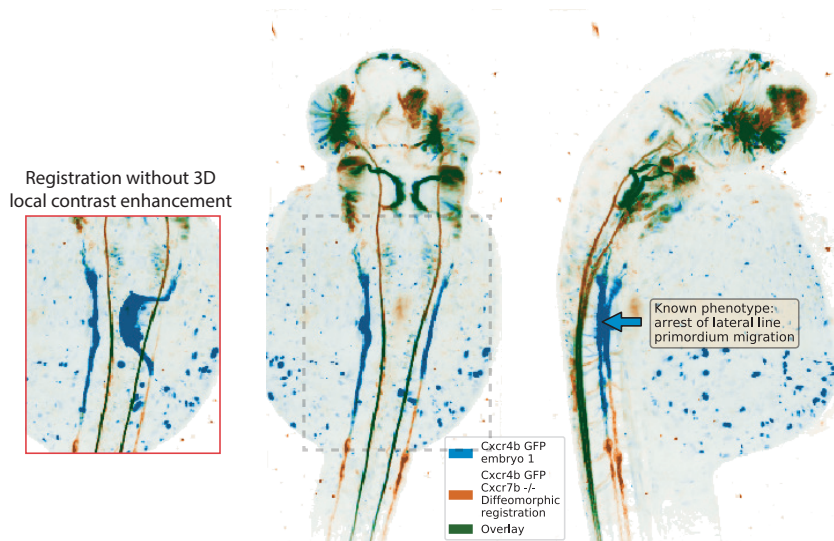
(b) Wild type and *Cxcr7b*^{-/-}

Figure 2.12 – Representative registration result after pairwise diffeomorphic registration. The overlay shows a highly accurate superposition of tissues for registrations between two wild type samples (a). This also holds true for mapping wild type onto mutant samples (b) when applying local contrast enhancement prior to registration. Without contrast enhancement, strong artefacts appear in the neighbourhood of the lateral line primordium.

2.2.1.2 Establishing a common reference coordinate system

Thus we established robust pairwise image registration that serves as the basis for placing multiple samples into the same common coordinate system (CCS). Existing atlases that focus on the zebrafish brain achieve this by mapping new samples onto a given template [131, 126, 84]. This template sample is usually chosen to be either a single representative sample or an averaged sample calculated from a subset of available samples. In the first case, the common space is biased by the particular choice of the template sample and in the second case, relying on a registration between a sample and a sample average is problematic, as misregistrations during template creation will influence the registration quality of newly incorporated samples.

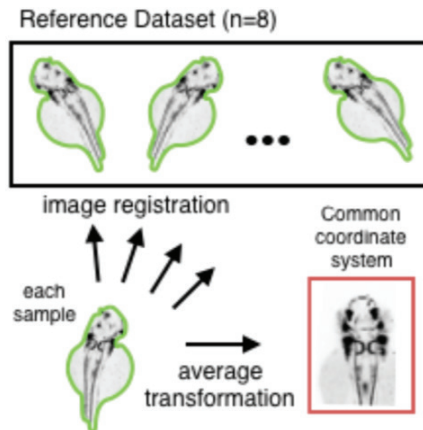


Figure 2.13 – Each new sample was placed into the common coordinate system by registering it to each sample of the reference dataset consisting of $N = 10$ wild type samples. The inverse of the average deformation field of these pairwise registrations then transformed the sample into the CCS.

To address both of these problems, the following groupwise registration strategy for defining a CCS was chosen. A reference subset $\{I_i^R\}$ of $N = 10$ wild type samples is defined as the reference dataset. For incorporating a new sample I , I was registered against each I_i^R , resulting in the deformation maps D_{I,I_i^R} (see Fig. 2.13 for a schematic). In the case of a sample in the reference dataset, the deformation mapping it to itself was set to unity (zero displacement vector field). Then the

average of $\{D_{I,I_i^R}\}$ was calculated and inverted to result in the transformation D_I , transforming I into the CCS:

$$D_I(x) = \left(\sum_i D_{I,I_i^R}(x) \right)^{-1} \quad (2.12)$$

This groupwise registration scheme can be iterated to further improve registration quality. To do so, a new CCS was defined by applying the same procedure to the samples transformed into the CCS of the previous iteration. For avoiding multiple interpolations, the resulting deformation maps were composed and only then used to transform the input sample data. To limit computational resources, two iterations were chosen for this application, exhibiting a good convergence behavior.

To align the principal axes of the CCS to those of the sample, an orientation transform was incorporated into the deformation maps of the first iteration. For this, the plane defining the bilateral symmetry of the zebrafish embryo was found by registering the mean of the reference samples in the CCS against its laterally inverted image. Tissue coordinates were extracted performing a basic tissue segmentation using Otsu thresholding. The correspondence between bilaterally symmetrical coordinates obtained from the registration then defined the embryo midplane, to which a linear plane was fitted. Finally, a basis change was performed choosing the normal vector of the fitted plane as the new x-axis. The new y-axis was chosen to align with the first axis of a Principal Component Analysis of the segmented tissue coordinates, representing the Anterior-Posterior axis of the embryo. The new z-axis then resulted as the cross product of the x and y-axes, defining the dorso-ventral axis of the CCS.

Importantly, by registering each sample to a set of reference samples a bias towards a single sample is avoided and potential pairwise misregistrations are averaged out. Another advantage of this approach is its linear scalability, since new samples can be readily incorporated into an existing CCS if the reference dataset is kept constant.

2.2 Atlas framework

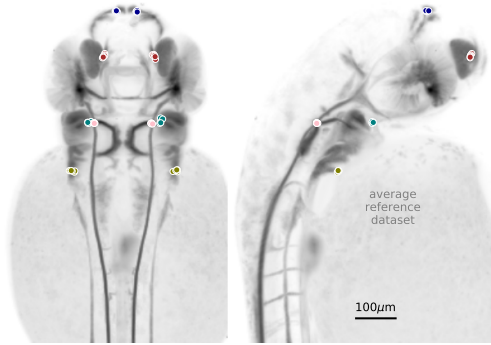
Name	Description	Max dist. (μm)	Mean dist. (μm)
AN_L	Left anterior habenular nerve	4.25	2.74
AN_R	Right anterior habenular nerve	2.37	1.72
OB_L	Left olfactory bulb nerve base	6.72	3.86
OB_R	Right olfactory bulb nerve base	9.31	4.45
VB_L	Central blood vessel bifurcation right	5.25	3.54
VB_R	Central blood vessel bifurcation left	7.38	6.09
NC_L	Left lateral and facial motor nerve crossing	2.53	1.44
NC_R	Right lateral and facial motor nerve crossing	3.07	2.31
BA_L	Posterior branchial arch extension left	6.96	4.65
BA_R	Posterior branchial arch extension right	8.33	4.06

Table 2.2 – List of landmark definitions used for registration validation (see Fig. 2.14. Landmarks were chosen to represent morphologically distinct features present in all considered samples including wild type and *Cxcr7b*^{-/-} genotypes.

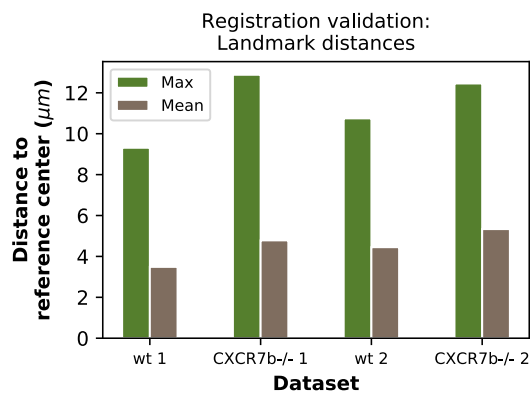
Fig. 2.14a shows the average intensities of the transformed reference samples in the final CCS. As can be observed, tissues appear well defined due to good sample overlap, the average reference embryo being almost indistinguishable from a single sample stack. In order to quantitatively determine the achieved registration quality of the presented registration framework, the distances between manually defined landmarks were measured. These were annotated for two wild type and two *Cxcr7b*^{-/-} mutant sets of six embryos each, recorded on different experimental days, including samples of the reference dataset. The landmarks were positioned at ten morphologically distinct locations within the embryo, which are summarized in Table 2.2.

The landmark coordinates were then transformed into the CCS using the corresponding deformation maps of each sample. The distances were measured between a given landmark and the geometrical center of landmarks belonging to the reference samples. Fig. 2.14b shows the maximum and mean distances for the different experimental days and genotypes, which were found to vary between $9\mu m < d_{max} < 13\mu m$ and $3\mu m < d_{mean} < 5\mu m$ respectively. On the datasets used for validation, the vari-

ability in registration precision of the experimental replicates was comparable to those of a different genetic condition. Finally, considering an average cell diameter of roughly $d \approx 10\mu m$, these values indicate that the registration framework achieves approx. cellular resolution for the vertebrate zebrafish embryo.



(a) Landmarks placed on the averaged reference dataset



(b) Landmark distances for different datasets

Figure 2.14 – Registration validation using landmark annotations reveals that the achieved resolution is within the spatial range of an average cell. Landmarks were chosen to represent morphologically distinct points in the sample. The distances are measured for the samples of the reference dataset and indicated with respect to the geometric center of all instances of a given landmark. Final landmark distances with maximal values of approx. $d_{max} \approx 13\mu m$ and mean values of less than $\langle d \rangle = 5\mu m$ indicate cellular resolution under the assumption of a typical cell diameter of $d = 10\mu m$.

2.2.2 Definition of tissue patches using segmentation and clustering

After placing samples into the common reference system, the analysis was focussed on the tissues of interest by performing a segmentation of the Cxcr4b expressing cells. Besides being the biological focus of the study, this is necessary as the above described registration accuracy does not strictly hold for parts of the embryo which do not express the reference marker or significant autofluorescence signal. For obtaining a tissue segmentation, both the GFP and RFP channels of all embryos contained in the reference dataset I_i^c were used. For each channel the average $\bar{I}^c = \frac{1}{N} \sum I_i^c$ was calculated and an intensity threshold T was obtained by applying an Otsu threshold in two iterations:

$$T_0^c = \text{Otsu}(\{I^c(x, y, z)\})$$

$$T^c = \text{Otsu}(\{I^c(x, y, z) | I^c(x, y, z) < T_0^c\})$$

To further refine the segmentation, an *Ilastik* ([145]) classifier was manually trained on two samples using the GFP channel and applied to the full reference dataset obtaining the segmentations s_i . The tissue segmentation S was then obtained as:

$$S = \{(x, y, z) \mid \min_i I_i^{GFP}(x, y, z) > T^{GFP}\}$$

$$\cap \{(x, y, z) \mid \min_i I_i^{RFP}(x, y, z) > T^{RFP}\}$$

$$\cap \{(x, y, z) \mid \min_i s_i(x, y, z) > 0\}$$

$$\cup \{(x, y, z) \mid I^{GFP}(x, y, z) > \frac{T_0^{GFP}}{2}\}$$

$$\cup \{(x, y, z) \mid I^{RFP}(x, y, z) > \frac{T_0^{RFP}}{2}\}$$

Here, \cap and \cup represent the intersection and union and are applied sequentially starting from the first thresholded set. To remove single pixels and small disconnected structures, the segmentation mask was morphologically eroded and subsequently dilated, both in a single iteration. Finally, a size filter was applied to exclude segmented objects occupying a volume smaller than $1000\mu\text{m}^3$ (equivalent approx. to the volume of a single cell). Fig. 2.15 a) shows a rendering of the segmentation overlaid onto the average reference embryo.

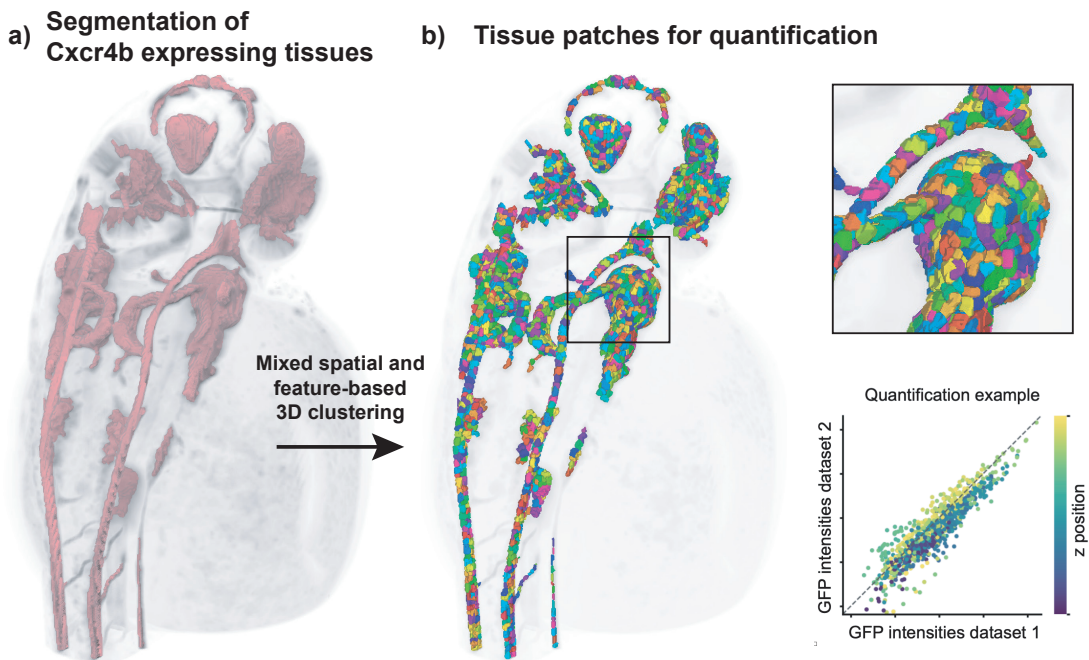


Figure 2.15 – Tissue segmentation and clustering: To focus the analysis on tissues expressing Cxcr4b, the relevant tissues are segmented in 3D (a). The segmentation is then further clustered into tissue patches (b), which align with the intensity patterns of the expressing tissues and where chosen to have an average diameter of $d = 10\mu\text{m}$ approx. equivalent to the registration accuracy. The tissue patches are then the units from which image features are extracted and compared between samples.

The main aim behind placing many samples into the same coordinate system consisted in directly comparing image features between the samples. Using the same resolution as for the nonlinear image registration of $3\mu\text{m}$, the segmented volume

occupies approx. 90000 pixels, each representing a location from which image features such as fluorescence intensities can be extracted. To significantly reduce this number, the segmented volume was subdivided into larger comparison regions, accounting for residual registration inaccuracies and easing data handling.

Subdivision was performed using hierarchical agglomerative clustering of the segmented voxels, i.e. by recursively merging pairs of clusters based on a distance criterion. The final amount of clusters $N_{clus} = \frac{V_s}{d^3} \approx 3000$ was chosen such that the obtained regions would average a diameter of $d = 10\mu m$ (i.e. a volume of $1000\mu m^3$), which is again equivalent to a cell's dimension and the length scale of registration accuracy. First, each pixel within the segmented volume was assigned a feature vector which consisted of its three spatial coordinates and the mean intensity of the CLAHE filtered reference samples in the common coordinate system:

$$f(x, y, z) = \begin{pmatrix} x \\ y \\ z \\ \frac{1}{N} \sum_i CLAHE(I_i^c(x, y, z)) \end{pmatrix}$$

Further, the last dimension of the feature vector was weighted by a factor determined as twice the distance between maximally distant voxels within a cube of edge length $d = 10\mu m$, giving the contrast based feature component roughly the same variance as the spatial coordinate components. As a distance criterion Ward's method was chosen, which considers the error sum of squares of all voxels contained in a given pair of clusters. The connectivity of the pixels was calculated solely based on the spatial coordinates, constraining which voxels were available for merging and thereby creating only spatially connected clusters.

The dimensionality reduction consisting of dividing the segmented volume into tissue patches therefore accounts for residual misalignment in the reference coordinate

system and at the same time eases data handling when comparing image features between samples. A rendering of the tissue patches is shown in Fig. 2.15 b), illustrating a homogeneous distribution of roughly equally sized clusters. To use the tissue patches for quantifications, the mean pixel intensity of a given image feature such as GFP or RFP intensity, lifetime ratio or volume change (as described in the next section) can be extracted for every patch and embryo. These observables can then be compared to each other, such as exemplified in a scatter plot showing the GFP intensities of two wild type embryos in Fig. 2.15 b).

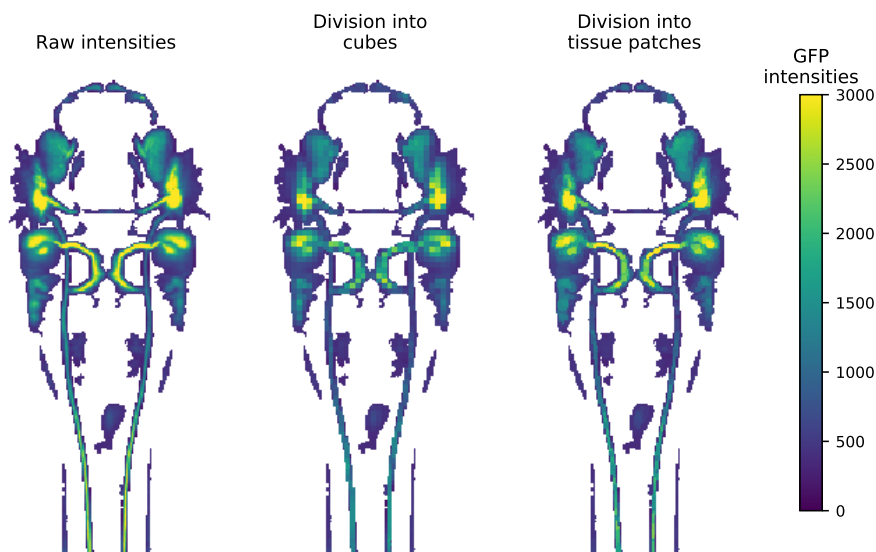


Figure 2.16 – The effect of mixed spatial and contrast based clustering. The left image shows the mean maximum z-projected GFP intensities of the reference dataset within the segmented volume. The other two images result from replacing single pixel intensities by the mean intensities using two different methods for subdivision, simple cubic pixel pooling and the presented clustering approach. Due to clustering operating both on coordinates and contrast, the latter conserves many more structures compared to the first.

Importantly, having included an image contrast based feature into the feature vector has the effect that cluster borders align with transitions between tissues of differing relative *Cxcr4b* expression, preserving relevant image detail. This effect is illustrated in Fig. 2.16, which compares the raw image intensities with images reconstructed

from patches obtained using two different methods, simple binning and the presented clustering (see the figure caption).

2.2.3 Experimental setup and statistical analysis

In addition to the technical considerations, an important biological challenge that arises when studying the full sample in an unbiased way is consistent staging. During the pharyngula period, the migration progression of the lateral line primordium is the standard reference marker for staging [75]. However, primordium migration is impaired in *cxcr7b*^{-/-} mutants and could therefore not be used here directly. Instead, samples of any of the genetic conditions of interest were paired with a wild type control group and raised side-by-side in equal conditions until reaching 36hpf as determined in the wild type. As image acquisition was performed on live samples, these continued to age during a given experiment. Therefore the total amount of samples imaged during a given experimental session was limited to approx. $N = 20$, amounting to an absolute age divergence of maximally 3-4h (equivalent to $\approx 10\%$ of the absolute age post fertilization) between the youngest and oldest acquired sample. In order to control for possible data variability between different experimental sessions, during every session both the dataset containing the genetic condition of interest plus and a wild type control dataset were acquired. The resulting datasets each contained $6 < N < 10$ valid in toto samples.

After multi-view processing and incorporation of the samples into the common coordinate system, an important analysis to be performed consisted in the statistical testing for differences within a given observable (GFP, RFP, etc...) between different conditions (mutants, perturbations, etc...) and samples. To do so, first the mean value of the observable was extracted for each patch and sample. Hypothesis testing was then implemented by means of data simulation:

1. Data was grouped by experimental day and control or condition.

2. The test statistic τ and null hypothesis H_0 were defined (e.g. the absolute difference of mean GFP values between control and condition and “there is no difference in these values between control and condition”).
3. The experimental test statistic τ_0 was calculated by taking the weighted average of the test statistic obtained for each experimental day based on the respective sample number.
4. Data to calculate the test statistic under H_0 was simulated by randomly shuffling all embryos in the control and condition datasets within a given experimental day, giving τ_i for each permutation.
5. A p-value was approximated by counting the fraction of times the comparison between τ_0 and τ_i contradicts H_0 .

Using this procedure, statistical significance could be estimated in a non parametric way. Importantly, working on observables defined for each tissue patch rather than each voxel within the image helped making the statistical analysis computationally more tractable.

2.2.4 Morphometric quantification of tissue phenotypes

So far, the aim of placing samples into the same coordinate system had been the comparison of fluorescence intensities and protein lifetime ratios. In addition, from the spatial normalisation process information on the morphology of the Cxcr4b expressing tissues can be extracted, complementing the intensity measurements and potentially providing a means to quantify tissue phenotypes. Namely, as a result of placing samples into the CCS, a nonlinear displacement field is obtained which assigns each location x in the CCS with a corresponding location in the original coordinate system of the sample y .

Volume changes as a readout for morphological phenotypes

This displacement field is a vector field $D : \mathbb{R}^3 \rightarrow \mathbb{R}^3, y = x + D(x)$, which provides dense information about the deformations applied by the image transformation and therefore contains any captured differences in sample morphology. In order to analyse these vector fields with the goal of extracting morphological phenotypes, the determinant of the jacobian tensor field of the displacement field is used as a measure in voxel-based morphometry [3]:

$$J_i(x_1, x_2, x_3) = \det \left(\begin{bmatrix} 1 + \frac{\partial D_1}{\partial x_1} & \frac{\partial D_1}{\partial x_2} & \frac{\partial D_1}{\partial x_3} \\ \frac{\partial D_2}{\partial x_1} & 1 + \frac{\partial D_2}{\partial x_2} & \frac{\partial D_2}{\partial x_3} \\ \frac{\partial D_3}{\partial x_1} & \frac{\partial D_3}{\partial x_2} & 1 + \frac{\partial D_3}{\partial x_3} \end{bmatrix} \right) \quad (2.13)$$

For a given input sample i , J_i is defined for every location within the CCS. Its geometrical interpretation is the volume change between the source and the target coordinates of a given transformation. Values of $J_i(x, y, z) > 1$ at a given location indicate that the local environment of this location is stretched when transformed from the CCS to the original sample space. Inversely, values of $J_i(x, y, z) < 1$ indicate a decrease of volume, while values $J_i(x, y, z) = 1$ reflect no stretching or shrinking of the local environment. In general terms, J_i gives the factor by which an infinitesimal volume element in the CCS is expanded when mapped onto the original sample, i.e. $J_i(x, y, z) = 2$ indicates a twofold increase. For ease of interpretation, J will be expressed in binary logarithmic representation, reflecting the negative or positive volume fold change.

It is important to mention that volume changes do not necessarily capture all information relevant for morphological phenotypes contained within the displacement fields. Also, only morphological differences accurately normalized for by the non-linear image registration procedure are present within the vector fields. Keeping

in mind these limitations, due to their clear geometrical interpretation and invariance with respect to the original pose and position of the sample, volume changes represent a suitable measure to quantify morphological phenotypes.

Validation: Detection of developmental asymmetries

To assess whether the proposed method in practice can be used to detect morphological phenotypes, known morphological deformations in the samples were required. Therefore, asymmetries of *Cxcr4b* expressing tissues at 36hpf known from the literature were taken advantage of. These include two structures which form part of the segmented volume shown in Fig. 2.15, namely

- the habenulae, which are more prominent on the right side of the embryo [134] and the
- the pancreas, which is asymmetrically positioned tending towards the right side of the embryo [111].

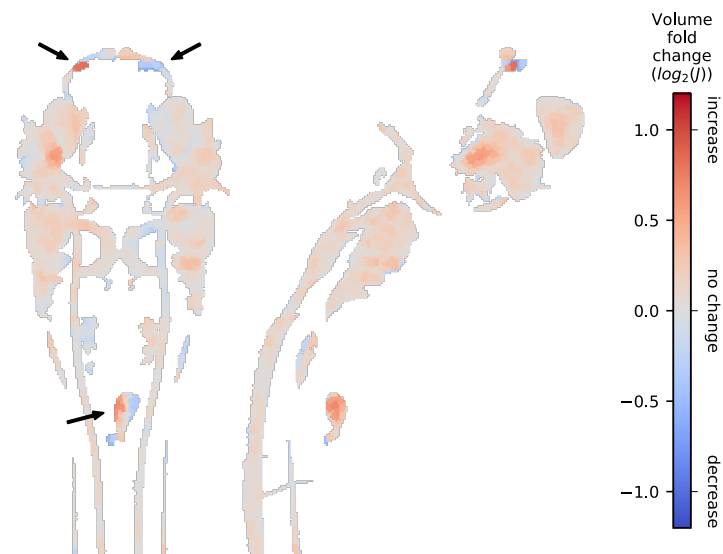
In order to exploit these asymmetries for validation, synthetic test embryos were created by laterally mirroring the bilaterally symmetric wild type embryo stacks. This was performed for wild type datasets from three experimental sessions containing in total $N = 25$ embryos. Then, for each experimental replicate, in addition to the original wild type dataset the laterally mirrored dataset was considered as the associated experimental condition. After placing the samples into the CCS, the volume changes were extracted for each tissue patch and sample as detailed in the previous section.

Fig. 2.17a shows the difference of the mean volume changes between the mirrored and wt datasets. While exhibiting minor differences in many tissues, the strongest volume change can be seen in the habenulae and pancreas. More specifically, the extracted volume changes for the left smaller habenula indicate tissue stretching when compared to the mirrored samples and inversely for the right habenula. Further, the

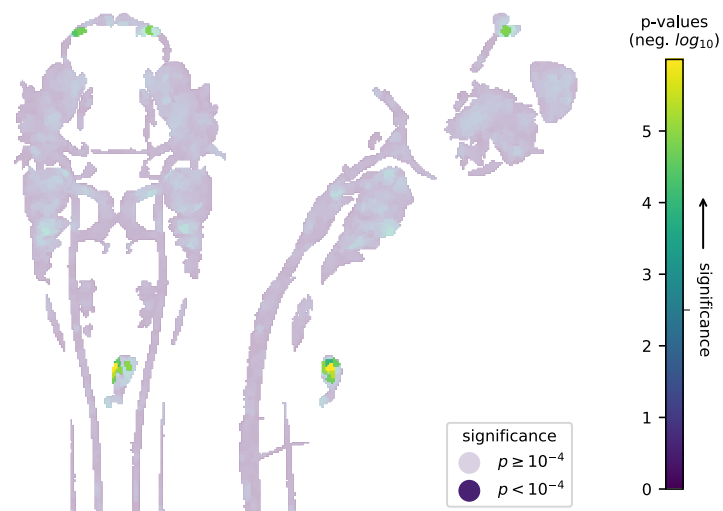
quantitative values of approx. one fold change for both lateral habenulae agree with the approx. volume difference apparent from the segmentation. In the case of the pancreas, both increases and decreases of the volume were captured, representing distortions mapping the organ to a laterally inverted version of itself. Fig. 2.17b shows the p-values resulting from a statistical analysis as described in section 2.2.3, indicating that for the two mentioned tissues the effect was indeed significant (and the most significant) with p-values $p < 10^{-2}$.

Interestingly, also a few other structures exhibit strong p-values, which to our knowledge are however not reported to form part of asymmetric organs. These captured lateral differences might be an effect of slight illumination differences between the left and right light sheets of the microscope, or, alternatively, represent real asymmetries in the embryo. These could for example be a consequence of another, however Cxcr4b negative tissue asymmetry, which is the heart. The indicated areas are located near blood vessels which exhibit a faint GFP signal (but are excluded from the segmented volume) and could be asymmetrically enlarged.

In conclusion, considering p-values $p < 10^{-4}$ the presented method for morphological phenotyping accurately reports on the developmental asymmetries. This validates that both the image registration and the phenotype analysis approach capture both large and small morphological differences given by the asymmetric pancreas and habenulae. Also, despite focusing on volume changes as a phenotypic readout, the analysis captures both the volume differences of the habenulae on one side and the differences in shape and position of the pancreas on the other. In conclusion, the presented analysis represents a suitable method for the automatic detection of morphological phenotypes.



(a) Difference in volume change



(b) P-values

Figure 2.17 – Volume changes in laterally mirrored embryos.

To validate the presented phenotypic analysis, wild type embryos were compared to the same wild type embryos mirrored along their lateral symmetry axis ($N = 25$ each). Known lateral asymmetries of *Cxcr4b* expressing tissue at this stage include the habenulae and the pancreas (see arrows). These are exactly the structures exhibiting the strongest (a) effect sizes (difference of mean volume change between wt and mirrored) and (b) its statistical significance. The images were created by backprojecting the values obtained for each tissue patch, followed by a projection of the values with largest absolute values in the z and x directions.

3 Studying chemokine signaling interactions

The overall aim of this study¹ consisted of gaining a systems level understanding of the signaling activity and function of Cxcr4b and its interactions with the scavenger receptor Cxcr7b during early zebrafish development. Both receptors and their ligands Cxcl12a and Cxcl12b are broadly expressed during early embryogenesis, potentially allowing for interactions in many tissues and processes. Strong expression of these components can be observed during the Pharyngula Period of zebrafish development (24hpf to 48hpf), a period during which the embryo adopts a clear body plan and many important organs are in the process of forming. The body axis and head straighten, guiding the embryo into a developmental stage during which the morphologies of diverse vertebrate species are best comparable (Gould, 1977). Thus, the central timepoint of the pharyngula period, namely 36hpf, was chosen as the focus for analysis due to the strong expression of the chemokine signaling components in many organ systems. Fig. 3.1 shows the expression of Cxcr4b in an in toto reconstruction and identifies some of the key forming structures at 36hpf.

The emergence of tandem fluorescent lifetime reporters made it possible to measure chemokine receptor turnover in living tissues of the zebrafish embryo, as was shown by [40]. As receptor turnover scales with the concentration of activating ligand, the timer represents a powerful tool for reporting also on the functional interactions

¹The work presented in this chapter has been largely performed in collaboration with Erika Donà, a former PhD student in Gilmour group at EMBL Heidelberg.

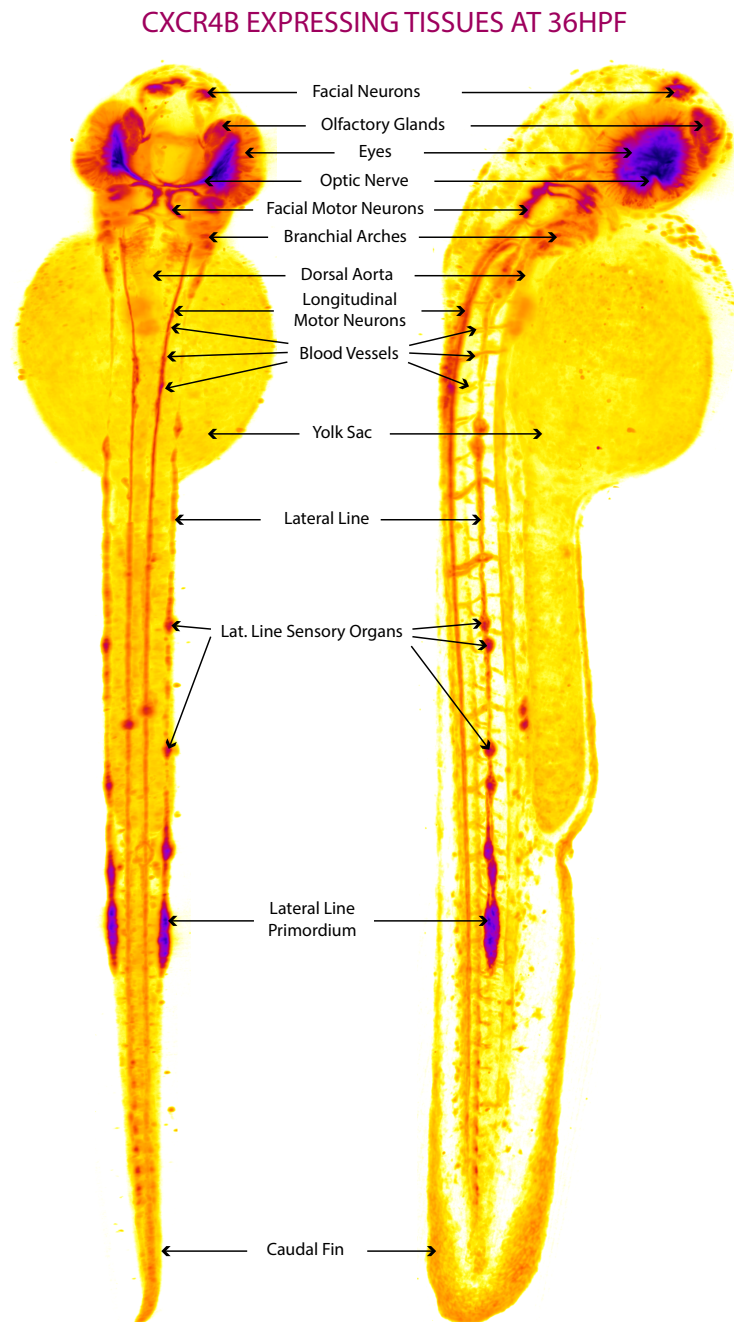


Figure 3.1 – Our focus lies on the developmental stage 36hpf, which marks the midpoint of the Pharyngula Period. The signaling receptor *Cxcr4b*, the scavenger receptor *Cxcr7* and the ligands are widely and highly expressed at this stage. Here, we give an overview of the important structures and forming organs. Lookup table: intensities increase from yellow to violet.

between the chemokine receptor of interest, Cxcr4b, its ligand Cxcl12 and other signaling components potentially interacting with it. We therefore aimed to combine its use with the previously described computational normalisation framework in order to characterise and compare the signaling activity of Cxcr4b in different genetic backgrounds in an unbiased way. Detected changes in signaling rates would then report on ligand mediated interactions between Cxcr4b and the given gene perturbation.

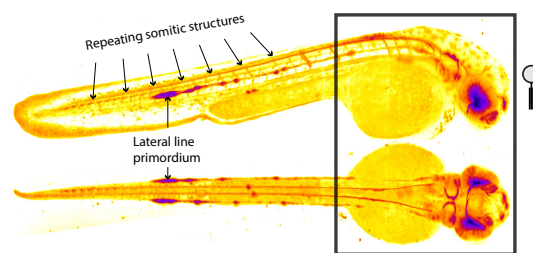


Figure 3.2 – The majority of relevant Cxcr4b expressing tissues are located in the anterior part of the 36hpf old embryo. We therefore focussed on this region, since imaging the entire fish including the tail would have significantly increased acquisition times without improving the coverage of structures of interest.

With the aim of establishing a standard imaging protocol for our unbiased study, we first determined the optimal microscope settings for acquiring embryos at both the embryo scale and cellular resolution. At the lowest magnification compatible with this goal (using a 20x objective in combination with a negative zoom of 0.36x provided by the tube lens), acquiring the full zebrafish embryo would require three longitudinal positions along the anterior-posterior axis of the embryo, along with relatively long acquisition times for every sample. However, as fig. 3.2 shows, most of the volume of the embryo is contained in the anterior most position, even when excluding the yolk sac. Also, most Cxcr4b expressing structures are located in this anterior volume, while the tail of the embryo contains most prominently the lateral line primordium, which in any case needs to be excluded from the analysis because of its highly variable position. The remaining structures mainly consist

of longitudinal nerves and somitic structures that represent metameric ‘repeats’ of tissues already present in the anterior most part of the embryo. Therefore, we decided to only acquire four panoramic views and focus our study on the anterior part of the embryo.

3.1 In toto measurement of fluorescent lifetime ratios

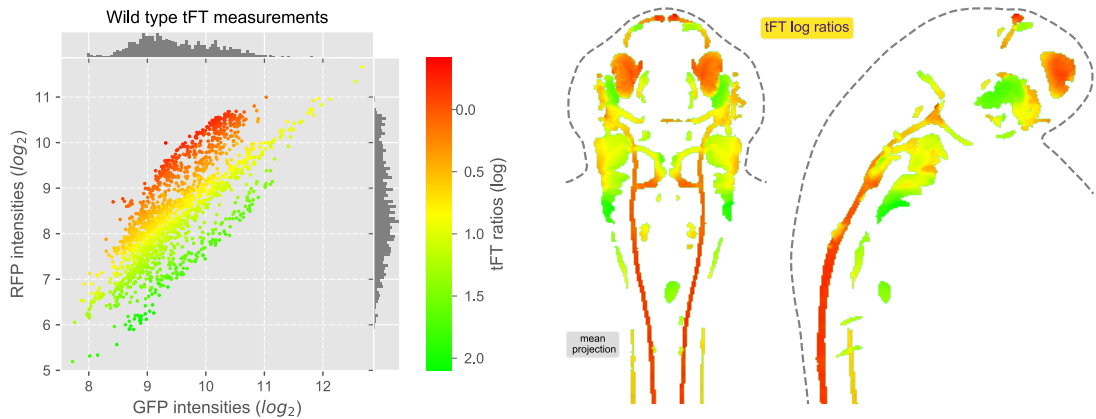
In order to use fluorescent timers as readouts of Cxcr4b signaling activity in an unbiased way in the context of the in toto embryo, we characterised timer measurements performed in combination with the previously described registration framework. The first parameter we investigated was the range and variability of timer measurements from tissue to tissue and embryo to embryo.

To do so, we incorporated acquisitions of wild type embryos expressing the tandem fluorescent timer construct *cxcr4b::sfGFP-tagRFP* at 36dpf into the registration framework. Fig. 3.3 shows both the absolute intensities of the sfGFP and tagRFP channels and the resulting ratios in the segmented tissue patches (see section 2.2.2). The intensity measurements of the fast (sfGFP) and slow maturing (tagRFP) fluorescent proteins exhibit a relatively high degree of decorrelation, leading to ratios spanning a large range of values. Interestingly, interpreting ratios as a readout of average receptor age, the data shows that receptor expression levels and receptor age are not clearly correlated.

Also, ratio values differ largely not only when comparing different regions of the embryo but also within the immediate neighborhoods of the segmented organs. As represented by the lower scatter plot, ratio values do not seem to accumulate on either end of the elicited spectrum and are approx. normally distributed (see the x-axis histogram of the lower scatter plot). Further, fig. 3.3 shows that the oldest receptors can be found in the lateral motor nerves.

3.1 In toto measurement of fluorescent lifetime ratios

Conversely, the receptor proteins of most other tissues are on average younger, meaning they exhibit considerable dynamics that can be captured with the utilised tFT, thereby confirming that the chosen combination of fluorophores exhibits a good sensitivity for a global analysis.



(a) Mean lifetime ratios

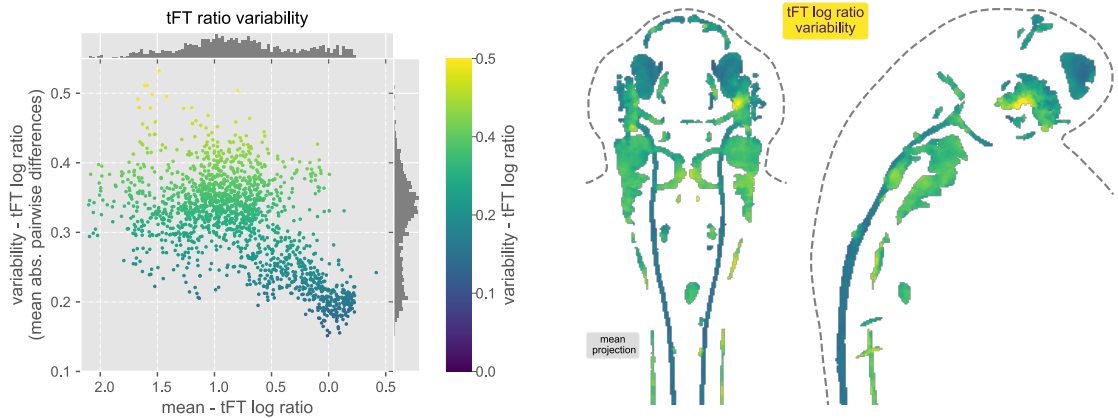
Figure 3.3 – tFT ratio measurements in wild type. Scatter plot of sfGFP vs. tagRFP intensities (log scale) and the resulting tFT ratios (log ratios) in color as measured from the individual tissue patches. On the right, ratios are visualised in the context of the embryo using a mean projection of the same values colored in the scatter plot. The quantification reveals that the tFT ratios, which report on average receptor turnover rates, assume a large range of values (approx. normally distributed as indicated by the x-axis histogram). Ratios vary to a similar degree between organs (or groups of tissues) compared to within organs. Data was obtained from three wild type datasets totalling $N = 25$ embryo recordings.

Fig. 3.4 shows an analysis of the variabilities obtained from the ratio measurements. Ratios exhibit a variability approx. one order of magnitude lower than the total range of the absolute measurements, resulting in an embryo-wide ratio variability comparable to the one obtained for targeted measurements in the migrating pLLP [40]. This variability can include both biological (e.g. differences in signaling rates, embryo age) and technical components (e.g. optical penetrance, misregistrations).

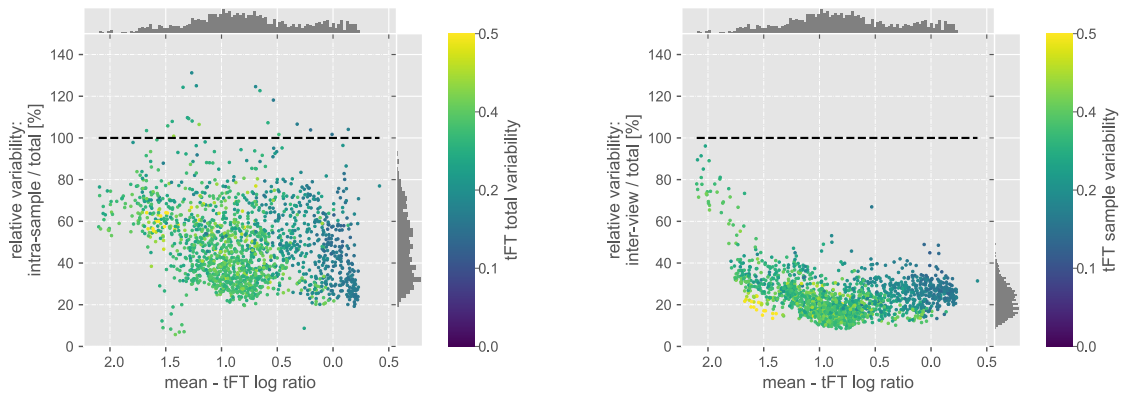
To examine the contributions of the underlying sources of the observed variability, we performed measurements of two types of variabilities:

1. Intra-sample (or within-sample) variability: By incorporating laterally mirrored samples into the normalisation framework and comparing their ratios to those of their unchanged counterparts, the variabilities of the normalisation process in combination with the intrinsic lateral variability can be quantified. It therefore represents both the biological and technical measurement error associated to a single sample or data point. This intra-sample variability is plotted in fig. 3.4b relative to the total sample variability, amounting to values distributed around a mean of approx. 50%. This means that a significant contribution to the total measured ratio variability must be given by ratios differing between samples, thereby resolving individual samples within the measurement error.
2. Inter-view variability: In order to test whether tFT ratios can be accurately measured within the scattering context of the zebrafish embryo, we measured the variability between ratios obtained from different acquisition angles of the multi-view light sheet setup. Three of four registered but unfused views were considered, excluding for every given sample location the worst view as indicated by the image quality measure described in sec. 2.1.2. As different views represent different total penetration depths of illumination and detection within the sample, this measure estimates the contribution of varying optical penetrance to the ratio measurement error. As Fig. 3.4c shows, for most tissues this error stays well below 50% of the total ratio variability, supporting the conclusion that the measurement error introduced by varying optical penetrance is contained within the sampling variability.

3.1 In toto measurement of fluorescent lifetime ratios



(a) Total ratio variability



(b) Intra-sample variability

(c) Inter-view variability

Figure 3.4 – tFT ratio variability

a) total (sample) variability: log tFT ratios on the x-axis vs. total absolute ratio variability on the y-axis. The variability was calculated as the average absolute pairwise difference between samples from the same dataset.

b) log tFT ratios vs. intra-sample relative to total variability. Intra-sample variability was calculated as the average pairwise absolute ratio difference between samples and their laterally mirrored counterparts, thereby including all sources of intra-sample variability: spatial normalisation errors and biological intra-sample variation.

c) log tFT ratios vs. multi-view acquisition variability, i.e. the ratio variability between the multi-view angles before view fusion. This estimates the variability arising from measuring tFT ratios at different locations within the sample.

3.2 Cxcr4b receptor signaling dynamics

3.2.1 Cxcr4b receptor activity is regulated globally by the endogenous Cxcl12 chemokine ligand distribution

Having observed that Cxcr4b receptors are differentially expressed at 36hpf and exhibit different ages across the embryo, we next asked whether receptors had been exposed to chemokines. As introduced earlier, it is known that zebrafish Cxcr4b has two ligands, Cxcl12a and Cxcl12b, which it binds with different affinities. To probe the presence of these interactions in the embryo we compared the expression of the fluorescent timer construct between wild type background and embryos deficient for both chemokine ligands.

Fig. 3.5 contains the quantifications of these embryos after incorporation into the spatial normalisation framework. We find that average ratios all across the segmented tissues show a shift towards higher values. As indicated by the histograms, the distribution of values in the mutant is much narrower than in the wild type. The lower part of the figure shows the result of a statistical analysis of the ratio comparison as detailed in sec. 2.2.3, which yields that 79% of the tissue patches exhibit a significant increase in ratio, while no patch shows a decrease. Notably, the tissues which do not show a ratio increase already have some of the highest ratios in wild type. A reasonable explanation therefore is that the ratios in these tissues have reached their maximal possible value, which is the case when all tagRFP fluorophores have matured and the chosen timer has reached its sensitivity limit.

One clear conclusion resulting from differing ratios between wild type and ligand mutant in the majority of tissues is that before the analysed point in time the receptor had been interacting with at least one of its ligands. Ratios increasing in value means that receptor populations are older. As detailed in sec. 1.2.2, one explanation for a higher ratio when comparing two receptor populations can be

3.2 Cxcr4b receptor signaling dynamics

decreased protein degradation in case of comparable production rates. As Cxcr4b can be degraded when exposed to its ligand, a lack of the latter would lead to lower degradation and therefore lower receptor turnover. To test how receptor levels compare between wild type and ligand mutant in our experiment, fig. 3.6 shows the relative change in receptor concentrations as measured by the sfGFP signal. Indeed, most receptor concentrations increase in the ligand mutant. Furthermore, the change in ratios correlates with the relative change in receptor concentration. Therefore, the increase in both receptor ages and expression levels is compelling support for the interpretation that in the absence of Cxcl12, Cxcr4b receptor turnover decreases in the vast majority of expressing tissues, if not all. This reveals that the pattern of receptor turnover observed across wild-type embryos emerges for interactions between Cxcr4b and its endogenous ligand Cxcl12a. indicates that in the highlighted tissues, Cxcr4b is turning over due to ligand binding in wild type.

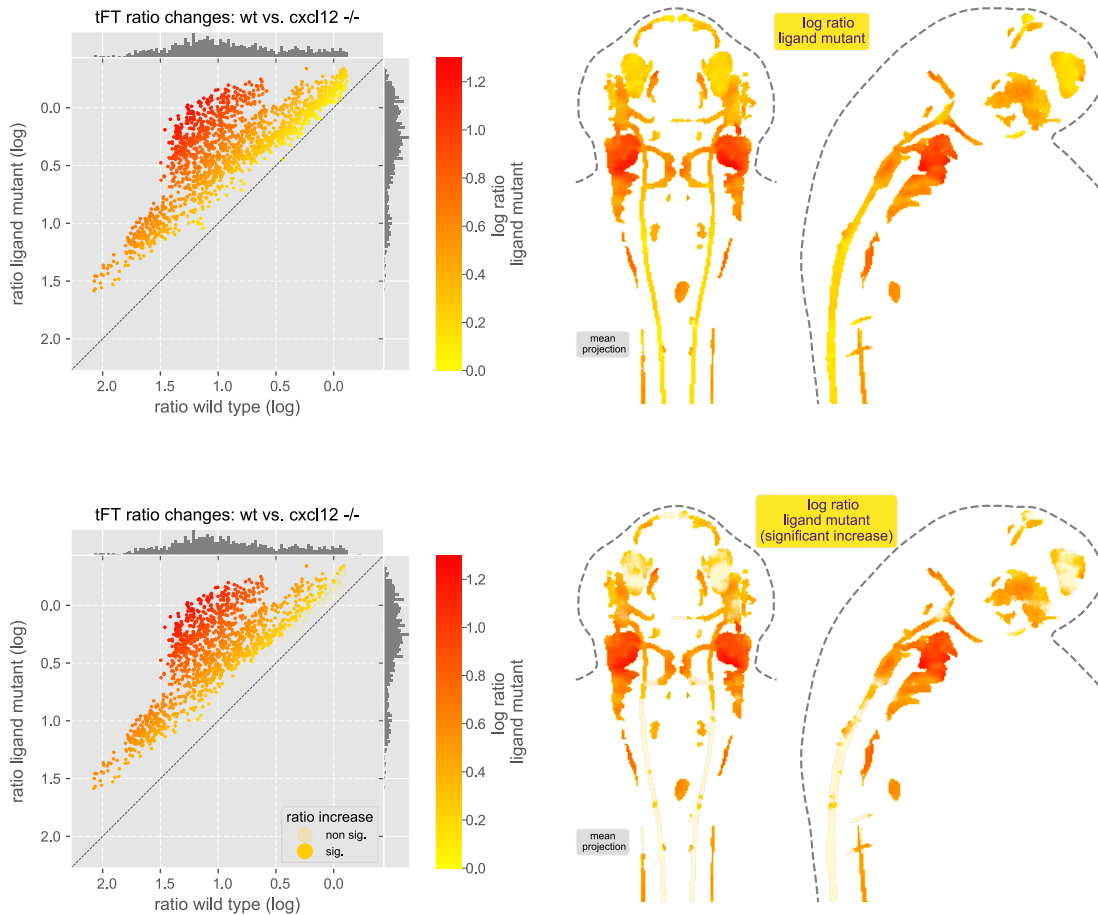


Figure 3.5 – tFT ratio comparison: wt vs. ligand mutant

Top: The scatter plot compares log wild type ratios vs. log ratios in the ligand mutant *cxcl12*^{-/-} (double knockout for *cxcl12a* and *cxcl12b*). Color-coded is the ratio difference between the two conditions. The majority of tissues shows an increase in the ratios.

Bottom: Shown in solid color are those tissues showing a statistically significant increase ($p < 0.05$) in ratios from wild type to the ligand mutant (79%, no tissues show a stat. sig. decrease): In these tissues, *cxcr4b* turnover rates decrease in the absence of the ligand, meaning that in wild type they are sensitive to its presence. Data includes a total of $N_{wt} = 8$ and $N_{cxcl12^{-/-}} = 7$ samples.

3.2 Cxcr4b receptor signaling dynamics

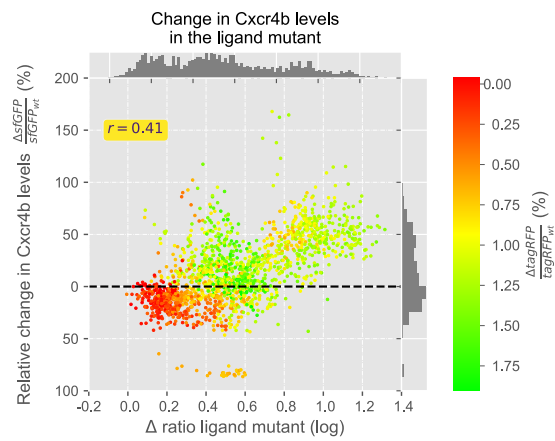


Figure 3.6 – Differences in Cxcr4b expression levels between wt and ligand mutant. The increase in the ligand correlates with the change in lifetime ratios.

3.2.2 Widespread chemokine receptor hyperactivation in absence of scavenger Cxcr7

In the experiment detailed in the previous section we observed that Cxcr4b turnover is sensitive to loss of either Cxcl12a or Cxcl12b ligand in the majority of tissues. As the scavenger protein Cxcr7b is also known to be able to bind both of these ligands, we next asked whether the pattern of chemokine receptor-ligand interactions is influenced by the scavenger receptor. If so, how widespread is this impact of the scavenger and what occurs in the tissues in which the receptor-chemokine signaling seems to be rather low? To address the influence of Cxcr7b on Cxcr4b dynamics, similarly to the previous experiment we compared the expression of Cxcr4b-tFT in wild type to embryos lacking Cxcr7b.

Fig. 3.7 shows the quantification of these samples after incorporation into the spatial normalisation framework, comparing the ratios between the two conditions and mapping the differences onto the reference embryo. We find that in the mutant, the histogram of ratios widens and the majority of tissues shows a decrease in fluorescent lifetime ratios. Therefore, the average age of receptor populations changes in the absence of the scavenger. From here we conclude that the scavenger interacts with Cxcr4b and, surprisingly, this interaction affects the majority of expressing tissues.

In order to further interpret the ratio changes we compare the receptor levels between the two analysed conditions, shown in fig. 3.8. We find that similarly to the case of the ligand mutant, the change in ratios correlates with a change in receptor expression levels: a decrease in ratios is associated to a decrease in concentrations. Together with the finding that receptor ages decrease broadly, this is consistent with Cxcr4b receptor turnover increasing strongly in the absence of Cxcr7b, which normally competes for the same ligands. Therefore we conclude that in wild type, the Cxcr4b turnover rates of most tissues due to their exposure to SDF is strongly determined by the scavenging action of Cxcr7b on the ligands.

Although it was known that Cxcr7b can bind to the ligands, it was not known whether this would have an impact on Cxcr4b signaling on a systemic level in vivo. As opposed to zebrafish embryos lacking Cxcr7b, Cxcr7 deficiency in mice is lethal [169]. Therefore, one hypothesis explaining *cxcr7b*^{-/-} viability in zebrafish addresses a possible redundancy between Cxcr7b and Cxcr7a, which can potentially bind to the same ligands. Instead, our experiment shows that, if present, such potential redundancy does not prevent the functional hyperactivation of Cxcr4b signaling level in vivo.

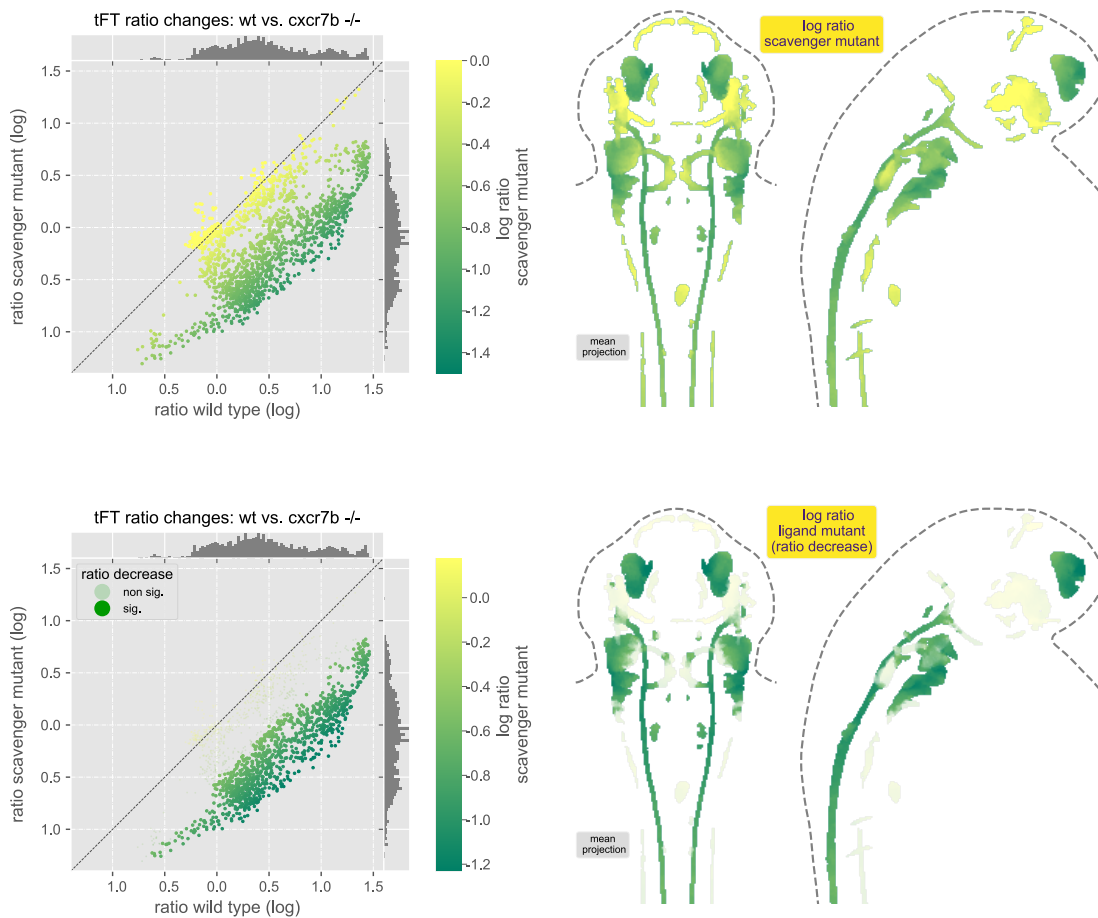


Figure 3.7 – tFT ratio comparison: wt vs. scavenger mutant

Top: The scatter plot compares log wild type ratios vs. log ratios in the scavenger mutant $cxcr7b^{-/-}$. Color-coded is the ratio difference between the two conditions. As opposed to the case of a lacking ligand, in case of removing the scavenger receptor, the majority of tissues show a decrease in the ratios.

Bottom: Shown in solid color are those tissues showing a statistically significant decrease ($p < 0.05$) in ratios from wild type to the scavenger mutant (63%, no tissue shows a stat. sig. increase): In these tissues, $cxcr4b$ turnover rates decrease in the absence of the scavenger, likely reflecting an increase of available ligand. This provides evidence for a widespread competition between $Cxcr4b$ and $Cxcr7b$ for $Cxcl12$.

Data includes a total of $N_{wt} = 23$ and $N_{cxcr7b^{-/-}} = 27$ samples.

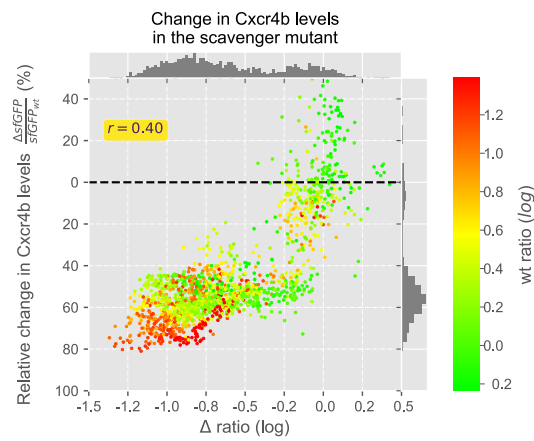


Figure 3.8 – Differences in Cxcr4b expression levels between wt and ligand mutant. The increase in the ligand correlates with the change in lifetime ratios.

3.2.3 In toto comparison of the effect of ligands and scavenger on Cxcr4b in vivo

Comparing the mapped ratio differences in figures 3.5 and 3.7, it becomes apparent that the tissues interacting with either ligands or scavengers do not necessarily overlap. Since all embryo measurements are normalised to occupy the same coordinate system, we can directly compare the ratio changes due to one with those due to the other. Fig. 3.9 shows the corresponding average values and in color mapped the different statistical significance cases.

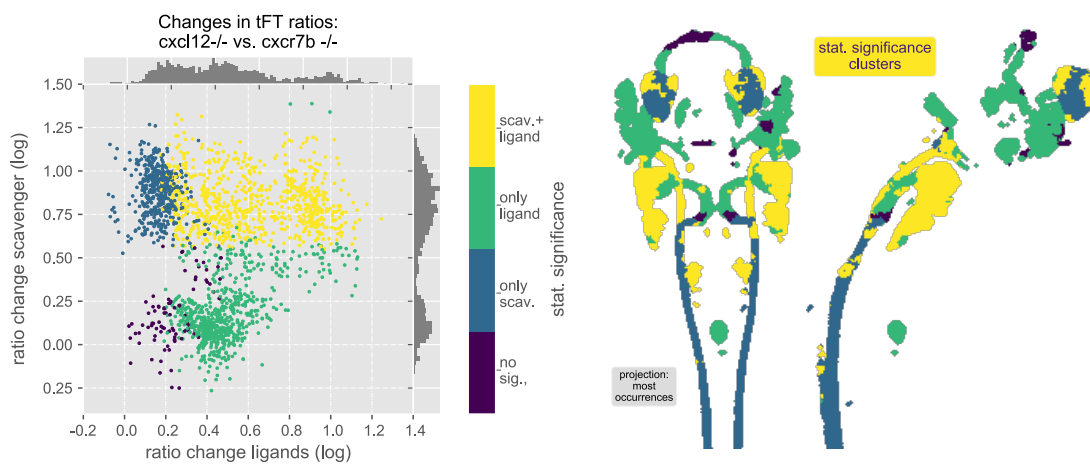


Figure 3.9 – The scatter plot compares the ratio changes between wild type and the ligands mutant ($cxcr12a^{-/-}cxcr12b^{-/-}$) and the scavenger mutant ($cxcr7b^{-/-}$) respectively. The different colors indicate the different combinations of whether or not the ratio change is statistically significant for the given mutant.

As discussed previously, tissues can be divided into those for which there is a clear sensitivity to the ligand and those for which we cannot detect a strong and significant ratio change in its absence. Interestingly however, within the latter class most patches exhibit a strong response to the scavenger. One interpretation is that in these tissues the scavenger is so efficient at reducing available ligand that there is little effect on receptor turnover when the ligand is depleted. Interestingly, few

tissues in the ligand insensitive group show no response to the scavenger. We therefore propose that in vivo, the scavenger has a regulatory effect on Cxcr4b signaling whose magnitude is comparable to that of the ligand itself.

3.3 Correlating scavenger expression pattern to its signaling impact

3.3.1 Chemokine receptor turnover increase does not tightly correlate with Cxcr7b expression profile

Our finding that Cxcr4b turnover rates were increased in the majority of tissues in *cxcr7b*^{-/-} mutants suggests that there exists a broad interaction between the two receptors. We wanted to investigate this interaction further: Most likely the receptors compete for their common ligands, therefore a dependency between the expression or presence of Cxcr7b and its effect on Cxcr4b turnover rates could be expected. More precisely, one would expect a higher increase in receptor turnover rates in mutants in regions where Cxcr7b expression is higher and therefore leads to a higher sinking activity. To find out whether this is the case we compared the results from section 3.2.2 with a dataset adding Cxcr7b expression data to the framework, using the *cxcr4b::cxcr4b-sfGFP; cxcr7b::lyn-tagRFP* transgenic fish line.

The results are shown in fig. 3.10 which compares ratio changes in Cxcr4b-tFT in *cxcr7b*^{-/-} and Cxcr7b expression for every tissue patch. Interestingly, a clear monotonous relationship between the two quantities does not become apparent: Patches exist for which despite high receptor expression, no strong ratio change can be measured. Conversely, ratio changes are shown in some regions in which Cxcr7b exhibits relatively low expression levels. Despite the absence of a monotonous correlation between the two quantities, a strong difference can be observed when comparing the median Cxcr7b expression of the tissues exhibiting a significant ratio

change and those which do not. Also, applying Kendall's tau as a measure of correlation between the two quantities results in a statistically significant anti-correlation ($C_\tau = -0.139$), confirming an expected relationship.

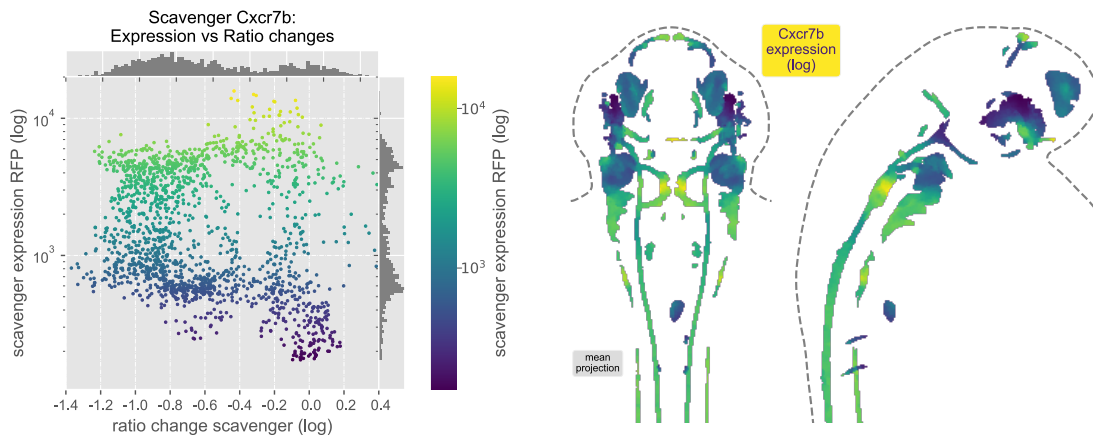


Figure 3.10 – The scatter plot compares the ratio change from wild type to *cxcr7b*^{-/-} mutant on the x-axis with the expression of Cxcr7b in the tissue patches on the y-axis and in color (shown on a logarithmic scale). A clear monotonous relationship or correlation between the two quantities cannot be observed. However, the median intensity for the tissue patches exhibiting significant ratio differences is approx. double the median intensity for those tissues unaffected by the lack of Cxcr7b. Also, Kendall's Tau rank correlation analysis reveals a significant anti correlation with a coefficient of $C_\tau = -0.139$.

Cxcr7b expression data was obtained from $N = 5$ samples.

A technical explanation for the obtained relatively weak correlation could be the fact that the observed Cxcr7b readout is a transcriptional reporter, where Cxcr7b regulatory elements drive a membrane tethered RFP which, unlike Cxcr7, is not actively degraded. This reduced turnover results in perdurance of expression and labeling of tissues that may no longer express the Cxcr7 protein. This however does not explain the presence of very low expressing patches exhibiting high turnover rate changes.

3.3.2 Modelling a potential long range Cxcr7b-Cxcr4b interaction

Alternatively, the spatial accordance between expression levels and effects on Cxcr4b-tFT turnover rates might be explained by an interaction which does not act exclusively locally: As the ligand can diffuse through the extracellular space, the scavenger might affect its concentrations not only in its immediate neighborhood, but over a distance. In this case, one would expect a given signaling receptor to also 'sense' scavenger expression domains located at a distance. To simulate this scenario, we performed a progressive signal dilation or blurring of the Cxcr7b expression pattern: For a given iteration, the signal was blurred using a gaussian filter ($\sigma = 1\mu m$) and the maximum of this blurred signal and the original signal was kept as the resulting dilated signal, used as the starting point for the next iteration (see fig. 3.11 on the right for an illustration of this signal dilation process in maximum projections and an exemplary expression profile). We then calculated the correlation (Kendall's tau) between the ratio changes and the different dilation iteration numbers (fig. 3.11 on the left).

In case of an exclusively local interaction between Cxcr4b and Cxcr7b we would expect an immediate drop of the correlation value as the signal becomes diluted, because the local expression levels would explain ratio changes better than blurred ones. However, we find the opposite: Up to an iteration number of $i=30$, the two quantities become more anti-correlated before reversing this trend for further increasing signal dilations. This correlation minimum or anti-correlation maximum (significance) would suggest that a non-local interaction over a spatial range of approx. $\Delta x \approx 30\mu m$ between Cxcr4b and Cxcr7b is better supported than a purely local one by the experimental data. However, although significant, the observed changes in the correlation values are too low to draw strong conclusions at this point.

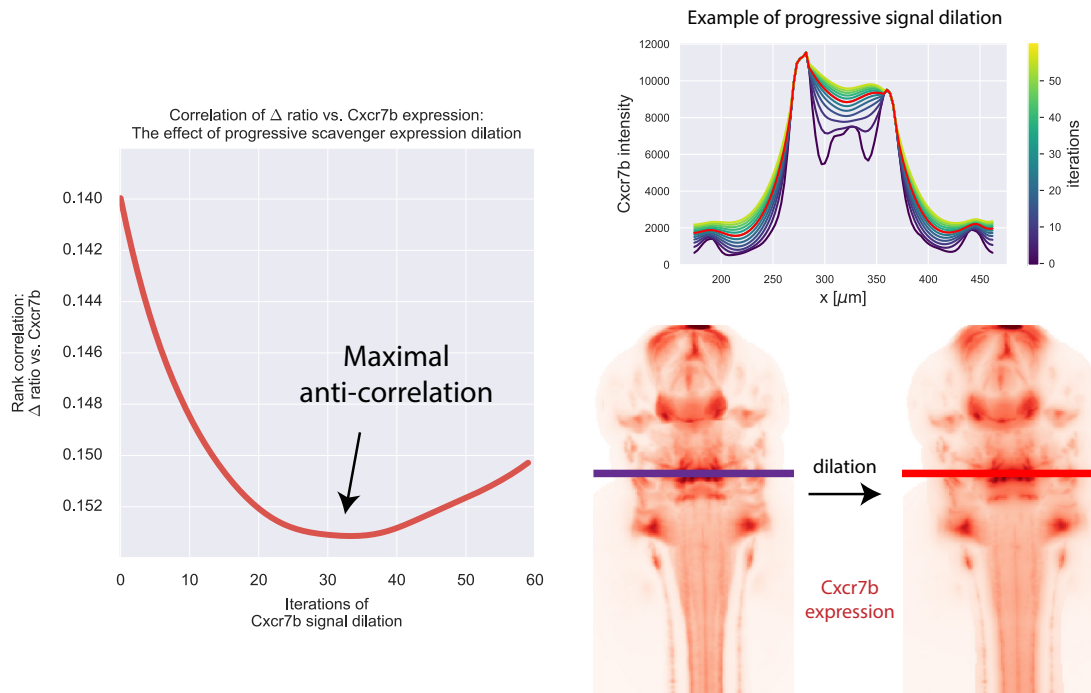


Figure 3.11 – The effect of dilating the Cxcr7b signal on the (anti-)correlation (Kendall’s tau) between ratio changes in *cxcr7b*^{-/-} and Cxcr7b expression was tested. The dilation consisting of an iterative blurring of the Cxcr7b intensities models the case in which Cxcr4b can sense not only its immediately local Cxcr7b concentration, but within an extended neighborhood. The two panels at the right illustrate this signal dilation. Finding a correlation minimum at a non-zero iteration could reflect the presence of long-range interactions between the two receptors.

3.4 Addressing impact of chemokine receptor hyperactivation on tissue positioning and morphology

In sec. 3.2.2 we found that Cxcr4b receptor turnover was significantly increased in the absence of the scavenger in nearly 70% of the tissues expressing Cxcr4b. Given such a systemic and hyperactivating effect of Cxcr7b, it is surprising that *cxcr7b*^{-/-} zebrafish embryos are homozygously viable and develop into fertile adults. Therefore we asked whether Cxcr7b activation has a phenotypic consequence on the tissue level. More specifically, as Cxcr4b is strongly involved in promoting cell migration

3.4 Addressing impact of chemokine receptor hyperactivation on tissue positioning and morphology

and proliferation, we were interested in morphological differences between wild type and mutant tissues. To investigate this, we made use of the analysis presented in sec. 2.2.4, which quantitatively analyses the deformations required to map a sample into the normalised reference space and extracts tissue volume changes as a measure for morphological phenotypes.

For this analysis we used the same normalised samples as in sec. 3.2.2, making it possible to compare ratio differences between the scavenger mutant and wild type to the morphological phenotype score for every tissue patch in the embryo. As the volume changes between genetic conditions represent a rather noisy measurement, instead of absolute volume changes for this analysis we consider the volume change effect size defined as the difference between the mean volumes of the scavenger and the wild type datasets divided by the standard deviation of the wild type [56]:

$$\Delta = \sum_{ds} \frac{\bar{J}_{cxcr7b^{-/-},ds} - \bar{J}_{wt,ds}}{\sigma_{wt,ds}}$$

With this definition, a volume change becomes more pronounced if the variation exhibited by the wild type is small and vice versa if the baseline variation is already high. By considering only the wild type variation instead of a pooled variation of both populations, Δ becomes more sensitive by taking into account the assumption that the variability in the mutant case is likely to be higher than in the wild type case, as is the case for gene deletion phenotypes in general (and in particular the case of the pLLP migration arrest in *cxcr7b*^{-/-}). Therefore, it gives a quantitative estimation of how unlikely a given observed volume change is, leading us to interpret this quantity as an indicator of putative morphological phenotypes. Fig. 3.12a shows a plot of ratio changes vs Δ , mapping the absolute values of the latter onto the embryo (negative and positive values of Δ indicate smaller and larger tissue volumes in the mutant respectively, while its absolute value does not distinguish

between both cases and thereby provides a measure of the strength of the considered volume change).

In terms of the comparison between chemokine receptor ratio changes and tissue volume changes, surprisingly we find that there is not a clear dependence between the two quantities. This could have been expected as there could be a phenotypic consequence of the increase in receptor turnover and thereby *Cxcr4b* signaling activity. Rather, the phenotypic measurements show a largely uncorrelated variability, exhibiting a weak trend of volumes becoming smaller in the mutant as ratios decrease. This, however, can be accounted to the fact that, as shown earlier in section REF, receptor levels decrease in the mutant as ratios also decrease. Given that the sfGFP intensity pattern had been used as a reference marker for the spatial normalisation of the analysed embryos, these volume decreases can be attributed to this process being sensitive to strong differences in fluorophore intensities. As discussed in sec. REF, ideally this phenotyping experiment would be conducted with completely stable reference markers.

Having identified this systematic pattern in the data, we further investigated how reliably the phenotype quantification captures real phenotypes. Therefore, we included the otherwise partly excluded lateral line into the mapping, showing the quantification values also for this region.

Studying the distribution of Δ , we find that some of the largest values are achieved in the lateral line (up to a four fold increase compared to the wild type), indicating a strong change in volumes here. This can be explained by the difference between the large volume occupied by the arrested primordium in the mutant and the much smaller volume occupied by the deposited chain cells and neuromasts in the wild type embryos, due to the primordium migrating out of the field of view in the latter. By confirming this known phenotype in *cxcr7b*^{-/-}, this shows that the used measure for morphological phenotypes successfully detects phenotypes.

3.4 Addressing impact of chemokine receptor hyperactivation on tissue positioning and morphology

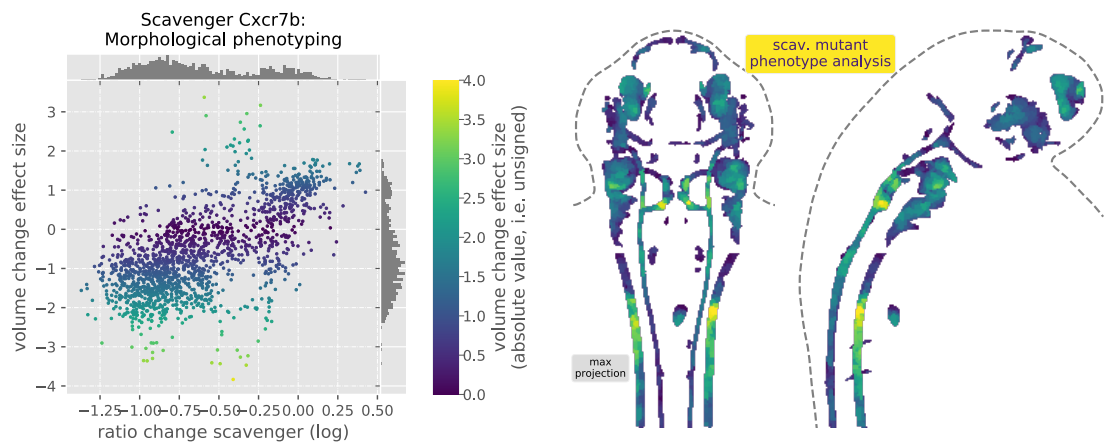
A second region shows high scores comparable to those in the lateral line, suggesting the facial motor neurons as a phenotypic tissue in the scavenger mutant. To study whether this was indeed the case, we identified this tissue in the raw images which have not been normalised and would, as opposed to the normalised image stacks, retain any real differences. This data is shown in fig. 3.12 and represents a reproducibly present phenotype in the scavenger mutant. While in the wild type the facial motor neurons are distributed along the shape of an arch, this pattern in the mutant is often interrupted. A further analysis of the deformation fields details the average morphological differences in 3D, also depicted in fig. 3.12: as can be seen when going through image stacks of the mutant, neurons accumulate in the anterior part of the tissue and become less dense when moving posteriorly. While our automated phenotyping approach uncovered this phenotype in an unbiased way, a report of it could be found in literature [32] describing a defect in the tangential migration of facial motor neurons.

Together, the regions of the lateral line and the facial motor neurons represent the highest obtained phenotypic scores in the scavenger mutant. For the remaining more moderate scores we could not identify any associated phenotypes. While some of the highlighted regions respond to the previously described effect when comparing differing fluorophore intensities, we notice that most of the remaining moderate effect sizes (volume changes increased up to three times compared to the wild type) appear in the more thicker tissues which are represented as maximum projections of the embryo. Therefore, the probability of observing high effect sizes in these regions is increased due to an abundance of measurements (there is an increased probability of rare events, an effect addressed by multiple comparison correction in statistics).

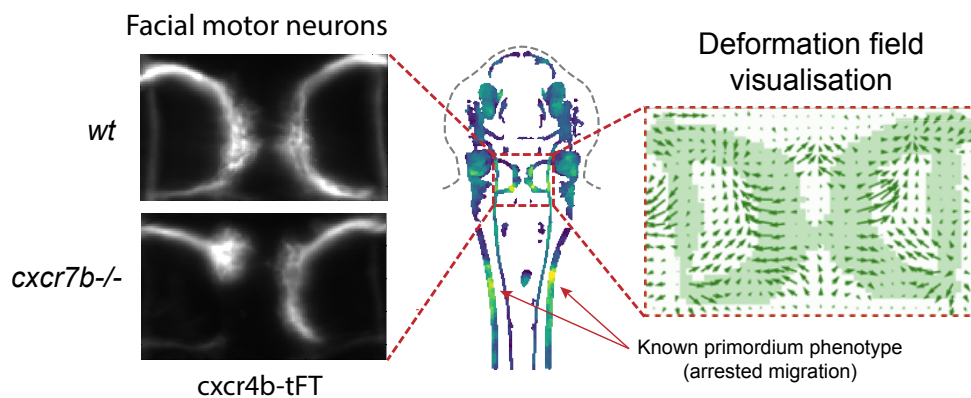
Finally, having identified the arrested pLLP and the facial motor neurons as two already characterised phenotypes, we conclude that our automated morphological phenotyping method successfully identified existing *cxcr7b*^{-/-} phenotypes at 36hpf in the zebrafish embryo. At the same time, all other analysed regions in the embryo showed much lower phenotypic scores, suggesting that the remaining majority

of tissues are aphenotypic in terms of their morphology, at least not to a degree comparable to the reported phenotypes.

3.4 Addressing impact of chemokine receptor hyperactivation on tissue positioning and morphology



(a) Morphological phenotype quantification



(b) Facial motor neuron phenotype

Figure 3.12 – Morphological phenotypes of $cxcr7b^{-/-}$

Top: Automated morphological phenotype quantification. The effect sizes compare volume changes between wild type and mutant to the variation present in the wild type. In addition to the segmented tissues, here the lateral line is included in the visualisation.

Bottom: Besides the lateral line, the highest phenotypic scores are obtained for the facial motor neurons, which are identified here in the raw data and in an analysis of average deformations characterising the phenotype.

Data includes a total of $N_{wt} = 23$ and $N_{cxcr7b^{-/-}} = 27$ samples.

3.5 Testing the role of desensitization in providing phenotypic robustness

Using unbiased phenotyping analysis demonstrates that, besides the two phenotypes already described in literature, the majority of the analysed tissues appears aphe-notypic in *cxc7b*^{-/-}. This was surprising considering that our analysis of lifetime ratios suggests a strong increase in Cxcr4b turnover in the scavenger mutant. Thus, while in other contexts a gene deletion can be compensated for by 'rescue' by genetic redundancy, this does not seem to be the case here. Therefore the question arises how this apparent robustness is achieved. One hypothesis considers our finding that, as turnover increases in the scavenger mutant, receptor concentrations decrease (see fig. 3.8), a process known as receptor desensitization. Potentially, decreased receptor levels could lead to a net decrease of downstream signaling despite increased turnover. Therefore, this desensitization could provide the observed phenotypic robustness.

The optimal way of testing this hypothesis would be to prevent receptor desensitization in the scavenger mutant and compare the phenotypic output in this case to that of the otherwise unperturbed scavenger mutant.

Such an experimental condition could be created by making use of a genetic perturbation of Cxcr4b by truncating the receptor C-terminal tail which contains sequences that targets protein for degradation. The resultant receptor, named Cxcr4b*, is not degraded in vivo but otherwise remains functional. This had been achieved by truncating serine residues in the receptor C-terminus, which are targets for protein degradation. As in the case of the wild type Cxcr4b, the modified receptor is expressed using a BAC, therefore representing a receptor pool additional to the endogenously present Cxcr4b.

Due to its C-terminus truncation, we expected Cxcr4b* degradation not to be increased in a scavenger mutant background. Then, the desensitization hypothesis

would be confirmed if, as opposed to wild type Cxcr4b, the expression of Cxcr4b* would lead to strongly increased phenotypes in a scavenger mutant background.

3.5.1 Preventing Cxcr4b desensitization enhances the pLLP migration phenotype in the absence of Cxcr7

Having a good knowledge of the importance of Cxcr7b on Cxcr4b mediated pLLP migration, we first assessed the effect of introducing the non-degradable Cxcr4b*. How is primordium migration affected when Cxcr4b is not degraded? To find out, we compared embryos in different genetic backgrounds regarding the presence of Cxcr7b, expressing at the same time either Cxcr4b or Cxcr4b* fused to the same timer construct used for analysis so far.

Fig. 3.13 shows the normalised migrated distances of the pLLP along the lateral line in the different genetic conditions. As a control, we observe that wild type Cxcr4b with the scavenger present migrates the full distance. In the scavenger mutant background the known arrested migration can be observed with a mean migrated distance of approx. 40%. In case of Cxcr4b* in mutant background, we observe that this distance is significantly reduced to on average less than 10%. Interestingly, Cxcr4b* in either wild type or heterozygous scavenger background reduces the total migrated distance compared to the control.

From these experiments we conclude that, in the lateral line, replacing Cxcr4b by its non-degradable version Cxcr4b* does strengthen the phenotype elicited in the scavenger mutant, supporting the hypothesis that receptor desensitization does provide one source of robustness in the case of this tissue. Interestingly, both in wild type and heterozygous scavenger background, Cxcr4b* appears to affect primordium migration by itself.

From these experiments we conclude that, in the lateral line, replacing Cxcr4b by its non degradable version Cxcr4b* does strengthen the phenotype elicited in the scav-

enger mutant. However, either in wild type or heterozygous scavenger background, *Cxcr4b** appears to affect primordium migration by itself. In this context and assay it is difficult to distinguish whether the observed effect of preventing *Cxcr4b* from degrading in the homozygous scavenger mutant is

1. an additive phenotype of the two independent perturbations or
2. a stronger effect resulting from a higher order interplay between the two perturbations.

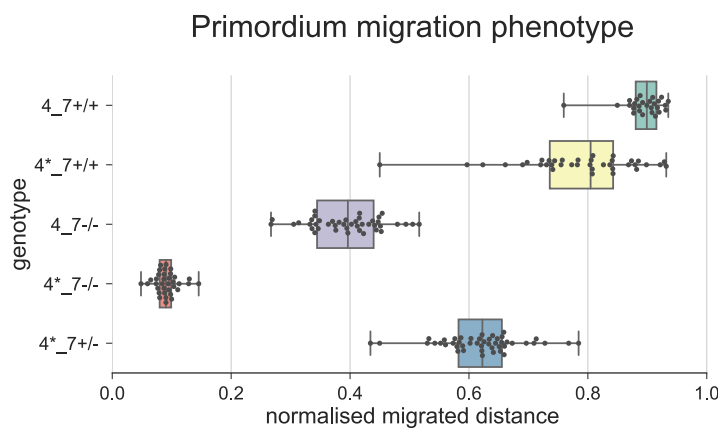


Figure 3.13 – pLLP migration phenotype of wt *Cxcr4b*-tFT and *Cxcr4b**-tFT in different scavenger related genetic backgrounds (4 refers to *Cxcr4b* and 7 to *Cxcr7b*).

3.5.2 Preventing *Cxcr4b* desensitisation does not lead to additional phenotypes in *cxcr7b*^{-/-}

Having assessed that preventing *Cxcr4b* degradation does have an effect on the phenotype of the scavenger mutant in the lateral line, we extended this analysis to the remaining *Cxcr4b* target tissues in the embryo. Which effect does the maintenance of *Cxcr4b* levels have on the different tissues in the absence of the scavenger and its resulting high concentrations of chemokine?

3.5 Testing the role of desensitization in providing phenotypic robustness

To test this, we incorporated embryos expressing $\text{cxcr4b}::\text{cxcr4b}^*\text{-tFT}$ in a $\text{cxcr7b}^{-/-}$ background into the analysis framework. First we assessed that indeed receptor levels of Cxcr4b^* , as opposed to the case of wild type Cxcr4b , in the scavenger mutant did not decrease when compared to wild type Cxcr4b in the presence of the scavenger. The results are shown in fig. 3.14 in terms of relative sfGFP expression and reveal that, while in wild type receptor levels strongly and broadly decrease (as already seen in section 3.2.2), this is not the case when expressing the non degradable Cxcr4b^* . Instead, receptor levels are elevated, which is as expected as Cxcr4b turnover does not solely occur due to the absence of scavenger protein.

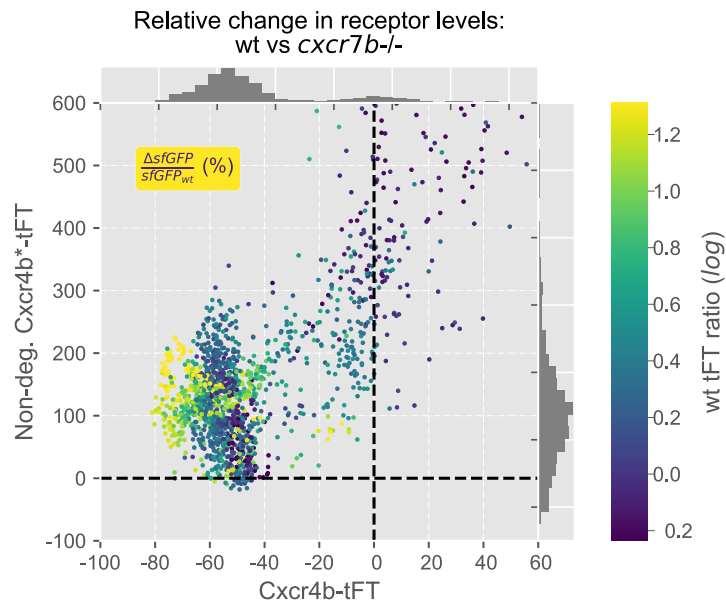


Figure 3.14 – Non-degradable Cxcr4b^* , in contrast to Cxcr4b , remains in high levels in $\text{cxcr7b}^{-/-}$ mutants.

Next, we compared the morphological phenotype scores between the two conditions. Fig. 3.15 shows a side-by-side comparison of the obtained volume change effect sizes (same definition as in section 3.4). Again, the lateral line is additionally included in the visualisation and the range of displayed score value is identical for both

scenarios. Overall, we find that phenotype scores are very similar between the scavenger mutant expressing either the wild type or non degradable Cxcr4b. Fig. 3.15 shows a direct comparison of the obtained numerical values. As a technical note, this graph reveals that the previously discussed tendency of finding overall volume decreases due to fluorophore intensity loss is not present in the case Cxcr4b*, which confirms this systematic measurement bias. Further, phenotypic scores scatter approx. symmetrically around the mean, but importantly agree in their extreme values. In both cases we observe some of the strongest scores in the lateral line, which represent the pLLP migration phenotype. The mappings reveal a narrowing of the distribution of high scores in Cxcr4b*, confirming the previously found strengthening of this phenotype. Also, the defect in facial motor neuron migration is present in both conditions. Equally here, a slight strengthening of the phenotype in Cxcr4b* can be inferred from an increase in the phenotypic scores in the already highlighted regions in wild type Cxcr4b. However, interestingly we could not detect additional morphological phenotypes in other target tissues when expressing Cxcr4b*.

As a control, fig. 3.15d shows the phenotype scores obtained for expressing Cxcr4b* in a wild type background. Both above mentioned phenotypes are not visible here and in general, phenotypic scores are low with one exception of moderate values in the posterior end of the branchial arches. Here we could however not identify clearly differing tissue morphologies when inspecting the raw image data.

In conclusion, these experiments show that preventing the desensitization of Cxcr4b receptor, in either wild type or scavenger mutant embryos, produces a slight increase in the phenotypic strength of the two already present phenotypes. However, enhanced morphological phenotypes could not be detected in other Cxcr4b expressing tissues.

3.5 Testing the role of desensitization in providing phenotypic robustness

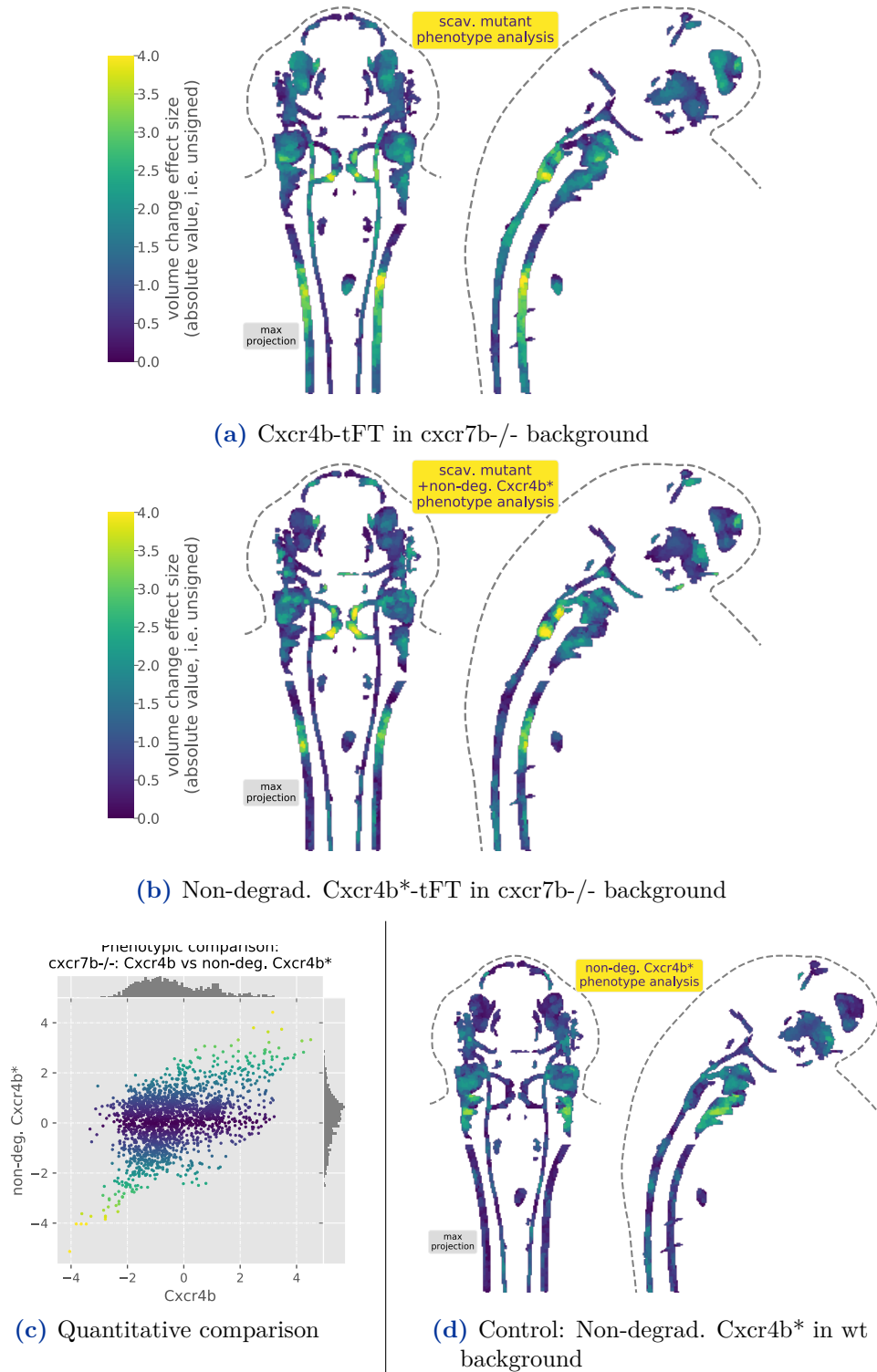


Figure 3.15 – Morphological phenotype analyses: Side-to-side comparison between *Cxcr4b*-tFT and *Cxcr4b*^{*}-tFT in *cxcr7b*^{-/-}.

Data includes a total of $N_{cxcr4b-tFT} = 23$, $N_{cxcr4b^*-tFT} = 17$, $N_{cxcr4b-tFT,cxcr7b^{-/-}} = 27$ and $N_{cxcr4b^*-tFT,cxcr7b^{-/-}} = 31$ processed samples.

3.6 Materials and Methods

3.6.1 Zebrafish stocks

Fish maintenance

Zebrafish (*Danio rerio*) strains were maintained and staged following standard procedures. Embryos were raised in E3 buffer at 30°C. All zebrafish experiments were conducted under the rules of the European Molecular Biology Laboratory and the guidelines of the European Commission, Directive 2010/63/EU.

Transgenic lines

The following previously described fish lines were used for this study:

- *cxcr4b::cxcr4b-tFT* (BAC) [40]
- *cxcl12at30516* (*cxcl12a-*) [156]
- *cxcr7sa16* (*cxcr7b-*) [68]
- *cxcl12bmu100* (*cxcl12b-*) [21]

The following lines have been produced by Erika Donà, have not been published yet and will be described elsewhere:

- *cxcr4b::lyn-tFT* (BAC)
- *cxcr4b::cxcr4b*Ser-tFT* (BAC)

Before an experiment, the genotype of *cxcl12*^{-/-} and *cxcr7*^{-/-} mutants was determined based on the primordium migration phenotype, while *cxcl12bmu100* mutants were genotyped as previously described [21]. Genomic DNA from single embryos or fin fragments was extracted using QuickExtract DNA Extraktionslösung 1.0 (Biozym).

Phenotype-guided prediction of *cxcl12b* genotype

While *cxcl12at30516* and *cxcl12bmu100* mutations are both viable in homozygosis, we were not able to raise double homozygous mutants to adulthood when crossing *cxcl12a* / *cxcl12b* double heterozygous mutants. To obtain double homozygous embryos *cxcl12a*^{-/-} / *cxcl12b*^{+/-} and *cxcl12a*^{+/-} / *cxcl12b*^{-/-} fish were therefore crossed and *cxcl12a*^{-/-} embryos sorted based on primordium position at 32 h.p.f.. The primordium was identified thanks to the expression of *Cxcr4b-tFT*, being *cxcr4b:cxcr4b-tFT* transgene carried by one of the parents. Sorted embryos were then divided into two groups based on the strength of their phenotype. Finally, single embryo genotyping was performed to assess the frequency of *cxcl12b*^{-/-} embryos in either of the groups. Note: these experiments were performed by Erika Donà.

Otherwise, crosses of the above mentioned lines were raised at convenience (homozygously viable) to obtain the mixed genotypes indicated in the experiments.

3.6.2 pLLP migration phenotype scoring

Overviews of 48 h.p.f. (or any indicated stage) embryos were acquired using a Leica MZ16F fluorescence stereomicroscope. Distances from the ear to the primordium and from the ear to the tail of the fish were measured using Fiji. Their ratio was then considered as the normalised migrated distance.

3.6.3 Light sheet microscopy

Dechorionated embryos were mounted through glass-capillaries in 1% LMP agarose plus 100 µg/ml Mesab and imaged on a ZEISS Lightsheet Z.1 microscope using a ZEISS x20 / 1.0 water-immersion Plan Apochromat objective lens with 0.6 zoom resulting in a pixel size of 0.64 µm. To increase the effective penetration depth limited by light scattering in the specimen, stacks from four views at 90° angles

turning around the anterior-posterior axis of the embryo were acquired. For a given view, planes were acquired every 3 μm with a field of view of 1400 x 1920 pixels. GFP and RFP were acquired sequentially, switching channel every plane, using varying laser powers and exposure times. Images from dual sided illumination (ZEISS 10x / 0.2) were combined into a single image using the online image fusion option offered by the acquisition software (ZEN). Before further processing, the (constant) background subtracted image stacks were blurred using a gaussian kernel to even out camera pixel noise and artifacts.

4 Discussion

The central aim of this study consisted in studying chemokine signaling activity and function across tissues in the context of early zebrafish development. Specifically, the focus lied on exploring potential interactions of the chemokine receptor Cxcr4b and its scavenger receptor Cxcr7b. While a novel interaction mechanism between the two proteins had recently been discovered in the migrating posterior lateral line primordium, the aim of this study consisted in systematically probing and screening the embryo for further relevant interactions. This strongly explorative question was justified and accompanied by the advent of novel microscopy techniques and improving computational resources for data analysis, which form the basis of the methodological approach chosen in this study. Developing and combining tools for the processing of large microscopy data, a framework for the spatial normalisation of many zebrafish embryo acquisitions was established, incorporating both biological replicates and genetic perturbations of interest. Complementing the use of tandem fluorescent lifetime reporters as a readout for receptor turnover with a quantitative readout for morphological phenotypes, this framework was then applied to probe the impact of Cxcr7b on Cxcr4b signaling activity and function. This section summaries and discusses both the methodological developments and the biological results obtained along the way and provides future perspectives.

4.1 Establishing a multi-view light sheet reconstruction pipeline for increased multi-view throughput and reconstruction quality

Imaging full embryos has in recent years been made possible by the invention of multi-view light sheet microscopy [82, 153], which has emerged as a powerful method to obtain fluorescence recordings of entire developing organisms *in vivo*. While this has allowed addressing many new questions bridging the cellular to the tissue and embryo scale, many technical difficulties remain in terms of processing the data produced by the microscopes. In addition to the fact that growing data sizes pose a challenge to available computational resources, the post processing of raw data consisting of registration and fusion of multi-view image stacks has remained a poorly standardised step with unreliable outcomes of varying quality. Aiming to integrate high quantities of multi-view samples of high quality into our analysis, within this thesis we addressed and improved upon two aspects of multi-view image processing.

Robust multi-view registration without fiducial markers

The first aspect addresses multi view registration. So far, the available methods and protocols for finding the affine transformations between multi view stacks had required the use of fiducial markers as references for guiding the registration process [123, 82, 121]. These are either embedded into the acquired sample or imaged separately using the same multi view configuration as used for the sample. Both of these procedures not only complicate the acquisition process but also significantly increase acquisition times due to strongly increased sample volumes, possibly including sample replacement¹. In the case of working with many staged live samples,

¹Another issue is an increase in data sizes, which can be addressed using image compression algorithms specifically designed for large fluorescence microscopy images. Although not detailed in this thesis, the author has collaborated on the development of such algorithms [10].

4.1 Establishing a multi-view light sheet reconstruction pipeline for increased multi-view throughput and reconstruction quality

timing can however be critical. Therefore, we developed a method to register image stacks in the absence of fiducial markers. As detailed in sec. 2.1.1, this was achieved by performing registration in three steps of increasing transformation complexity. As a first step, stacks were rotated according to microscope metadata and an initial translation between pairs of stacks was found by performing a 3D Fourier phase shift registration. The robustness of this first step significantly increased by applying 3D adaptive contrast enhancement (CLAHE) to the input image stacks prior to calculating the cross spectral densities. As a second step, an affine transformation between pairwise stacks was found by optimising an image similarity metric. As a last step, this process was repeated in a groupwise registration of all multi view stacks, further increasing the robustness and precision of the final registration result.

Towards reaching the overall goal of this thesis and to acquire many in toto acquisitions it was key to rely on a robust registration algorithm. Also, by eliminating the need for acquiring fiducial markers together with the sample, we decreased the acquisition times of individual sample snapshots approx. two fold, significantly increasing the throughput when imaging living samples, reaching between 20-30 in toto samples in 2-3 hours. Further, our improvements in multi view registration have shown to work robustly not only in the context of this work, but also for various other (to this point partly unpublished) datasets including reconstructions of mouse [42] and drosophila embryos using a variety of different markers in living and fixed specimens. Additional benefits of performing registration based directly on image data include the possibility of partially correcting for distortions introduced by scattering in large samples and the option of restricting high resolution views to a region of interest lying entirely within the specimen. In terms of limitations, in its current form the described registration method assumes the multiple views to be acquired in a linear succession of pairwise overlaps. Also, should a pairwise registration fail, alternative registration strategies need to be introduced manually. For further increasing the generality and robustness of the method, it might be beneficial to include a heuristic to perform redundant registrations between views and

use a quality metric to prioritise reliable transformations. A similar method has recently been implemented in the context of stitching tiled stacks of large cleared samples [57].

Image quality weighted multi-view deconvolution

Besides their use for registration, fluorescent beads embedded into the sample can be used for directly measuring the PSF within the imaged stack. The extracted PSFs can then be used for multi-view deconvolution in the fusion step [121]. Although beads can estimate a spatially varying PSF [148], these measurements are not performed within the specimen, where in the case of large scattering samples the superficial (or theoretical) PSF is strongly degraded.

The second aspect of multi-view processing addressed within this thesis therefore concerns multi view deconvolution in highly scattering samples. By combining the most common Lucy-Richardson based multi-view deconvolution approach [80] with an image quality based weighting scheme, a final fusion of superior quality was achieved. Specifically, each position in each of the multiple views was assigned a relative weight value reflecting its local image quality as determined by the entropy of a spectral image quality measure. This weight value would then determine the relative contribution of its associated pixel to the final multi view reconstruction. By comparing different fusion approaches we showed that this method successfully enhances reconstruction quality in panoramic zebrafish embryo acquisitions.

While image quality based multi view weighting has been used in additive fusion schemes [122][123], to our knowledge it had so far not been applied to multi-view deconvolution. However, in this context a weighting scheme is particularly useful, as although most deconvolution algorithms assume an accurate PSF, the latter is difficult to estimate deep within a sample. Therefore, weighing the contributions of the individual locations to the final reconstruction in the different views mitigates this problem and produces quantitatively more reliable results. Other approaches

4.1 Establishing a multi-view light sheet reconstruction pipeline for increased multi-view throughput and reconstruction quality

based on sample geometry could be used to determine regions of good quality within a given stack, however in contrast to an image quality metric these rely on extracting geometrical features of the sample, which is difficult to perform in a robust manner for the general case. In terms of computational performance, while computing the image quality weights represents additional processing time, it can also significantly reduce the time required for the subsequent multi view deconvolution step, which is the most time consuming. This could be achieved by using the quality weights to reduce the image volume to be convolved, e.g. by excluding minimally contributing regions using a threshold.

Within this work, all multi-view deconvolutions have been performed approximating the PSF by gaussian convolution kernels. In an iterative process, their widths in xy and z was manually determined for a given microscope settings optimizing the visual quality of the final reconstruction output and avoiding the formation of visible ringing artifacts. While a theoretical estimate of the PSF or a direct measurement using fluorescent beads could have been obtained, these likely would have only represented a better estimate of the PSF near the surface of the sample. Importantly, as within this work we rely on interpreting image intensities in a quantitative manner, as a control we compared pooled absolute intensities and ratiometric values (as quantified by the tissue patches) between different multi-view reconstruction methods and found no significant differences. This is likely explained by our conservative choice of regularization, the fact that the same spatially invariant convolution kernel was used for all experiments and that quantitative intensity based comparisons were only performed between samples acquired in the same experimental same session with unchanged microscope alignments.

Possible improvements of current multi-view reconstruction methods fall into two categories: Improving reconstruction quality on one hand and reducing processing time on the other. For the first goal, deconvolution based methods would strongly benefit from accurate estimations of the effective PSF within the sample. A promising emerging approach lies in the detailed simulation of the imaging process [163],

rendering the problem more computationally tractable. Also, potentially the simultaneous observation of the same region of interest from different views can further be exploited by incorporating appropriate priors into probabilistic reconstruction methods. Secondly, both the efficient use of GPUs and optimizations of convergence behavior can reduce processing times of multi-view reconstruction [121]. Finally, an approach addressing both categories are convolutional neural networks, which have been shown to perform well on image restoration tasks[162] and could be expanded to the multi-view context.

4.2 Building an *in toto* atlas to integrate expression, signaling and phenotype information

While previous studies addressing chemokine signaling interactions focussed on specific tissues, here we aimed to systematically study the embryo. Having established the multi-view processing methods to image many zebrafish embryos *in toto*, the next challenge consisted in extracting information from the highly heterogeneous data obtained from microscopy. Considering the high developmental variability of the zebrafish embryo and the need to analyse mutant embryos potentially exhibiting strong phenotypes, a simple side to side comparison between embryos would have not allowed detailed comparisons. Therefore, the methodology of choice was to spatially normalise the embryo stacks and define a common coordinate system, into which all samples would be placed under nonlinear transformations. In recent years, advances in the accuracy of nonlinear image registration methods had significantly improved, strongly driven by research in neurodevelopmental disorders in the human brain[76]. Building upon this, brain registration had recently also been successfully applied to the developing zebrafish brain[131, 101, 84].

Within this thesis we optimised nonlinear image registration to process full panoramic recordings of the zebrafish embryo at 36hpf. Using fluorescent labelling

4.2 Building an in toto atlas to integrate expression, signaling and phenotype information

of our protein of interest (*cxcr4b:cxcr4b-sfGFP*), as a reference marker we optimised nonlinear image registration to align in toto zebrafish recordings with an isotropic resolution of $3\mu m$. Combining registration with adaptive contrast enhancement allowed this process to be robust even to strong phenotypic differences between samples. Performing iterative pairwise image registration between each sample and a set of samples defined as the reference dataset, we established a framework which would reliably place any new sample into a common coordinate system defined by the reference dataset. Manually placing landmarks on wild type and mutant samples we determined the achieved final resolution to be approx. $10\mu m$, which roughly corresponds to the diameter of an average cell. Further, to quantify the expression levels of the reference marker or markers acquired in adjacent channels, such as the slow maturing tagRFP within the fluorescent timer construct, we performed a segmentation of all Cxcr4b expressing structures in the embryo. The resulting volume of interest was then further clustered into tissue patches of an average diameter of $10\mu m$, defining the units for quantitative comparison between samples.

Quantifying fluorescence intensities allows the comparison of expression levels and lifetime ratios between samples, which can inform about differences in gene regulation or protein dynamics within and between genetic conditions. While being able to compare these measurements between samples is enabled by spatial normalisation, possible differences in morphology are normalised out. In order to additionally quantify morphological differences, we analyzed the deformation fields characterising the transformation of a given sample into the common coordinate system. Focusing on a simple scalar measure of 3D vector fields, we used the jacobian determinant of the displacements to indicate volume changes between samples. This is a common measurement performed in MRI studies to assess sizes of human brain regions and in our context provided a valuable readout for morphological phenotypes in the embryo, which could be quantified next to image intensities and ratios for every tissue patch. To see whether measured volume changes reported on actual phenotypes, the approach was validated by successfully identifying naturally occurring

left-right asymmetries in wild type embryos. Complementing intensimetric readouts providing information about expression and protein dynamics (using tandem lifetime reporters) with a morphological analysis therefore resulted in a method to link chemokine expression, activity and function systematically within the developing embryo.

Important to note is that existing studies performing nonlinear image registration of images obtained from fluorescence microscopy typically use reference markers which are ubiquitously expressed, e.g. expressing fluorophores using pan-neuronal or beta-actin promoters[131, 84]. In these cases, other labels of interest are integrated into the respective template by being acquired in a second channel next to the reference marker. Instead, in our case the fluorescent labelling of the receptor of interest *Cxcr4b* was used directly as a reference for the registrations. This was necessary as the fluorescent timer was occupying the green and red channels, leaving only a blue channel if significant bleed through was to be avoided. Also, DAPI stainings of the embryos introduced fixing artefacts and did not allow to resolve structures deep within the sample, both in terms of staining penetrance and increased optical scattering at lower wavelengths. Using *cxcr4b:cxcr4b-sfGFP* as a reference label had the disadvantage that differences in its expression between embryos or more importantly genetic conditions could interfere with the normalisation process itself (see section 3.4). On the other hand, using a specific label highlights the structure of interest better than a ubiquitous label would, therefore potentially increasing registration accuracy in these regions. Using either labelling strategy it is important to keep in mind that, strictly speaking, inter-sample registration produces mappings between expression domains rather than anatomical structures. In our study, we did not observe a clear change in expression domains between samples and image registration has proven to be relatively stable with respect to fluorophore intensity variations.

In general, labelling should be most critical for the morphological readouts. For the future, using membrane anchored fluorophores might prevent differences in la-

bellings intensities. Because the lifetime reporter relies on receptor degradation, different datasets would need to be acquired to obtain lifetime ratios and morphological phenotypes, independently contributing information to the atlas framework. In preliminary experiments, using a *cxcr4b:cxcr4b-lyn-sfGFP-tagRFP* construct has shown to provide a more homogeneous labelling of Cxcr4b expressing structures and exhibited relatively constant intensities between wild type and scavenger mutants. Slightly different and some additional structures were labelled compared to the unchanged timer construct, the latter representing tissues which in wild type had lost Cxcr4b expression but were still expressing due to the membrane anchoring. Possibly, the observed increased labelling consistency could reduce the relatively high spread of morphological readouts presented in section 3.4. This way, a more refined phenotypic analysis would be possible. For example, in addition to volume changes the precise shape changes between tissues could be quantified. This is exemplified in fig. 4.1, where the expression of the membrane anchored Cxcr4b label is shown together with an analysis of morphological changes between wild type datasets.

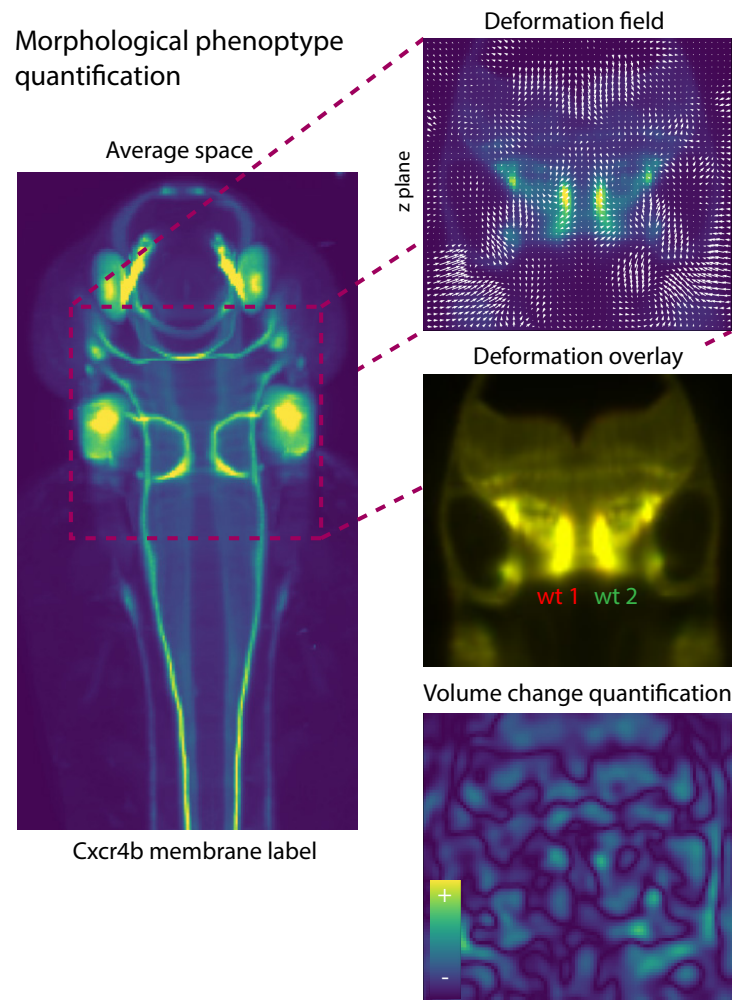


Figure 4.1 – Morphological phenotyping: Different labelling strategies could further improve morphological readouts, leading to refined descriptions of shape changes between samples and genetic conditions. Here, subtle morphological differences between wild type samples expressing a membrane anchored label are quantified as an example.

4.3 Loss of scavenger leads to embryo-wide hyper activation of chemokine signaling

In recent years, tandem fluorescent lifetime reporters had emerged as a tool for estimating average protein ages in living cells. Moreover, Donà et al. had recently shown that tFT could be used to visualize Cxcr4b receptor turnover in the zebrafish pLLP *in vivo*. Due to its ability to readout dynamic properties of receptors in snapshot recordings, the timer represented an ideal tool to investigate signaling activity in the context of the entire embryo. Namely, in combination with the spatial normalisation of embryos, tFT ratios could be directly compared between different genetic conditions in all segmented tissues. A difference in ratios and therefore average receptor age at a given location in the embryo would indicate that the dynamic history of that pool of Cxcr4b receptors would have been affected by the analyzed genetic perturbation.

First, we analyzed receptor populations in knockout mutants for the shared ligands of Cxcr4b and Cxcr7b. Compared to the wild type, we found that the large majority of tissues exhibited pools of receptors that were older in the absence of ligands. Additionally, an increase in receptor concentrations correlated with the increase in age. These findings were expected and confirm that tissues expressing Cxcr4b are sensitive to Cxcl12 and that this sensitivity can be captured by a tFT readout.

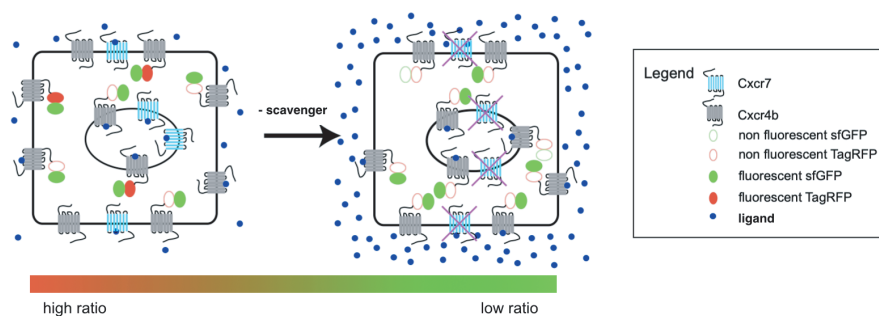


Figure 4.2 – Schematic of the signaling effect of scavenger loss at the cellular scale

Interested in possible interactions between Cxcr4b and Cxcr7b, in the same way we analyzed the behavior of receptor populations in the absence of the scavenger. Fig. 4.2 illustrates the expected effect of the scavenger on the ratio readout. Interestingly, we found an embryo-wide decrease in ratios, i.e. younger receptors in the mutant. Statistical analysis showed that 63% of all segmented tissues exhibited a significant decrease in receptor ages. Comparing receptor levels between the two conditions revealed a clear correlation between the change of receptor population age and a change in receptor levels: This was consistent with the scenario that the scavenger massively increased the degradation and turnover of Cxcr4b within the embryo.

In addition to spatially mapping the affected tissues, performing timer analysis within the spatial normalisation framework allowed orthogonal experiments and measurements to be compared to each other. Interestingly, we observed that some tissues did not show sensitivity to the absence of ligand, while they did show a ratio decrease when taking away the scavenger. This suggests that tissues exist from which the ligand is entirely shielded off by the scavenger, indicating that the scavenger can indeed strongly shape the signaling environment, with an impact of comparable importance to that of the ligand itself.

Importantly, interpreting changes in receptor turnover at a global scale between genetic conditions is only made possible by performing a mapping establishing direct correspondences between tissues in the different conditions. An alternative way of measuring lifetime ratios would be to use fluorescence activated cell scanning (FACS) in combination with protocols to dissociate the embryo. While in this way a higher throughput of embryos could be studied, changes in receptor levels or lifetime ratios could only be measured at the population level. Given the complexity of the dynamic tFT readout, clear conclusions can hardly be drawn without comparing sufficiently small and homogeneous receptor populations that can be assumed to respond approx. uniformly to a given perturbation. Otherwise, effects might be averaged out or, more importantly, as generally receptor populations cannot be assumed to be in steady state, necessary assumptions for interpreting ratio changes

could not be verified. However, FACS could be useful for rapidly spotting global candidate interactions reported by the ratios, to then be further examined and interpreted by a spatial analysis.

4.4 Desensitization alone cannot explain morphological robustness to increased signaling in *cxcr7b*^{-/-}

Most tissues are aphenotypic in *cxcr7b*^{-/-}

In the absence of the scavenger, we found that Cxcr4b expressing tissues all across the embryo exhibited an increased turnover. To see whether this hyper activation of signaling was accompanied by a phenotypic output, we mapped phenotypic scores onto the embryo and these tissues in particular. Interestingly, a morphological phenotype could be detected in the lateral line, where primordium migration had been arrested in the scavenger mutant. A second phenotype came up in the facial motor neurons, which exhibited differently shaped accumulation of neurons, often disconnected from the lateral nerves they connect to in wild type. Confirming our observation, this phenotype had already been described in the literature [32].

Interestingly in mice, Cxcr7 deficiency is lethal in early postnatal stages. The underlying phenotypes are associated to cardiovascular development and characterised by a bulky and less branched vasculature compared to wild type [170, 140, 47]. In these processes, Cxcr7 is also described to interact with the Cxcr4/Cxcl12 signaling axis. In zebrafish, cardiovascular defects in the absence of Cxcr7b have recently also been described [151]. In zebrafish however cardiovascularity is driven by Cxcr4a, which is the gene duplicate of our targeted receptor Cxcr4b [55]. In our data, part of the vasculature appears faintly labelled by Cxcr4b, which however provided a too low signal to be included into the set of segmented tissues. However, interestingly, the volume changes obtained from the deformation map analysis are independent of the

segmentation and captured varying morphologies in some of the cardiovascular, which could be confirmed when looking into the raw unregistered image stacks (data not shown).

Interestingly, the lateral line and the facial motor neurons remained the only morphological phenotypes we identified in *Cxcr4b* expressing tissue at 36hpf. Many other structures such as the branchial arches, the olfactory bulbs and other neurons showed no morphological differences. The lack of more phenotypes in the absence of *Cxcr7b* is not necessarily surprising, as in zebrafish also the scavenger is present in duplicates in the form of *Cxcr7a* and *Cxcr7b*. Therefore, an upregulation of *Cxcr7a*, which shares the same ligands (REF?), could buffer phenotypic effects. While this might be the case, our lifetime ratio analysis showed that the signaling activity of *Cxcr4b* was indeed altered due to the absence *Cxcr7b*. Therefore, if present, a possible epistatic effect does not maintain chemokine levels in the embryo. Instead, we see that *Cxcr4b* activity increases strongly despite the presence of *Cxcr7a*, providing evidence for a clear phenotypic effect of the *Cxcr7b* mutant, which is however predominantly restricted to a signaling layer, without exhibiting an impact in terms of tissue morphologies at 36hpf.

Probing the role of desensitization by preventing *Cxcr4b* degradation

While we found that overall *Cxcr4b* receptor turnover rates were increased, we also found that this was accompanied by and correlating with a strong difference in receptor levels. Consistent with an increased degradation as a consequence of increased turnover, *Cxcr4b* was present in significantly lower concentrations in the mutant compared to the wild type (less than half in most tissues). Could it be that this desensitization effect prevented further phenotypes? As a result of the chemokine flood in the absence of scavenger, receptors were turning over at higher rates, however in lower concentrations. Therefore, net downstream signal transduction could possibly

4.4 Desensitization alone cannot explain morphological robustness to increased signaling in *cxcr7b*^{-/-}

be maintained at similar levels. Indeed, desensitization in response to ligand is a shared feature of G protein-coupled receptors[95] and is considered important for cell gradient sensing [92][119]. Specific to Cxcr4, the inability of the receptor to desensitize is known to lead to excessive signaling responses by immune cells in the context of the WHIM syndrome [7].

We reasoned that the optimal experiment to test whether desensitization was indeed providing robustness in these tissues would be to prevent degradation and assess the resulting phenotypes. Indeed this was possible by using a genetically engineered version of the signaling receptor, Cxcr4*, in which a truncation of the serine residues within the C-tail prevented receptor ubiquitination, therefore hindering Cxcr4 from being degraded (see fig. 4.3 for a schematic). This could be used for comparing the effects of the wild type and degradation deficient Cxcr4b in the absence of the scavenger: the desensitization hypothesis would be confirmed if the phenotypes strengthened without desensitization.

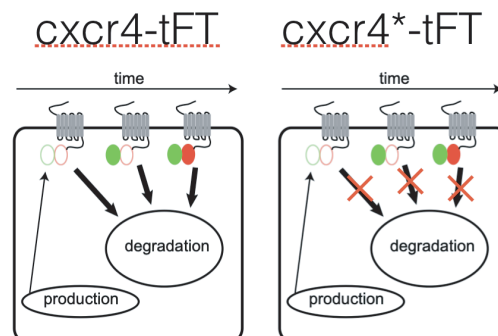


Figure 4.3 – We probed the role of desensitization in response scavenger absence by comparing the phenotypes of Cxcr4b and its non degradable modification Cxcr4*.

Assessing the effect of Cxcr4* in the context of pLLP migration, we found that indeed there was an increase in phenotypic strength. However, also Cxcr4b* alone in a wild type background showed a slightly reduced total migration distance. Therefore, this allows two different interpretations, namely that the tissue shows

1. an additive phenotype of the two independent perturbations or

2. a stronger effect resulting from a higher order interplay between the two perturbations.

In both cases, a lack of desensitization might explain the observed phenotypes, however only in the second could we conclude that desensitization specifically ameliorates the phenotypic impact of the absence of the scavenger. Therefore, we interpret that the results of this assay in the lateral line neither confirm nor falsify the hypothesis that desensitization plays a stabilizing role in the case of overabundant ligand availability.

To see how this behaved in other tissues we assessed the effect of Cxcr4* in all segmented structures using our morphological phenotype analysis. Here, we found that preventing Cxcr4b from degrading

1. produces a slight increase in the phenotypic strength of the two *cxcr7b*^{-/-} phenotypes and
2. does not introduce any additional morphological phenotypes and

Therefore, we conclude that while receptor desensitization seems to play some role, as it slightly increases *cxcr7b*^{-/-} phenotypes, in most Cxcr4b expressing tissues it does not explain the absence of phenotypes in terms of tissue morphologies. Interestingly, the ligand sinking role of Cxcr7 has also been proposed to have the function of keeping Cxcr4 levels high [1]. While we can confirm that receptor levels decrease all across the embryo in the absence of the scavenger, conversely this loss of signaling receptor does not lead to phenotypes when compared to the case of persistently high receptor levels.

4.5 An opportunity to model receptor interactions

In section 3.3.2 we compared the obtained decreases of lifetime ratios in the scavenger mutant to the expression pattern of the latter. Expecting a relationship between

these quantities, we were surprised to find that there was only a weak correlation between the two, indicating that the presence of Cxcr7b does not clearly predict its signaling impact on Cxcr4b. Interestingly, also the global distributions of Cxcr4b and Cxcr7b were largely non overlapping within the embryo. While this could reflect non overlapping functions of the two receptors at this stage of development, there is also the possibility that the receptors interact over a distance. This could be mediated by a diffusive ligand which is attracted by its sinks. In fact, when artificially dilating the measured Cxcr7b expression pattern, which would simulate the diffusion of the scavenger or in its effect the ligand, the correlation slightly improved. A number of reasons could explain both this increase and the generally low correlation, including that

- ratio differences between wild type and scavenger mutant are not necessarily proportional to changes in ligand concentrations
- differing geometrical conditions within the embryo lead to locally differing relationships between sink and ligand concentrations
- the two receptors can interact at distance due to ligand diffusion.

Potentially, exploiting the timer in a more quantitative way could lead to more clarity. While it is difficult to visualise endogenous ligand concentrations directly, from tFT measurements in steady state degradation rates can be inferred, which are directly linked to ligand concentrations [40]. Although in the general case steady state cannot be assumed, estimates of degradation constants could be obtained. For example, acquiring several, potentially only two timepoints instead of a single snapshot of the tFT expressing embryo would allow estimating the degradation constant for every tissue. In this way, potential large range effects could be uncovered in quantitative models. Also, the contribution of different components to the formation of chemokine gradients could be studied and validated in detail. Even without following ratios over time, combining perturbations of signaling components with the spatial normalisation framework provides an opportunity for testing inter-

actions within the dynamic environment of the developing embryo *in vivo*. Any variation in the ratio differences between pairs of conditions hints towards a change in the underlying interactions. In this way, the signaling impact of even peripheral components could be assessed.

4.6 Future perspective

As previously mentioned, our spatial normalisation framework in combination with tandem fluorescent lifetime reporters is especially well suited to model and uncover interactions between signaling components. An interesting application would be to further study genetical variability and robustness of signaling networks. The zebrafish genome is characterised by a remarkable abundance of gene duplications [94], which constitute one of the main drivers of vertebrate genome evolution. An analysis of the functional interactions between gene duplicates could both provide an entry point to studying the high natural variability in phenotypic traits during zebrafish development and elucidate the continuous process of functional diversification of these components.

When using timers to study signaling dynamics, one of the main sources of uncertainty in terms of interpreting its readout consists of the fact that the timer reports on the cumulative signaling history of the receptor population of a given cell or tissue [69]. This complicates the direct comparison between genetic conditions. One solution to address this would be to track the timer signal over time, which so far has been limited by quickly bleaching fluorophores. However, combining gentler light sheet microscopy with new fluorescent proteins might overcome this issue. Being able to obtain time resolved tFT readouts would allow the precise quantification of protein dynamics in terms of production and degradation rates [13].

Another way of obtaining a more precise signaling readout would be to perform more acute perturbations of the system. This could e.g. involve heat-shock experiments or

other inducible genetic systems to modify the availability of a certain component in a targeted manner. Of course, the continuously increased availability of optogenetic perturbations in all model organisms is a promising method for precise perturbations in both space and time.

Further, measurements and perturbations over time could be complemented by non-linear image registration performed not only between samples but also between time-points, yielding four dimensional tensors of tissue dynamics. An interesting field of application would be the study of morphogenetic processes, where a deformation field analysis could complement the use of novel intensiometric activity readouts [137, 74] and perturbation strategies [63] to quantify the feedback between mechanics, signaling and phenotypic function across different spatial and temporal scales.

4.7 Concluding remarks

In this thesis, we developed a computational framework for the comprehensive quantification of both fluorescent readouts and tissue morphologies from multi-view light sheet microscopy acquisitions. Combining this framework with the use of a novel reporter for measuring receptor activity in vivo, we took a systemic approach to studying chemokine signaling in the embryo. By being able to quantify and directly compare embryo wide activity measurements between different genetic conditions, we mapped the systemic reactions of the embryo's signaling state to the absence of different functional components of the signaling network. Further we used precise genetic perturbations together with the ability of our analysis framework to integrate information about expression, signaling dynamics and phenotypes to study mechanisms underlying genetic robustness. Together, we hope to have provided proof of principle evidence in showing that modern microscopy and image processing can be combined with novel cell biological assays to systematically study embryonic development.

Acknowledgements

At this point I want to express my sincere gratitude to Darren Gilmour, who from starting off as a collaborator became my scientific advisor. It is his mentorship characterised by knowledgeable scientific guidance, enthusiasm, encouragement and patience, adaptability, respectfulness and tireless support which has been a privilege for me and is highly appreciated.

Importantly, I would like to thank Francesca Peri for the opportunity to start my PhD in her lab and her generous investments and active part in my pursuance of diverse projects. For introducing me into the world of zebrafish and her good advice, kindness and strong support during these years.

I thank Detlev Arendt, Thomas Höfer and Lars Hufnagel for acting as members of my scientific advisory committee and Steffen Lemke for agreeing to chair the Defense. Also, I especially thank Detlev and Thomas for reviewing this thesis.

I would like to especially thank Lars Hufnagel for rewarding collaborations, sharing of knowledge and continuous support over the years.

Next, I would like to thank Erika Donà for the conceptualization of this project and her contributions to it. Also for a great learning experience during the beginning of my PhD.

I'd like to thank all overlapping people around the Peri and Gilmour labs at both EMBL and UZH for creating such a collaborative, esteeming and fun environment. A special thanks goes to many people (Elisa, Katrin, Ale, Ambra, Sabine,...) and especially Jonas Hartmann for his great company and interesting discussions.

From Hufnagel lab special thanks goes to Gustavo, Nils, Balint, Lucia, Ulla, Dimitri and Masternils for collaborations, activities and fun.

Further, I'd like to thank the entire Developmental Biology Unit at EMBL for a vibrant, constructive and curiosity driven environment. This thanks extends to different groups of people for their ways of making EMBL such a great place to work at: the Cantine and Cafeteria, IT Services, Kitchen Ladies, Staff Association, Graduate Office, ALMF, and many more.

Personally, I am grateful to many dear friends for making my PhD time at EMBL so enjoyable: Thibaut, Gustavo, Aastha, Lukas, Thibaut, Lucía, Sourabh, Sascha, Joergen, Natalia, Deepika, Jessica, Maria, Jonas, Jan, Ulla, Manu, Masternils, Nils, and many more. Thank you Naomi for so much.

Finally, I'd like to thank my parents and brothers for the support of a loving family.

Bibliography

- [1] Philipp Abe, Wiebke Mueller, Dagmar Schütz, Fabienne MacKay, Marcus Thelen, Penglie Zhang, and Ralf Stumm. CXCR7 prevents excessive CXCL12-mediated downregulation of CXCR4 in migrating cortical interneurons. *Development*, 141(9):1857–1863, may 2014.
- [2] Markus Affolter and Cornelis J. Weijer. Signaling to cytoskeletal dynamics during chemotaxis, 2005.
- [3] John Ashburner and Karl J. Friston. Voxel-Based Morphometry: The Methods. *NeuroImage*, 11(6):805–821, jun 2000.
- [4] B AVANTS, C EPSTEIN, M GROSSMAN, and J GEE. Symmetric diffeomorphic image registration with cross-correlation: Evaluating automated labeling of elderly and neurodegenerative brain. *Medical Image Analysis*, 12(1):26–41, feb 2008.
- [5] Brian B. Avants, Paul Yushkevich, John Pluta, David Minkoff, Marc Korczykowski, John Detre, and James C. Gee. The optimal template effect in hippocampus studies of diseased populations. *NeuroImage*, 2010.
- [6] Gyeong Hun Baeg, Erica M. Selva, Robyn M. Goodman, Ramanuj Dasgupta, and Norbert Perrimon. The Wingless morphogen gradient is established by the cooperative action of Frizzled and Heparan Sulfate Proteoglycan receptors. *Developmental Biology*, 2004.
- [7] K. Balabanian, Bernard Lagane, José Luis Pablos, Lysiane Laurent, Thierry Planchenault, Olivier Verola, Celeste Lebbe, Delphine Kerob, Alain Dupuy,

- Olivier Hermine, Jean-François Nicolas, Véronique Latger-Cannard, Danièle Bensoussan, Pierre Bordigoni, Françoise Baleux, Françoise Le Deist, Jean-Louis Virelizier, Fernando Arenzana-Seisdedos, and Françoise Bachelerie. WHIM syndromes with different genetic anomalies are accounted for by impaired CXCR4 desensitization to CXCL12. *Blood*, 105(6):2449–2457, mar 2005.
- [8] Karl Balabanian, Bernard Lagane, Simona Infantino, Ken Y.C. Chow, Julie Harriague, Barbara Moepps, Fernando Arenzana-Seisdedos, Marcus Thelen, and Françoise Bachelerie. The chemokine SDF-1/CXCL12 binds to and signals through the orphan receptor RDC1 in T lymphocytes. *Journal of Biological Chemistry*, 2005.
- [9] Karl Balabanian, Bernard Lagane, José Luis Pablos, Lysiane Laurent, Thierry Planchenault, Olivier Verola, Celeste Lebbe, Delphine Kerob, Alain Dupuy, Olivier Hermine, Jean François Nicolas, Véronique Latger-Cannard, Danièle Bensoussan, Pierre Bordigoni, Françoise Baleux, Françoise Le Deist, Jean Louis Virelizier, Fernando Arenzana-Seisdedos, and Françoise Bachelerie. WHIM syndromes with different genetic anomalies are accounted for by impaired CXCR4 desensitization to CXCL12. *Blood*, 2005.
- [10] Bálint Balázs, Joran Deschamps, Marvin Albert, Jonas Ries, and Lars Hufnagel. A real-time compression library for microscopy images. *bioRxiv*, page 164624, jul 2017.
- [11] Tamas Balla. Green light to illuminate signal transduction events, 2009.
- [12] S. C. Baraban, M. R. Taylor, P. A. Castro, and H. Baier. Pentylenetetrazole induced changes in zebrafish behavior, neural activity and c-fos expression. *Neuroscience*, 2005.
- [13] Joseph D Barry, Erika Donà, Darren Gilmour, and Wolfgang Huber. TimerQuant: a modelling approach to tandem fluorescent timer design and

- data interpretation for measuring protein turnover in embryos. *Development (Cambridge, England)*, 143(1):174–9, jan 2016.
- [14] Deepali Bhandari, Joann Trejo, Jeffrey L. Benovic, and Adriano Marchese. Arrestin-2 interacts with the ubiquitin-protein isopeptide ligase atrophin-interacting protein 4 and mediates endosomal sorting of the chemokine receptor CXCR4. *Journal of Biological Chemistry*, 2007.
- [15] Bijan Boldajipour, Maria Doitsidou, Katsiaryna Tarbashevich, Cedric Laguri, Shuizi Rachel Yu, Jonas Ries, Karin Dumstrei, Sylvia Thelen, Julia Dörries, Esther Maria Messerschmidt, Marcus Thelen, Petra Schwille, Michael Brand, Hugues Lortat-Jacob, and Erez Raz. Cxcl12 evolution - subfunctionalization of a ligand through altered interaction with the chemokine receptor. *Development*, 2011.
- [16] Bijan Boldajipour, Harsha Mahabaleshwar, Elena Kardash, Michal Reichman-Fried, Heiko Blaser, Sofia Minina, Duncan Wilson, Qiling Xu, and Erez Raz. Control of Chemokine-Guided Cell Migration by Ligand Sequestration. *Cell*, 2008.
- [17] Bijan Boldajipour, Harsha Mahabaleshwar, Elena Kardash, Michal Reichman-Fried, Heiko Blaser, Sofia Minina, Duncan Wilson, Qiling Xu, and Erez Raz. Control of Chemokine-Guided Cell Migration by Ligand Sequestration. *Cell*, 132(3):463–473, feb 2008.
- [18] Jennifer M. Burns, Bretton C. Summers, Yu Wang, Anita Melikian, Rob Berahovich, Zhenhua Miao, Mark E.T. Penfold, Mary Jean Sunshine, Dan R. Littman, Calvin J. Kuo, Kevin Wei, Brian E. McMaster, Kim Wright, Maureen C. Howard, and Thomas J. Schall. A novel chemokine receptor for SDF-1 and I-TAC involved in cell survival, cell adhesion, and tumor development. *Journal of Experimental Medicine*, 2006.
- [19] John M. Busillo and Jeffrey L. Benovic. Regulation of CXCR4 signaling, 2007.

-
- [20] Jeroen Bussmann and Erez Raz. Chemokine guided cell migration and motility in zebrafish development. *The EMBO Journal*, 34:1309–1318, 2015.
- [21] Jeroen Bussmann, Scot A. Wolfe, and Arndt F. Siekmann. Arterial-venous network formation during brain vascularization involves hemodynamic regulation of chemokine signaling. *Development*, 2011.
- [22] Joan Castells-Ballester, Ewa Zatorska, Matthias Meurer, Patrick Neubert, Anke Metschies, Michael Knop, and Sabine Strahl. Monitoring Protein Dynamics in Protein O-Mannosyltransferase Mutants In Vivo by Tandem Fluorescent Protein Timers. *Molecules*, 23(10):2622, oct 2018.
- [23] Young Ryun Cha, Misato Fujita, Matthew Butler, Sumio Isogai, Eva Kochhan, Arndt F. Siekmann, and Brant M. Weinstein. Chemokine Signaling Directs Trunk Lymphatic Network Formation along the Preexisting Blood Vasculature. *Developmental Cell*, 2012.
- [24] M Chalfie, Y Tu, G Euskirchen, W W Ward, and D C Prasher. Green fluorescent protein as a marker for gene expression. *Science (New York, N.Y.)*, 263(5148):802–5, feb 1994.
- [25] Mao Rong Chen, Song Yang, Wei Pin Niu, Zhao Yu Li, Ling Feng Meng, and Zheng Xing Wu. A novel fluorescent timer based on bicistronic expression strategy in *Caenorhabditis elegans*. *Biochemical and Biophysical Research Communications*, 2010.
- [26] Ann-Shyn Chiang, Chih-Yung Lin, Chao-Chun Chuang, Hsiu-Ming Chang, Chang-Huain Hsieh, Chang-Wei Yeh, Chi-Tin Shih, Jian-Jheng Wu, Guo-Tzau Wang, Yung-Chang Chen, Cheng-Chi Wu, Guan-Yu Chen, Yu-Tai Ching, Ping-Chang Lee, Chih-Yang Lin, Hui-Hao Lin, Chia-Chou Wu, Hao-Wei Hsu, Yun-Ann Huang, Jing-Yi Chen, Hsin-Jung Chiang, Chun-Fang Lu, Ru-Fen Ni, Chao-Yuan Yeh, and Jenn-Kang Hwang. Three-Dimensional Reconstruction of Brain-wide Wiring Networks in *Drosophila* at Single-Cell Resolution. *Current Biology*, 21(1):1–11, jan 2011.

- [27] Shang Wei Chong, Alexander Emelyanov, Zhiyuan Gong, and Vladimir Korzh. Expression pattern of two zebrafish genes, *cxcr4a* and *cxcr4b*. *Mechanisms of Development*, 2001.
- [28] Shang Wei Chong, Le Minh Nguyet, Yun Jin Jiang, and Vladimir Korzh. The chemokine Sdf-1 and its receptor Cxcr4 are required for formation of muscle in zebrafish. *BMC Developmental Biology*, 2007.
- [29] Albert H. Coons. INTRODUCTION: THE DEVELOPMENT OF IMMUNO-HISTOCHEMISTRY. *Annals of the New York Academy of Sciences*, 177(1 Defined Immun):5–9, jun 1971.
- [30] Francis Crick. Diffusion in embryogenesis. *Nature*, 1970.
- [31] Nicolas Cubedo, Emmanuel Cerdan, Dora Sapede, and Mireille Rossel. CXCR4 and CXCR7 cooperate during tangential migration of facial motoneurons. *Molecular and Cellular Neuroscience*, 2009.
- [32] Nicolas Cubedo, Emmanuel Cerdan, Dora Sapede, and Mireille Rossel. CXCR4 and CXCR7 cooperate during tangential migration of facial motoneurons. *Molecular and Cellular Neuroscience*, 40(4):474–484, apr 2009.
- [33] Dask Development Team. *Dask: Library for dynamic task scheduling*, 2016.
- [34] Gustavo de Medeiros, Nils Norlin, Stefan Gunther, Marvin Albert, Laura Panavaite, Ulla-Maj Fiuza, Francesca Peri, Takashi Hiiragi, Uros Krzic, and Lars Hufnagel. Confocal multiview light-sheet microscopy. *Nature Communications*, 6(1):8881, dec 2015.
- [35] Fabien M. Décaillot, Manija A. Kazmi, Ying Lin, Sarmistha Ray-Saha, Thomas P. Sakmar, and Pallavi Sachdev. CXCR7/CXCR4 heterodimer constitutively recruits β -arrestin to enhance cell migration. *Journal of Biological Chemistry*, 2011.
- [36] W Denk, J H Strickler, and W W Webb. Two-photon laser scanning fluorescence microscopy. *Science (New York, N.Y.)*, 248(4951):73–6, apr 1990.

- [37] Elizabeth M. Deuchar. Diffusion in embryogenesis. *Nature*, 1970.
- [38] Yifu Ding, Daniel J Vanselow, Maksim A Yakovlev, Spencer R Katz, Alex Y Lin, Darin P Clark, Phillip Vargas, Xuying Xin, Jean E Copper, Victor A Canfield, Khai C Ang, Yuxin Wang, Xianghui Xiao, Francesco De Carlo, Damian B van Rossum, Patrick La Riviere, and Keith C Cheng. Computational 3D histological phenotyping of whole zebrafish by X-ray histotomography. *eLife*, 8, may 2019.
- [39] Erika Donà. *Self-directed collective cell migration: a fluorescent timer approach*. PhD thesis, Universitaet Heidelberg, 2014.
- [40] Erika Donà, Joseph D. Barry, Guillaume Valentin, Charlotte Quirin, Anton Khmelinskii, Andreas Kunze, Sevi Durdu, Lionel R. Newton, Ana Fernandez-Minan, Wolfgang Huber, Michael Knop, and Darren Gilmour. Directional tissue migration through a self-generated chemokine gradient. *Nature*, 503(7475):285, sep 2013.
- [41] Florian O. Fahrbach, Vasily Gurchenkov, Kevin Alessandri, Pierre Nassoy, and Alexander Rohrbach. Self-reconstructing sectioned Bessel beams offer submicron optical sectioning for large fields of view in light-sheet microscopy. *Optics Express*, 21(9):11425, may 2013.
- [42] Henning Falk. *Imaging the onset of the segmentation clock during mouse gastrulation*. PhD thesis, 2018.
- [43] Yu Feng, Christopher C. Broder, Paul E. Kennedy, and Edward A. Berger. HIV-1 entry cofactor: Functional cDNA cloning of a seven-transmembrane, G protein-coupled receptor. *Science*, 1996.
- [44] Paul R. Fisher. Genetics of phototaxis in a model eukaryote, Dictyostelium discoideum, 1997.
- [45] Peter Friedl and Darren Gilmour. Collective cell migration in morphogenesis, regeneration and cancer. *Nature Reviews Molecular Cell Biology*, 10(7):445–

- 457, jul 2009.
- [46] Jochen Fuchs, Susan Böhme, Franz Oswald, Per Niklas Hedde, Maike Krause, Jörg Wiedenmann, and G. Ulrich Nienhaus. A photoactivatable marker protein for pulse-chase imaging with superresolution. *Nature Methods*, 2010.
- [47] Han Gerrits, Dorette S. van Ingen Schenau, Nicole E.C. Bakker, Ad J.M. van Disseldorp, Ankie Strik, Laura S. Hermens, Tim B. Koenen, Magda A.M. Krajnc-Franken, and Jan A. Gossen. Early postnatal lethality and cardiovascular defects in CXCR7-deficient mice. *genesis*, 46(5):235–245, may 2008.
- [48] G. J. Graham, M. Locati, A. Mantovani, A. Rot, and M. Thelen. The biochemistry and biology of the atypical chemokine receptors, 2012.
- [49] Carsten Grashoff, Brenton D. Hoffman, Michael D. Brenner, Ruobo Zhou, Maddy Parsons, Michael T. Yang, Mark A. McLean, Stephen G. Sligar, Christopher S. Chen, Taekjip Ha, and Martin A. Schwartz. Measuring mechanical tension across vinculin reveals regulation of focal adhesion dynamics. *Nature*, 2010.
- [50] G. Grynkiewicz, M. Poenie, and R. Y. Tsien. A new generation of Ca²⁺ indicators with greatly improved fluorescence properties, 1985.
- [51] Tripti Gupta, Gregory D. Marquart, Eric J. Horstick, Kathryn M. Tabor, Sinisa Pajevic, and Harold A. Burgess. Morphometric analysis and neuroanatomical mapping of the zebrafish brain. *Methods*, 150:49–62, nov 2018.
- [52] Petra Haas and Darren Gilmour. Chemokine Signaling Mediates Self-Organizing Tissue Migration in the Zebrafish Lateral Line. *Developmental Cell*, 2006.
- [53] Petra Haas and Darren Gilmour. Chemokine Signaling Mediates Self-Organizing Tissue Migration in the Zebrafish Lateral Line. *Developmental Cell*, 2006.

- [54] Bodduluri Haribabu, Ricardo M. Richardson, Ian Fisher, Silvano Sozzani, Stephen C. Peiper, Richard Horuk, Hydar Ali, and Ralph Snyderman. Regulation of human chemokine receptors CXCR4: Role of phosphorylation in desensitization and internalization. *Journal of Biological Chemistry*, 1997.
- [55] Michael R M Harrison, Jeroen Bussmann, Ying Huang, Long Zhao, Arthela Osorio, C Geoffrey Burns, Caroline E Burns, Henry M Sucov, Arndt F Siekmann, and Ching-Ling Lien. Chemokine-guided angiogenesis directs coronary vasculature formation in zebrafish. *Developmental cell*, 33(4):442–54, may 2015.
- [56] Larry V. Hedges and Ingram. Olkin. *Statistical methods for meta-analysis*. Academic Press, 1985.
- [57] David Hörl, Fabio Rojas Rusak, Friedrich Preusser, Paul Tillberg, Nadine Randel, Raghav K. Chhetri, Albert Cardona, Philipp J. Keller, Hartmann Harz, Heinrich Leonhardt, Mathias Treier, and Stephan Preibisch. BigStitcher: reconstructing high-resolution image datasets of cleared and expanded samples. *Nature Methods*, 16(9):870–874, sep 2019.
- [58] Jan Huisken. Slicing embryos gently with laser light sheets. *BioEssays*, 34(5):406–411, may 2012.
- [59] Jan Huisken and Didier Y R Stainier. Selective plane illumination microscopy techniques in developmental biology. *Development (Cambridge, England)*, 136(12):1963–75, jun 2009.
- [60] Jan Huisken, Jim Swoger, Filippo Del Bene, Joachim Wittbrodt, and Ernst H K Stelzer. Optical sectioning deep inside live embryos by selective plane illumination microscopy. *Science (New York, N.Y.)*, 305(5686):1007–9, aug 2004.
- [61] James B. Pawley, editor. *Handbook of Biological Confocal Microscopy - Google Books*. Third edition.

- [62] Tian Jin. Gradient sensing during chemotaxis, 2013.
- [63] Heath E. Johnson and Jared E. Toettcher. Signaling Dynamics Control Cell Fate in the Early *Drosophila* Embryo. *Developmental Cell*, 2019.
- [64] Eric Jones, Travis Oliphant, Pearu Peterson, and Others. {SciPy}: Open source scientific tools for {Python}.
- [65] Philipp J Keller, Annette D Schmidt, Anthony Santella, Khaled Khairy, Zhirong Bao, Joachim Wittbrodt, and Ernst H K Stelzer. Fast, high-contrast imaging of animal development with scanned light sheet-based structured-illumination microscopy. *Nature Methods*, 7(8):637–642, aug 2010.
- [66] Philipp J Keller and Ernst HK Stelzer. Quantitative in vivo imaging of entire embryos with Digital Scanned Laser Light Sheet Fluorescence Microscopy. *Current Opinion in Neurobiology*, 18(6):624–632, dec 2008.
- [67] E. Kelly, C. P. Bailey, and G. Henderson. Agonist-selective mechanisms of GPCR desensitization. In *British Journal of Pharmacology*, 2008.
- [68] Ross N. W. Kettleborough, Elisabeth M. Busch-Nentwich, Steven A. Harvey, Christopher M. Dooley, Ewart de Bruijn, Freek van Eeden, Ian Sealy, Richard J. White, Colin Herd, Isaac J. Nijman, Fruzsina Fényes, Selina Mehroke, Catherine Scahill, Richard Gibbons, Neha Wali, Samantha Caruthers, Amanda Hall, Jennifer Yen, Edwin Cuppen, and Derek L. Stemple. A systematic genome-wide analysis of zebrafish protein-coding gene function. *Nature*, 496(7446):494–497, apr 2013.
- [69] Anton Khmelinskii, Philipp J Keller, Anna Bartosik, Matthias Meurer, Joseph D Barry, Balca R Mardin, Andreas Kaufmann, Susanne Trautmann, Malte Wachsmuth, Gislene Pereira, Wolfgang Huber, Elmar Schiebel, and Michael Knop. Tandem fluorescent protein timers for in vivo analysis of protein dynamics. *Nature Biotechnology*, 30(7):708–714, jun 2012.

- [70] Boris N. Kholodenko, John F. Hancock, and Walter Kolch. Signalling ballet in space and time. *Nature Reviews Molecular Cell Biology*, 11(6):414–426, jun 2010.
- [71] Anna Kicheva, Periklis Pantazis, Tobias Bollenbach, Yannis Kalaidzidis, Thomas Bittig, Frank Jülicher, and Marcos González-Gaitán. Kinetics of morphogen gradient formation. *Science*, 2007.
- [72] Hyung Do Kim and Shelly R. Peyton. Bio-inspired materials for parsing matrix physicochemical control of cell migration: A Review, 2012.
- [73] Jihoon Kim, Sangkyu Lee, Kanghoon Jung, Won Chan Oh, Nury Kim, Seungkyu Son, Young Ju Jo, Hyung Bae Kwon, and Won Do Heo. Intensiometric biosensors visualize the activity of multiple small GTPases in vivo. *Nature Communications*, 2019.
- [74] Jihoon Kim, Sangkyu Lee, Kanghoon Jung, Won Chan Oh, Nury Kim, Seungkyu Son, YoungJu Jo, Hyung-Bae Kwon, and Won Do Heo. Intensiometric biosensors visualize the activity of multiple small GTPases in vivo. *Nature Communications*, 10(1):211, dec 2019.
- [75] Charles B Kimmel, William W Ballard, Seth R Kimmel, Bonnie Ullmann, and Thomas F Schilling. Stages of Embryonic Development of the Zebrafish. Technical report, 1995.
- [76] Arno Klein, Jesper Andersson, Babak A. Ardekani, John Ashburner, Brian Avants, Ming-Chang Chiang, Gary E. Christensen, D. Louis Collins, James Gee, Pierre Hellier, Joo Hyun Song, Mark Jenkinson, Claude Lepage, Daniel Rueckert, Paul Thompson, Tom Vercauteren, Roger P. Woods, J. John Mann, and Ramin V. Parsey. Evaluation of 14 nonlinear deformation algorithms applied to human brain MRI registration. *NeuroImage*, 46(3):786–802, jul 2009.

- [77] S. Klein, M. Staring, K. Murphy, M.A. Viergever, and J. Pluim. elastix: A Toolbox for Intensity-Based Medical Image Registration. *IEEE Transactions on Medical Imaging*, 29(1):196–205, jan 2010.
- [78] Michael Knop and Bruce A. Edgar. Tracking protein turnover and degradation by microscopy: photo-switchable versus time-encoded fluorescent proteins. *Open Biology*, 4(4):140002, apr 2014.
- [79] Brian K. Kobilka. G protein coupled receptor structure and activation, 2007.
- [80] U Krzic. Multiple-view microscopy with light-sheet based fluorescence microscope. (July):155, 2009.
- [81] Uros Krzic. *Multiple-view microscopy with light-sheet based fluorescence microscope*. PhD thesis, 2009.
- [82] Uros Krzic, Stefan Gunther, Timothy E Saunders, Sebastian J Streichan, and Lars Hufnagel. Multiview light-sheet microscope for rapid in toto imaging. *Nature Methods*, 9(7):730–733, jul 2012.
- [83] Ashok Kumar, Kimberly N. Kremer, Daniel Dominguez, Madhavi Tadi, and Karen E. Hedin. $G\alpha 13$ and Rho Mediate Endosomal Trafficking of CXCR4 into Rab11 + Vesicles upon Stromal Cell-Derived Factor-1 Stimulation . *The Journal of Immunology*, 2011.
- [84] Michael Kunst, Eva Laurell, Nouwar Mokayes, Anna Kramer, Fumi Kubo, António M. Fernandes, Dominique Förster, Marco Dal Maschio, and Herwig Baier. A Cellular-Resolution Atlas of the Larval Zebrafish Brain. *Neuron*, 103(1):21–38.e5, jul 2019.
- [85] Joseph R. Lakowicz. *Principles of fluorescence spectroscopy*. 2006.
- [86] D A Lauffenburger and A F Horwitz. Cell migration: a physically integrated molecular process. *Cell*, 84(3):359–69, feb 1996.
- [87] Virginie Lecaudey and Darren Gilmour. Organizing moving groups during morphogenesis. *Current Opinion in Cell Biology*, 18(1):102–107, feb 2006.

- [88] Virginie Lecaudey and Darren Gilmour. Organizing moving groups during morphogenesis. *Current Opinion in Cell Biology*, 18(1):102–107, feb 2006.
- [89] Angélique Levoye, Karl Balabanian, Françoise Baleux, Françoise Bachelerie, and Bernard Lagane. CXCR7 heterodimerizes with CXCR4 and regulates CXCL12-mediated G protein signaling. *Blood*, 2009.
- [90] Stephen W. Lewellis and Holger Knaut. Attractive guidance: How the chemokine SDF1/CXCL12 guides different cells to different locations, 2012.
- [91] Stephen W. Lewellis, Danielle Nagelberg, Abhi Subedi, Alison Staton, Michelle LeBlanc, Antonio Giraldez, and Holger Knaut. Precise SDF1-mediated cell guidance is achieved through ligand clearance and microRNA-mediated decay. *Journal of Cell Biology*, 2013.
- [92] Francis Lin and Eugene C. Butcher. Modeling the Role of Homologous Receptor Desensitization in Cell Gradient Sensing. *Journal of immunology (Baltimore, Md. : 1950)*, 181(12):8335, 2008.
- [93] Bradley C. Lowekamp, David T. Chen, Luis Ibáñez, and Daniel Blezek. The Design of SimpleITK. *Frontiers in Neuroinformatics*, 7:45, 2013.
- [94] Jianguo Lu, Eric Peatman, Haibao Tang, Joshua Lewis, and Zhanjiang Liu. Profiling of gene duplication patterns of sequenced teleost genomes: evidence for rapid lineage-specific genome expansion mediated by recent tandem duplications. *BMC genomics*, 13:246, jun 2012.
- [95] Louis M Luttrell and Robert J Lefkowitz. The role of beta-arrestins in the termination and transduction of G-protein-coupled receptor signals. *Journal of cell science*, 115(Pt 3):455–65, feb 2002.
- [96] Matthias Machacek, Louis Hodgson, Christopher Welch, Hunter Elliott, Olivier Pertz, Perihan Nalbant, Amy Abell, Gary L. Johnson, Klaus M. Hahn, and Gaudenz Danuser. Coordination of Rho GTPase activities during cell protrusion. *Nature*, 461(7260):99–103, sep 2009.

- [97] Paul S Maddox, Ben Moree, Julie C Canman, and E D Salmon. Spinning disk confocal microscope system for rapid high-resolution, multimode, fluorescence speckle microscopy and green fluorescent protein imaging in living cells. *Methods in enzymology*, 360:597–617, 2003.
- [98] J.-F Mangin, J Lebenberg, S Lefranc, N Labra, Guillaume Auzias, M Labit, M Guevara, H Mohlberg, P Roca, and P Guevara. Spatial normalization of brain images and beyond. *Medical Image Analysis*, 33:127–133, 2016.
- [99] Adriano Marchese and Jeffrey L. Benovic. Agonist-promoted Ubiquitination of the G Protein-coupled Receptor CXCR4 Mediates Lysosomal Sorting. *Journal of Biological Chemistry*, 2001.
- [100] Gregory D. Marquart, Kathryn M. Tabor, Mary Brown, Jennifer L. Strykowski, Gaurav K. Varshney, Matthew C. LaFave, Thomas Mueller, Shawn M. Burgess, Shin-ichi Higashijima, and Harold A. Burgess. A 3D Searchable Database of Transgenic Zebrafish Gal4 and Cre Lines for Functional Neuroanatomy Studies. *Frontiers in Neural Circuits*, 9:78, nov 2015.
- [101] Gregory D. Marquart, Kathryn M. Tabor, Eric J. Horstick, Mary Brown, and Harold A. Burgess. High precision registration between zebrafish brain atlases using symmetric diffeomorphic normalization. *bioRxiv*, page 081000, oct 2016.
- [102] Kasper Marstal, Floris Berendsen, Marius Staring, and Stefan Klein. SimpleElastix: A User-Friendly, Multi-lingual Library for Medical Image Registration. In *2016 IEEE Conference on Computer Vision and Pattern Recognition Workshops (CVPRW)*, pages 574–582. IEEE, jun 2016.
- [103] Kasper Marstal, Floris Berendsen, Marius Staring, and Stefan Klein. SimpleElastix: A User-Friendly, Multi-lingual Library for Medical Image Registration. In *2016 IEEE Conference on Computer Vision and Pattern Recognition Workshops (CVPRW)*, pages 574–582. IEEE, jun 2016.
- [104] Roberto Mayor and Sandrine Etienne-Manneville. The front and rear of collective cell migration, 2016.

- [105] Roberto Mayor and Eric Theveneau. The neural crest. *Development (Cambridge)*, 2012.
- [106] Fani Memi, Philipp Abe, Anna Cariboni, Fabienne MacKay, John G. Parnavelas, and Ralf Stumm. CXC chemokine receptor 7 (CXCR7) affects the migration of GnRH neurons by regulating CXCL12 availability. *Journal of Neuroscience*, 2013.
- [107] Takeshi Miyatsuka, Zhongmei Li, and Michael S. German. Chronology of islet differentiation revealed by temporal cell labeling. *Diabetes*, 2009.
- [108] D. J. Montell. Morphogenetic Cell Movements: Diversity from Modular Mechanical Properties. *Science*, 322(5907):1502–1505, dec 2008.
- [109] Anja Müller, Bernhard Homey, Hortensia Soto, Nianfeng Ge, Daniel Catron, Matthew E. Buchanan, Terri McClanahan, Erin Murphy, Wei Yuan, Stephan N. Wagner, Jose Luis Barrera, Alejandro Mohar, Emma Verástegui, and Albert Zlotnik. Involvement of chemokine receptors in breast cancer metastasis. *Nature*, 2001.
- [110] Maria E. Mycielska and Mustafa B.A. Djamgoz. Cellular mechanisms of direct-current electric field effects: Galvanotaxis and metastatic disease, 2004.
- [111] Sreelaja Nair and Thomas F. Schilling. Chemokine signaling controls endodermal migration during zebrafish gastrulation. *Science (New York, N.Y.)*, 322(5898):89, 2008.
- [112] J. Nakai, M. Ohkura, and K. Imoto. A high signal-to-noise ca^{2+} probe composed of a single green fluorescent protein. *Nature Biotechnology*, 2001.
- [113] Robert H. Newman, Matthew D. Fosbrink, and Jin Zhang. Genetically encodable fluorescent biosensors for tracking signaling dynamics in living cells, 2011.
- [114] Charles Nicholson and Eva Syková. Extracellular space structure revealed by diffusion analysis. *Trends in Neurosciences*, 1998.

- [115] Francisco P.M. Oliveira and João Manuel R.S. Tavares. Medical image registration: a review. *Computer Methods in Biomechanics and Biomedical Engineering*, 17(2):73–93, jan 2014.
- [116] J. J. Oppenheim, C. O C Zachariae, N. Mukaida, and K. Matsushima. Properties of the novel proinflammatory supergene "intercrine" cytokine family, 1991.
- [117] Hanchuan Peng, Phuong Chung, Fuhui Long, Lei Qu, Arnim Jenett, Andrew M Seeds, Eugene W Myers, and Julie H Simpson. BrainAligner: 3D registration atlases of Drosophila brains. *Nature Methods*, 8(6):493–498, jun 2011.
- [118] Ryan J Petrie, Andrew D Doyle, and Kenneth M Yamada. Random versus directionally persistent cell migration. *Nature reviews. Molecular cell biology*, 10(8):538–49, aug 2009.
- [119] Caren E. Petrie Aronin, Yun M. Zhao, Justine S. Yoon, Nicole Y. Morgan, Thorsten Prüstel, Ronald N. Germain, and Martin Meier-Schellersheim. Migrating Myeloid Cells Sense Temporal Dynamics of Chemoattractant Concentrations. *Immunity*, 47(5):862–874.e3, nov 2017.
- [120] Robert Pick, Doris Brechtefeld, and Barbara Walzog. Intraluminal crawling versus interstitial neutrophil migration during inflammation. *Molecular Immunology*, 55(1):70–75, aug 2013.
- [121] Stephan Preibisch, Fernando Amat, Evangelia Stamatakis, Mihail Sarov, Robert H Singer, Eugene Myers, and Pavel Tomancak. Efficient Bayesian-based multiview deconvolution. *Nature Methods*, 11(6):645–648, jun 2014.
- [122] Stephan Preibisch, Torsten Rohlfing, Michael P. Hasak, and Pavel Tomancak. Mosaicing of single plane illumination microscopy images using groupwise registration and fast content-based image fusion. volume 6914, page 69140E. International Society for Optics and Photonics, mar 2008.

- [123] Stephan Preibisch, Stephan Saalfeld, Johannes Schindelin, and Pavel Tomancak. Software for bead-based registration of selective plane illumination microscopy data. *Nature Methods*, 7(6):418–419, jun 2010.
- [124] Sudarshan Rajagopal, Jihee Kim, Seungkirl Ahn, Stewart Craig, Christopher M. Lam, Norma P. Gerard, Craig Gerard, and Robert J. Lefkowitz. β -Arrestin- But not G protein-mediated signaling by the "decoy" receptor CXCR7. *Proceedings of the National Academy of Sciences of the United States of America*, 2010.
- [125] Owen Randlett, Caroline L Wee, Eva A Naumann, Onyeka Nnaemeka, David Schoppik, James E Fitzgerald, Ruben Portugues, Alix M B Lacoste, Clemens Riegler, Florian Engert, and Alexander F Schier. Whole-brain activity mapping onto a zebrafish brain atlas. *Nature Methods*, 12(11):1039–1046, nov 2015.
- [126] Owen Randlett, Caroline L Wee, Eva A Naumann, Onyeka Nnaemeka, David Schoppik, James E Fitzgerald, Ruben Portugues, Alix M B Lacoste, Clemens Riegler, Florian Engert, and Alexander F Schier. Whole-brain activity mapping onto a zebrafish brain atlas. *Nature Methods*, 12(11):1039–1046, nov 2015.
- [127] Owen Randlett, Caroline L. Wee, Eva A. Naumann, Onyeka Nnaemeka, David Schoppik, James E. Fitzgerald, Ruben Portugues, Alix M.B. Lacoste, Clemens Riegler, Florian Engert, and Alexander F. Schier. Whole-brain activity mapping onto a zebrafish brain atlas. *Nature Methods*, 2015.
- [128] Erez Raz. Primordial germ-cell development: The zebrafish perspective, 2003.
- [129] Anne J Ridley, Martin A Schwartz, Keith Burridge, Richard A Firtel, Mark H Ginsberg, Gary Borisy, J Thomas Parsons, and Alan Rick Horwitz. Cell migration: integrating signals from front to back. *Science (New York, N.Y.)*, 302(5651):1704–9, dec 2003.

- [130] Matthew Rocklin. Dask: Parallel Computation with Blocked algorithms and Task Scheduling. In Kathryn Huff and James Bergstra, editors, *Proceedings of the 14th Python in Science Conference*, pages 130–136, 2015.
- [131] Olaf Ronneberger, Kun Liu, Meta Rath, Dominik Rueß, Thomas Mueller, Henrik Skibbe, Benjamin Drayer, Thorsten Schmidt, Alida Filippi, Roland Nitschke, Thomas Brox, Hans Burkhardt, and Wolfgang Driever. ViBE-Z: a framework for 3D virtual colocalization analysis in zebrafish larval brains. *Nature Methods*, 9(7):735–742, jul 2012.
- [132] Pernille Rorth. Whence Directionality: Guidance Mechanisms in Solitary and Collective Cell Migration, 2011.
- [133] Pernille Rorth. Fellow travellers: emergent properties of collective cell migration. *EMBO reports*, 13(11):984–991, oct 2012.
- [134] Myriam Roussigné, Isaac H Bianco, Stephen W Wilson, and Patrick Blader. Nodal signalling imposes left-right asymmetry upon neurogenesis in the habenular nuclei. *Development (Cambridge, England)*, 136(9):1549–57, may 2009.
- [135] Loïc A Royer, William C Lemon, Raghav K Chhetri, Yinan Wan, Michael Coleman, Eugene W Myers, and Philipp J Keller. Adaptive light-sheet microscopy for long-term, high-resolution imaging in living organisms. *Nature Biotechnology*, 34(12):1267–1278, dec 2016.
- [136] Vedangi Sample, Sohumi Mehta, and Jin Zhang. Genetically encoded molecular probes to visualize and perturb signaling dynamics in living biological systems, 2014.
- [137] Vedangi Sample, Sohumi Mehta, and Jin Zhang. Genetically encoded molecular probes to visualize and perturb signaling dynamics in living biological systems. *Journal of cell science*, 127(Pt 6):1151–60, mar 2014.
- [138] Juan Antonio Sánchez-Alcañiz, Sammy Haegel, Wiebke Mueller, Ramón Pla, Fabienne Mackay, Stefan Schulz, Guillermina López-Bendito, Ralf Stumm,

- and Oscar Marín. Cxcr7 Controls Neuronal Migration by Regulating Chemokine Responsiveness. *Neuron*, 2011.
- [139] Daria M. Shcherbakova, Natasha Cox Cammer, Tsipora M. Huisman, Vladislav V. Verkhusha, and Louis Hodgson. Direct multiplex imaging and optogenetics of Rho GTPases enabled by near-infrared FRET. *Nature Chemical Biology*, 14(6):591–600, jun 2018.
- [140] F. Sierro, C. Biben, L. Martinez-Munoz, M. Mellado, R. M. Ransohoff, M. Li, B. Woehl, H. Leung, J. Groom, M. Batten, R. P. Harvey, C. Martinez-A, C. R. Mackay, and F. Mackay. Disrupted cardiac development but normal hematopoiesis in mice deficient in the second CXCL12/SDF-1 receptor, CXCR7. *Proceedings of the National Academy of Sciences*, 104(37):14759–14764, sep 2007.
- [141] Frederic Sierro, Christine Biben, Laura Martínez-Muñoz, Mario Mellado, Richard M. Ransohoff, Meizhang Li, Blanche Woehl, Helen Leung, Joanna Groom, Marcel Batten, Richard P. Harvey, Carlos Martínez-A, Charles R. Mackay, and Fabienne Mackay. Disrupted cardiac development but normal hematopoiesis in mice deficient in the second CXCL12/SDF-1 receptor, CXCR7. *Proceedings of the National Academy of Sciences of the United States of America*, 2007.
- [142] Sara Sigismund, Elisabetta Argenzio, Daniela Tosoni, Elena Cavallaro, Simona Polo, and Pier Paolo Di Fiore. Clathrin-Mediated Internalization Is Essential for Sustained EGFR Signaling but Dispensable for Degradation. *Developmental Cell*, 2008.
- [143] Natalie Signoret, Joanne Oldridge, Annegret Pelchen-Matthews, Per J. Klasse, Thanh Tran, Lawrence F. Brass, Mette M. Rosenkilde, Thue W. Schwartz, William Holmes, Walt Dallas, Michael A. Luther, Timothy N.C. Wells, James A. Hoxie, and Mark Marsh. Phorbol esters and SDF-1 induce rapid

- endocytosis and down modulation of the chemokine receptor CXCR4. *Journal of Cell Biology*, 1997.
- [144] L. Silvestri, A. Bria, L. Sacconi, G. Iannello, and F. S. Pavone. Confocal light sheet microscopy: micron-scale neuroanatomy of the entire mouse brain. *Optics Express*, 20(18):20582, aug 2012.
- [145] Christoph Sommer, Christoph Straehle, Ullrich Kothe, and Fred A. Hamprecht. Ilastik: Interactive learning and segmentation toolkit. In *2011 IEEE International Symposium on Biomedical Imaging: From Nano to Macro*, pages 230–233. IEEE, mar 2011.
- [146] Fedor V. Subach, Oksana M. Subach, Illia S. Gundorov, Kateryna S. Morozova, Kiryl D. Piatkevich, Ana Maria Cuervo, and Vladislav V. Verkhusha. Monomeric fluorescent timers that change color from blue to red report on cellular trafficking. *Nature Chemical Biology*, 2009.
- [147] Katsiaryna Tarbashevich and Erez Raz. The nuts and bolts of germ-cell migration. *Current Opinion in Cell Biology*, 22(6):715–721, dec 2010.
- [148] Maja Temerinac-Ott, Olaf Ronneberger, Roland Nitschke, Wolfgang Driever, and Hans Burkhardt. Spatially-variant Lucy-Richardson deconvolution for multiview fusion of microscopical 3D images. In *2011 IEEE International Symposium on Biomedical Imaging: From Nano to Macro*, pages 899–904. IEEE, mar 2011.
- [149] A. Terskikh, A. Fradkov, G. Ermakova, A. Zarsky, P. Tan, A. V. Kajava, X. Zhao, S. Lukyanov, M. Matz, S. Kim, I. Weissman, and P. Siebert. 'Fluorescent timer': Protein that changes color with time. *Science*, 2000.
- [150] Eric Theveneau and Roberto Mayor. Cadherins in collective cell migration of mesenchymal cells. *Current Opinion in Cell Biology*, 24(5):677–684, oct 2012.
- [151] Chiara Tobia, Paola Chiodelli, Andrea Barbieri, Simone Buraschi, Elena Ferrari, Stefania Mitola, Giuseppe Borsani, Jessica Guerra, and Marco Presta.

- Atypical Chemokine Receptor 3 Generates Guidance Cues for CXCL12-Mediated Endothelial Cell Migration. *Frontiers in immunology*, 10:1092, 2019.
- [152] Raju Tomer, Alexandru S. Denes, Kristin Tessmar-Raible, and Detlev Arendt. Profiling by Image Registration Reveals Common Origin of Annelid Mushroom Bodies and Vertebrate Pallium. *Cell*, 142(5):800–809, sep 2010.
- [153] Raju Tomer, Khaled Khairy, Fernando Amat, and Philipp J Keller. Quantitative high-speed imaging of entire developing embryos with simultaneous multiview light-sheet microscopy. *Nature Methods*, 9(7):755–763, jul 2012.
- [154] Thai V Truong, Willy Supatto, David S Koos, John M Choi, and Scott E Fraser. Deep and fast live imaging with two-photon scanned light-sheet microscopy. *Nature Methods*, 8(9):757–760, sep 2011.
- [155] Luke Tweedy, Olivia Susanto, and Robert H Insall. Self-generated chemotactic gradients - cells steering themselves. *Current Opinion in Cell Biology*, 42:46–51, oct 2016.
- [156] Guillaume Valentin, Petra Haas, and Darren Gilmour. The Chemokine SDF1a Coordinates Tissue Migration through the Spatially Restricted Activation of Cxcr7 and Cxcr4b. *Current Biology*, 2007.
- [157] Stéfan van der Walt, S Chris Colbert, and Gaël Varoquaux. The NumPy Array: A Structure for Efficient Numerical Computation. *Computing in Science & Engineering*, 13(2):22–30, mar 2011.
- [158] Stéfan van der Walt, Johannes L. Schönberger, Juan Nunez-Iglesias, François Boulogne, Joshua D. Warner, Neil Yager, Emmanuelle Gouillart, and Tony Yu. scikit-image: image processing in Python. *PeerJ*, 2:e453, jun 2014.
- [159] Gayatri Venkiteswaran, Stephen W Lewellis, John Wang, Eric Reynolds, Charles Nicholson, and Holger Knaut. Generation and dynamics of an endogenous, self-generated signaling gradient across a migrating tissue. *Cell*, 155(3):674–87, oct 2013.

- [160] Gayatri Venkiteswaran, Stephen W. Lewellis, John Wang, Eric Reynolds, Charles Nicholson, and Holger Knaut. Generation and Dynamics of an Endogenous, Self-Generated Signaling Gradient across a Migrating Tissue. *Cell*, 155(3):674–687, oct 2013.
- [161] Michael Weber and Jan Huisken. Light sheet microscopy for real-time developmental biology. *Current Opinion in Genetics & Development*, 21(5):566–572, oct 2011.
- [162] Martin Weigert, Uwe Schmidt, Tobias Boothe, Andreas Müller, Alexandr Dibrov, Akanksha Jain, Benjamin Wilhelm, Deborah Schmidt, Coleman Broadus, Siân Culley, Mauricio Rocha-Martins, Fabián Segovia-Miranda, Caren Norden, Ricardo Henriques, Marino Zerial, Michele Solimena, Jochen Rink, Pavel Tomancak, Loic Royer, Florian Jug, and Eugene W. Myers. Content-aware image restoration: pushing the limits of fluorescence microscopy. *Nature Methods*, 15(12):1090–1097, dec 2018.
- [163] Martin Weigert, Kaushikaram Subramanian, Sebastian T. Bundschuh, Eugene W. Myers, and Moritz Kreysing. Biobeam - Multiplexed wave-optical simulations of light-sheet microscopy. *PLOS Computational Biology*, 14(4):e1006079, apr 2018.
- [164] Venera Weinhardt, Roman Shkarin, Tobias Wernet, Joachim Wittbrodt, Tilo Baumbach, and Felix Loosli. Quantitative morphometric analysis of adult teleost fish by X-ray computed tomography. *Scientific Reports*, 8(1):16531, dec 2018.
- [165] Christopher M. Welch, Hunter Elliott, Gaudenz Danuser, and Klaus M. Hahn. Imaging the coordination of multiple signalling activities in living cells, 2011.
- [166] Zhengui Xia, Henryk Dudek, Cindy K. Miranti, and Michael E. Greenberg. Calcium influx via the NMDA receptor induces immediate early gene transcription by a MAP kinase/ERK-dependent mechanism. *Journal of Neuroscience*, 1996.

- [167] Jingsong Xu, Fei Wang, Alexandra Van Keymeulen, Paul Herzmark, Aaron Straight, Kathleen Kelly, Yoh Takuwa, Naotoshi Sugimoto, Timothy Mitchison, and Henry R. Bourne. Divergent signals and cytoskeletal assemblies regulate self-organizing polarity in neutrophils. *Cell*, 2003.
- [168] Terry S Yoo, Michael J Ackerman, William E Lorensen, Will Schroeder, Vikram Chalana, Stephen Aylward, Dimitris Metaxas, and Ross Whitaker. Engineering and algorithm design for an image processing Api: a technical report on ITK—the Insight Toolkit. *Studies in health technology and informatics*, 85:586–92, 2002.
- [169] Sangho Yu, Dianna Crawford, Takatoshi Tsuchihashi, Timothy W Behrens, and Deepak Srivastava. The chemokine receptor CXCR7 functions to regulate cardiac valve remodeling. *Developmental dynamics : an official publication of the American Association of Anatomists*, 240(2):384–93, feb 2011.
- [170] Sangho Yu, Dianna Crawford, Takatoshi Tsuchihashi, Timothy W. Behrens, and Deepak Srivastava. The chemokine receptor CXCR7 functions to regulate cardiac valve remodeling. *Developmental Dynamics*, 240(2):384–393, feb 2011.
- [171] Qiang Zhang, Hai Huang, Luqing Zhang, Roland Wu, Chan-I Chung, Shao-Qing Zhang, Joaquim Torra, Antonino Schepis, Shaun R. Coughlin, Thomas B. Kornberg, and Xiaokun Shu. Visualizing Dynamics of Cell Signaling In Vivo with a Phase Separation-Based Kinase Reporter. *Molecular Cell*, 69(2):334–346.e4, jan 2018.
- [172] Sally H. Zigmond. Ability of polymorphonuclear leukocytes to orient in gradients of chemotactic factors. *Journal of Cell Biology*, 1977.